Rotation and Polarization in Heavy Ion Collisions

Yilong Xie

Thesis for the degree of philosophiae doctor (PhD)
at the University of Bergen

2017

Date of defence: Dec. 19, 2017

Contact: Yilong Xie

Departments of Physics and Technology

University of Bergen

Allégaten 55

5007 Bergen

Norway

Email: yi.long.xie.china@gmail.com

Acknowledgements

Time flies like a flash. Suddenly I come to the gate of graduation, caught by surprise.

At the first and most, thanks must be dedicated to Prof. László Pál Csernai. During the three and half years, I learned not only the profound knowledge from him, but also the scientific attitude to the natural and life itself. Besides, as a foreign student in Norway, I frequently encountered many challenges from physical and spiritual aspects, and he was always there to help me out. Finally, he is a fast man, he does everything in an effective and fast way that I never imagined before my doctoral career, while I am a very slow person, even sort of wishy-washy. This is one of the most important things that I need to learn and master during the rest of my life —

Fast, like a flash, like the time.

Only in this way, you can catch up with the steps of life.

I would like to thank Prof. Jan S. Vaagen, Prof. Larissa Bravina, as well as Prof. Gang Chen, my master supervisor, thank you all for those helpful suggestions and advices. I would like to thank Prof. Marcus Bleicher and Prof. Horst Stöcker for his kind hospitality during my stay in Frankfurt Institute for Advanced Studies(FIAS).

I would like to give my deepest respect to Prof. Benhao Sa and his wife. He is a typical Chinese scientist of old times, shining the virtues of wisdom, kindness, perseverance, diligence, tolerance, etc. His wife talked to me and kindly gave me advices when I started my doctoral career in 2014. They are one of the archetypes, which I hope I could be when I am getting old.

Also I want to mention my nice colleagues in Bergen, Dujuan Wang, Sindre Velle,

Susanne Flø Spinnangr, Istvan Papp, Sharareh Mehrabi Pari, Eirik Hatlen, Robert C. Glastad. They come from different countries and cultures, with a different way to treat the world. It is quite interesting and inspiring to discuss with them. They enriched my life in Bergen.

Finally, I would like to express the deepest thanks to my family, my parent and sisters. Love can not be taken for granted. They are the source of power to drive me to move forward.

Abstract

Relativistic thermodynamics with spin invented the polarization 4-vector to characterize the spin alignment effect in a rotating system. Then based on an Exact hydrodynamic model, we found an analytic solution of spatial part of Λ polarization 4-vector in non-relativistic limits. The results indicate the considerable contribution from the second term arising from the system expansion, which was neglected in previous studies. Then based on the Particle-in-Cell Relativistic (PICR) hydrodynamic simulation, we numerically solve the polarization vector for Λ hyperons at NICA and FAIR energies, and find that the y component of the polarization vector is dominant while x and z components are anti-symmetric at transverse momentum space, implying a vanishing contribution to the global polarization (at collider frame). Finally , we analyze the dependence of Λ polarization effect on centrality, energy and time, in our model. The linear dependence of Λ polarization on impact parameter reveal that the polarization stems from the initial orbital angular momentum; the polarization effects is found to decreases with the increasing energies, which is in line with the recent results from RHIC BES program, and is attributed to the intensive thermal motion of particles in higher energy; the time evolution of the Λ polarization in our calculation agrees with the time evolution of vorticity predicted previously, and indicates the invalidity of hydrodynamic model at later stage of system expansion. Besides, we develop a new Initial State model to adapt to the progress of recent experiments and theoretical studies, keeping the basic features of our early initial model, such as shear, angular momentum conservation and vorticity. This new IS model will help us to simulate a more realistic high-energy collisions.

Contents

Acknowledgements **i**

Abstract **iii**

Contents **iii**

Acronyms **vi**

1 Introduction **1**

2 Theoretical fundamentals **4**

2.1 Definitions and Notations 4

2.1.1 Microscopic variables 4

2.1.2 Macroscopic variables 7

2.2 Hydrodynamic model 9

2.2.1 Relativistic Boltzmann transport equation (BTE) and Jüttner distribution 11

2.2.2 The Particle in Cell (PIC) method 13

2.3 Initial state and freeze out 14

3 Polarization in non-relativistic limit **18**

3.1 The Exact rotating fluid dynamical model 19

3.2 Relativistic thermodynamics with spin 21

3.3 Solution for the Λ polarization vector 25

3.4 Results and Analysis 26

4 Global Λ polarization for intermediate energy 32

4.1 Polarization effect: from experiments to theory 32

4.2 Initial state and hydrodynamic model 35

4.3 Freeze out Stage 37

4.4 Λ Polarization for NICA and FAIR 38

4.5 Centrality and energy dependence, time evolution 43

4.5.1 Angular momentum, Impact Parameter and Centrality 44

4.5.2 Energy Dependence and Time evolution 46

4.6 Summary and Conclusion 48

5 Inital state with shear 51

5.1 Configuration and Milne Coordinate 52

5.2 Conservation law 55

5.3 The implementation of the model 58

5.4 Shear and Vorticity 59

5.5 Discussion 62

6 Summary and outlook 64

Bibliography 72

A The CFD cell structure 72

B Analytic solution for Λ polarization in non-relativistic limit 74

B.1 The denominator 75

B.2 The numerator 79

B.3 The second term 80

C Publications 85

Acronyms

QGP	Quark Gluon Plasma.
LHC	Large Hadron Collider.
RHIC	Relativistic Heavy Ion Collider.
BNL	Brookhaven National Laboratory.
NICA	Nuclotron-based Ion Collider fAcility.
FAIR	Facility for Antiproton and Ion Research.
FO	Freeze Out.
BTE	Boltzmann Transport Equation.
HBT	Hanbury Brown and Twiss.
DHBT	Differential Hanbury Brown and Twiss.
KHI	Kelvin Helmholtz Instability.
FD	Fluid dynamics.
CFD	Computational Fluid Dynamics.
EoS	Equation of State.
PIC	Particle in Cell.
CVE	Chiral Vortical Effect.
CME	Chiral Magnetic Effect.
c.m.	Center of Mass.
LR	Local Rest.
ATLAS	A Toroidal LHC ApparatuS.
CMS	Compact Muon Solenoid.
ALICE	A Large Ion Collider Experiment.
TPC	Time Projection Chamber.
ZDC	Zero Degree Calorimeters.

Chapter 1

Introduction

In 1915, S. J. Barnett found that an uncharged body will get spontaneous magnetization if it is rotating. The angular velocity of this rotating body decreases while a small magnetic field emerges, which reveals the conversion of orbital angular momentum into the spins of the constituents. At the same year, A. Einstein and W.J.de Haas also found that a ferromagnet at rest will start to rotate when put into an external H field. This two experiments confirm the coupling of microscopic spin angular momentum and the macroscopic orbital angular momentum, which may be called 'spin-orbit coupling' or 'equipartition principle' of angular momentum.

In non-central high-energy collisions, there exist also substantial initial orbital angular momentum, leading to a rotating participant system, and thus due to the spin-orbit interaction some exciting phenomena occur in high-energy experiments. Due to the spin-orbit interaction or equipartition principle, the spins of particles will be aligned with the initial angular momentum, which is called polarization. This polarization effect is blind to charge and chirality, i.e. the spins of particles and antiparticles are aligned to identical direction not the opposite directions, different from the polarization that occurs due to electromagnetic field.

By studying the relativistic fluid with spin at local equilibrium, theorists have invented the **polarization 4-vector** to characterize this spin alignment effect.

In this work, we study the Λ polarization mainly based on a string-rope Initial State (IS) model and a Particle-in-Cell Relativistic (PICR) hydrodynamic model. This IS model could naturally generate a longitudinal velocity shear, and with a small viscosity in subsequent hydrodynamic evolution the system will be rotating, which make it possible to calculate the polarization effect.

Finally, people are more and more realizing the importance of the initial state configuration, because the final state of the collision system is very sensitive to the initial state. Thus, considering the recent progress of the experiments and theory, we propose a new IS model to adapt to the new development, while retaining the basic features of our early IS model, e.g. shear, vorticity, angular momentum conservation.

Structure of the thesis

This thesis is mainly based on 4 published papers and 1 conference proceedings. These papers are all listed and shown in Appendix C. The other Appendices are important part of this thesis, providing some necessary details for better understanding.

There are six chapters. Chapter 2 introduces some basic theoretical knowledge, which is the foundation of the subsequent chapters.

Chapter 3, 4, and 5 introduce and summarize the publications:

Chapter 3: Based on an Exact hydrodynamic model, an analytic solution of spatial part of Λ polarization 4-vector is found in non-relativistic limits. The results indicate the considerable contribution form the second term arising from the system expansion, which was neglected in previous studies.

Chapter 4: Based on the Particle-in-Cell Relativistic (PICR) hydrodynamic simulation, we numerically solve the polarization vector for Λ hyperons at NICA and FAIR energies, and find that the y component of the polarization vector is dominant while x and z components are anti-symmetric in the transverse momentum space, thus their sum vanishes. Further more, we analyze the dependence of Λ polarization effect in our model on centrality, energy and time, which agrees well with the recent experiment results and other theoretical simulation.

Chapter 5: A new Initial State model is developed to adapt to the progress from recent experiments and theoretical studies, keeping the basic features of early initial state model (15 years ago), such as shear, angular momentum conservation and vorticity.

Chapter 6 summarizes our study and gives an outlook to this field.

Chapter 2

Theoretical fundamentals

This chapter is based on the textbook "Introduction to Relativistic Heavy Ion Collisions" [1].

2.1 Definitions and Notations

In this work, natural units are adopted, i.e. $c = \hbar = 1$ where c is the light speed and $\hbar$ is the reduced Planck constant. The high-energy systems usually evolve in a speed scale of light, thus the variables and approaches in special relativity are applied to describe the system's evolution.

2.1.1 Microscopic variables

In special relativity, we construct the four dimensional space-time coordinates as $x^\mu = (t, x, y, z)$, composed of the time coordinate t and classical spatial 3-vector $\boldsymbol{r} = (x, y, z)$. The space-time x^μ with superscript is a contravariant vector, could be transformed into a covariant vector with subscript, x_μ, via the metric tensor. In special relativity, the space-time is flat, and the metric tensor is taken to be Minkowski form, i.e. $g^{\mu\nu} = g_{\mu\nu} = diag(1, -1, -1, -1)$. Thus, the covariant space-time vector $x_\mu = g_{\mu\nu} x^\mu = (t, -x, -y, -z)$. Besides, we define the covariant space-time derivative as: $\partial_\mu \equiv \partial / \partial x^\mu =$

$(\partial/\partial t, \nabla)$.

The four momentum of a particle in the space-time is $p^\mu = (p^0, \boldsymbol{p})$, where $p^0 = E = \sqrt{\boldsymbol{p}^2 + m^2}$ is the particle's relativistic energy, $\boldsymbol{p}$ is the classical 3-momentum, and m is the particle's mass in its own frame. Thus, the four momentum is normalized to the particle's rest mass:

$$p^\mu p_\mu = (p^0)^2 - (\boldsymbol{p})^2 = m^2$$

. If a four vector's inner product is greater than zero, it is space-like, or if it is negative, it is time-like. A time-like vector connects two events that are causally connected, that is the second event is in the light cone of the first event. A space-like vector connects two events that are causally disconnected, that is the second event is outside the light cone of the first event. The time-like vector and space-like vector can not be transformed to each other by Lorentz transformation. The four-momentum vector of a particle is time like.

The four velocity, $u^\mu = (\gamma, \gamma\boldsymbol{v})$ or $u_\mu = (\gamma, -\gamma\boldsymbol{v})$ is also a time-like vector pointing to the moving direction of particle. Here $\gamma = 1/\sqrt{1 - \boldsymbol{v}^2}$ is the Lorentz factor. Thus, it is normalized to unity: $u^\mu u_\mu = 1$. The classical 3-velocity has a relation with momentum: $\boldsymbol{v} = \boldsymbol{p}/p^0$.

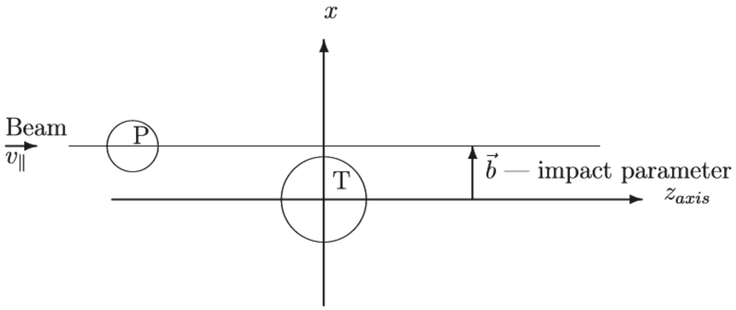

Figure 2.1: The commonly used coordinate system in heavy ion collisions. The z component of a vector is denoted with a subscript $\parallel$.

In high-energy collision physics, the colliding systems are usually analyzed from two directions, i.e. the longitudinal z direction along the projectile and target motion and the transverse plane $[x, y]$. We use subscripts $||$ and $\perp$ to denote these two directions. For example, the three velocity can be decomposed as: $\boldsymbol{v} = (v_{||}, \boldsymbol{v}_{\perp})$. Similarly the four velocity is $u^{\mu} = \gamma(1, v_{||}, \boldsymbol{v}_{\perp})$, and the momentum vector is $p^{\mu} = (p^0, p_{||}, \boldsymbol{p}_{\perp})$. See also in Fig. 2.1.

With the longitudinal velocity $v_{||}$, we define the rapidity of a particle, i.e. $y \equiv \mathrm{arcth}(v_{||})$, which is a generalization of classical 3-velocity. For small velocity, the rapidity approximates to velocity, $y \approx v_{||}$. In specific, the rapidity is defined as:

$$y \equiv \mathrm{arcth}(v_{||}) = \mathrm{arcth}(\frac{p_{||}}{p_0}) = \frac{1}{2}\ln(\frac{p_{||} + p_0}{p_{||} - p_0}) \ .$$

The rapidity y is additive under longitudinal Lorentz transformations. E.g., a particle is measured to has y_1 in frame K_1, and another frame K_2 moves relative to K_1 with rapidity y_2, then the measured rapidity of this particle in frame K_2 is $y = y_1 + y_2$. Thus, the shape of rapidity of the distribution is invariant under Lorentz boosts. Besides, the difference between the rapidities of two particles is invariant with respect to Lorentz boosts along z direction. The two properties result in the crucial role of rapidity in accelerator physics.

However in experiments, the rapidity is difficult to measure, thus a new variable, the pseudorapidity, is introduced:

$$\eta \equiv \frac{1}{2}\ln\frac{|\boldsymbol{p}| + p_{||}}{|\boldsymbol{p}| - p_{||}} = \ln\cot(\frac{\theta}{2}),$$

in terms of the polar angle θ between the momentum of emitted particles and the beam axis, which is measurable in experiments. In high-energy experiments, most particle's momentum is much larger than its rest mass, i.e. $E \approx |\boldsymbol{p}|$, thus $y \approx \eta$.

2.1.2 Macroscopic variables

Considering a colliding system with invariant particle number N, we can define the particle distribution f in the 6 dimensional (x,p) phase space,

$$\Delta N = f(x,p)\Delta^3 x \Delta^3 p \tag{2.1}$$

where δN is the particle number in a phase space volume element $\Delta^3 x \Delta^3 p$. In terms of distribution function, the local density and local current in a given reference frame can be defined as:

$$\mathsf{n(x)} = \int \mathsf{d^3p\, f(x,p)}\ , \tag{2.2}$$

$$\boldsymbol{j}(x) = \int d^3p\, \boldsymbol{v}\, f(x,p), \tag{2.3}$$

Note that $\mathsf{n}(x)$ and $\boldsymbol{j}(x)$ are defined in an arbitrary frame, and depend on $x \equiv x^\mu$, thus they are not invariant under Lorentz boosts. Here the 'local' does not mean 'local rest frame', but indicates these quantities are measured in local space instead of global. E.g. the local density $\mathsf{n}(x)$ is actually the normal density measured in experiments: $\mathsf{n}(x) = \Delta N/\Delta V$. Since the local volume δV is not Lorentz invariant, then the quantity $\mathsf{n}(x)$ is also not an invariant scalar. The characteristic density of a nucleus at rest is $n_0 = 0.145/fm^3$.

Notice that with $\boldsymbol{v} = \boldsymbol{p}/p^0$, the eqs. (2.2) and (2.3) can be united as:

$$N^\mu = \int \frac{d^3p}{p^0}\, p^\mu,\ f(x,p)\ . \tag{2.4}$$

The N^μ is the so called **particle 4-flow**, and it is composed of two components: $N^\mu(x) = (\mathsf{n}(x),\ \boldsymbol{j}(x))$. The particle 4-flow characterizes the current of the matter in the considered system.

Another quantity that characterizes the matter in the system is the **energy-momentum**

tensor, $T^{\mu\nu}$, which is defined by the distribution function as:

$$T^{\mu\nu} = \int d^3p\, p^\mu\, p^\nu\, f(x,p)\,. \tag{2.5}$$

Among all the components, T^{00} is the energy density, T^{0i} is the energy flow, the T^{i0} is the momentum density, and T^{ik} is the momentum flow, where $i, k = 1, 2, 3$.

Notice that fields and potential energy of the particles are not included in this energy momentum tensor, which only contains the rest mass and the kinetic energy. Thus, if particles interact with each other, one should add the contribution of the interaction field into the energy momentum tensor.

With the help of N^μ and $T^{\mu\nu}$, we find two invariant quantities that keep unchanged under Lorentz boost: (1), **Invariant scalar density** n: $n \equiv N^\mu u^\mu$ is the particle density in the Local Rest (LR) frame, $n = N^0_{(LR)}$, which is different from the previous local density n; (2), **Invariant scalar energy density** e: $e = u^\mu T^{\mu\nu} u^\nu$ is the energy density in the local rest frame, $e = T^{00}_{(LR)}$.

Finally, we want to mention the fluid flow and projection operator in hydrodynamics. The flow velocity of a medium, u^μ, is a time-like unit vector parallel to the world-line of the particle. Notice that flow velocity here is distinct with the particle 4-velocity defined previously, it characterizes the collective motion of a particle in a flow medium. The flow velocity is parallel to the energy flow T^{i0} in Landau's definition, which is applicable for very high energies

We define a projector, $\Delta_{\mu\nu}$, which projects a 4 vector into the plane (3-dimensional hypersurface) orthogonal to u^μ:

$$\Delta_{\mu\nu} \equiv g^{\mu\nu} - \frac{u^\mu u^\nu}{u^\mu u_\nu} = g^{\mu\nu} - u^\mu u^\nu\ . \tag{2.6}$$

Now the we have: $\Delta_{\mu\nu} u^\mu = 0$. The prove can be seen in [1].

2.2 Hydrodynamic model

Long before the discovery of Quantum Chromo-dynamics, Landau in 1953 had already applied the ideal hydrodynamics to describe the evolution of matter system generated in high-energy collisions[2]. After many decades, relativistic hydrodynamics has been a dominant research direction in high-energy heavy ion collisions study. The standard thermodynamics requires a global thermodynamic equilibrium, which means some thermodynamical parameters, (P, T, μ) keep unchanged globally. In high energy collisions studies, we assume the system reaches local hydrodynamic equilibrium. A fluid system at local equilibrium is not homogeneous, but the gradients of the intensive quantities (e.g. μ, P, T) are small, and the energy-momentum tensor $T^{\mu\nu}$ is diagonal in the local rest frame. This assumption is becoming more and more realistic because the collision energy and multiplicity are increasing more and more, which makes the massive particles behave collectively as a continuum. The commonly estimated thermalization time in heavy ion collisions is around 0.6 fm/c.

The hydrodynamics begins from the conservation law of charges and energy, momentum:

$$N^{\mu}{}_{,\mu} = 0 \text{ or } \partial_{\mu}(nu^{\mu}) = 0 \ , \tag{2.7}$$

$$T^{\mu\nu}{}_{,\mu} = 0 \text{ or } \partial_{\mu}(T^{\mu\nu}) = 0 \ , \tag{2.8}$$

where the subscript $_{,\mu}$ denotes the four-gradient: $_{,\mu} \equiv \frac{\partial}{\partial x^{\mu}} \equiv \partial_{\mu} \equiv (\partial_t, \nabla_{\boldsymbol{r}})$.

For a viscous fluid the energy-momentum tensor and particle 4-flow can be decomposed as:

$$T^{\mu\nu} = eu^{\mu}u^{\nu} - (P + \Pi)\Delta^{\mu\nu} + \pi^{\mu\nu} \ , \tag{2.9}$$

$$N^{\mu} = nu^{\mu} + S^{\mu} \ , \tag{2.10}$$

where e and p are energy density and pressure in the rest frame of fluid at equilibrium, $\pi^{\mu\nu}$ and Π are the shear stress tensor and bulk pressure, and S^{μ} is the particle diffusion current.

For ideal fluids, the energy momentum tensor and particle 4-flow is reduced to:

$$T^{\mu\nu} = (e+P)u^{\mu}u^{\nu} - Pg^{\mu\nu} \ , \tag{2.11}$$

$$N^{\mu} = nu^{\mu}, \tag{2.12}$$

neglecting the shear stress tensor, bulk pressure and diffusion effect. Specifically, we find that $T^{ik} = \omega\gamma^2 v_i v_k + P\delta_{ik}$, $T^{0i} = -T_{0i} = \omega\gamma^2 v_i$ and $T^{00} = T_{00} = (e+Pv^2)\gamma^2$ where $\omega = e+P$. Here we can introduce the momentum current density $\mathcal{M} \equiv T^{0i}$ and the apparent energy density $\mathcal{E} \equiv T^{00}$. The apparent density can also be introduced as $\mathcal{N} \equiv n\gamma = \mathsf{n}$. By using these three quantities, the fluid dynamic equations take the more familiar form:

$$\partial_t \mathcal{N} + \nabla \cdot (\boldsymbol{v}\mathcal{N}) = 0 \ , \tag{2.13}$$

$$\partial_t \boldsymbol{\mathcal{M}} + \nabla \cdot (\boldsymbol{v}\boldsymbol{\mathcal{M}}) = -\nabla P \ , \tag{2.14}$$

$$\partial_t \mathcal{E} + \nabla \cdot (\boldsymbol{v}\mathcal{E}) = -\nabla \cdot (P\boldsymbol{v}) \ . \tag{2.15}$$

Here Eq. (2.13) is the continuity equation, Eq. (2.14) and Eq. (2.15) are the Euler equation of fluid dynamics and the energy conservation. These fluid dynamic equations can be solved numerically with an Equation of State (EoS): $P = P(n,T)$ or $P = P(n,e)$. One of the commonly used EoS is for non-interacting massless particle: $P = c_0^2 e$, where c_0 is the sound speed in the medium.

2.2.1 Relativistic Boltzmann transport equation (BTE) and Jüttner distribution

Considering particle conservation law, $\partial_\mu N^\mu = 0$, in a 4-dimensional volume element, Δx^4, we have:

$$\int_{\Delta^4 x} \partial_\mu(N^\mu) = \int_{\Delta^4 x}\int_{\Delta^3 p} d^4x\,\frac{d^3p}{p^0}\,p^\mu\,\partial_\mu f(x,p) = 0\,,$$

where $\partial_\mu(p^\mu f) = p^\mu \partial_\mu f$ is used because we assume no collisions between particles and no external force. Since x, p and $\Delta^4 x$, $\Delta^3 p$ is arbitrary, we have:

$$p^\mu \partial_\mu f(x,p) = 0\ . \tag{2.16}$$

This is the relativistic transport equation for the collisionless case. However, collisions between particles change the distribution function, thus the right hand side of Eq. (2.16) is not longer zero. If two uncorrelated particles with initial momentum p_1 and p_2 collide at position x into final momentum $p_1^{'}$ and $p_2^{'}$, then the number of binary collisions is:

$$dN_{coll}(p_1^{'},p_2^{'}\leftarrow p_1,p_2) = d^4x\frac{d^3p_1}{E_1}\frac{d^3p_2}{E_2}\frac{d^3p_1^{'}}{E_1^{'}}\frac{d^3p_2^{'}}{E'_2}f(x,p_1)f(x,p_2)W(p'_1,p'_2\leftarrow p_1,p_2), \tag{2.17}$$

where $W(p_1^{'},p_2^{'} \leftarrow p_1,p_2)$ is the invariant transition rate per unit volume from p_1,p_2 to $p_1^{'},p_2^{'}$. We extract from above equation the term:

$$dN_{coll}^{'}(p'_1,p'_2 \leftarrow p_1,p_2) = \frac{d^3p_2}{E_2}\frac{d^3p_1^{'}}{E'_1}\frac{d^3p_2^{'}}{E'_2}f(x,p_1)f(x,p_2)W(p_1^{'},p'_2 \leftarrow p_1,p_2)\ ,$$

then the number of particles scattering out of and getting into the volume element $\Delta^4 x \Delta^3 p_1$ are

$$\Delta^4 x\frac{\Delta^3 p_1}{E_1}\int dN_{coll}^{'}(p_1^{'},p_2^{'} \leftarrow p_1,p_2) \text{ and } \Delta^4 x\frac{\Delta^3 p_1}{E_1}\int dN_{coll}^{'}(p_1,p_2 \leftarrow p_1^{'},p_2^{'})$$

respectively. Therefore, Eq. (2.16) is corrected to be:

$$\begin{aligned} p^{\mu}\partial_{\mu}f(x,p) &= \frac{1}{2}\int (dN'_{coll}(p_1,p_2 \leftarrow p'_1,p'_2) - dN'_{coll}(p'_1,p'_2 \leftarrow p_1,p_2)) \\ &= \frac{1}{2}\int \frac{d^3p_2}{E_2}\frac{d^3p'_1}{E'_1}\frac{d^3p'_2}{E'_2}[f'_1 f'_2 W(p_1,p_2 \leftarrow p'_1,p'_2) \\ &\qquad -f_1 f_2 W(p'_1,p'_2 \leftarrow p_1,p_2)] \ , \end{aligned} \tag{2.18}$$

where $f'_1 = f(x,p'_1), f'_2 = f(x,p'_2), f_1 = f(x,p_1) f_2 = f(x,p_2)$. This is the well-known relativistic Boltzmann transport equation. The inserted factor $\frac{1}{2}$ comes form the symmetry of exchanging $p_1, p_2 \leftrightarrow p'_1, p'_2$.

The stationary solution of the Relativistic BTE is called the Jüttner distribution, which is a globally equilibrium distribution function:

$$f^{J\ddot{u}ttner}(p) = \frac{1}{(2\pi\hbar)^3}\exp\frac{\mu - p^{\nu}u_{\nu}}{T} \ , \tag{2.19}$$

where μ is the chemical potential, T is temperature. Since $p^{\nu}u_{\nu}$, as well as μ and T, are scalars, the Jüttner distribution is Lorentz invariant. It has familiar generalizations to Bose-Einstein and Fermi-Dirac statistics. Any other solution of BTE should tend to $f^{J\ddot{u}ttner}(x,p)$. Most of the time the local particle distribution $f(x,p)$ is close to $f^{J\ddot{u}ttner}$ since the equilibrium stage can be reached very fast.

The ideal hydrodynamics does not require global equilibrium, but local equilibrium, thus an x dependent Jüttner distribution

$$f^{J\ddot{u}ttner}(x,p) = \frac{1}{(2\pi\hbar)^3}\exp\frac{\mu(x) - p^{\nu}u_{\nu}(x)}{T(x)} \ . \tag{2.20}$$

is assumed to be the prerequisite of perfect fluid dynamics, i.e. the system is not homogeneous but has a small gradient, as discussed in the beginning of this section.

2.2.2 The Particle in Cell (PIC) method

The PIC method is a widely used approach to numerically solve differential equations. The hydrodynamic model in this thesis is also based on the PIC method. In our simulation the space is divided into many grid cells and millions of marker particles are filled in the cells. The marker particles are just fictitiously designed to represent a small part of the flow and its mass and energy. It has nothing to do with real nucleons. We might call it ‘flow particles’. The cell structure of our computational fluid dynamics is shown in Appendix A.

To numerically solve the fluid dynamic equations, there are two kinds of computational reference frames (or computational grid), the Eulerian grid and the Lagrangian grid. The Eulerian grid is fixed in space and accounts for the storage of momentum, energy and particles. The fluid can move across these grid cells thus the number of cells filled with matter is increasing as the system is expanding. On the other hand, the Lagrangian mesh cells move with the fluid, thus the fluid does not flow in or out of these cells. The Marker Particles in our model are de facto the Lagrangian cells. Thus, our model is the combination of Eulerian method and Lagrangian method.

The Euler equations are solved in three steps. Firstly, we ignore the convective parts of the Euler equations, then Eqs. (2.13, 2.14, 2.15) become:

$$\frac{\partial N}{\partial t} = 0, \ \frac{\partial \boldsymbol{M}}{\partial t} = -\nabla p, \ \frac{\partial E}{\partial t} = -\nabla (p\boldsymbol{v}). \tag{2.21}$$

In this step, there is no transport between neighboring Eulerian cells.

In the second step, we need to consider the transport properties between the bigger Eulerian cells. The cell momentum and energy are distributed evenly among all the particles in this Eulerian cell, thus each Marker Particle (=Lagrangian cell) has an effective velocity, $\overline{v}_{i,j,k}$. In δt time each Marker Particle moves a distance $\overline{v}_{i,j,k}\delta t$. After a movement if the Marker Particle remains in the same cell, the energy and momentum of this Eulerian cell does not change (this is the origin of numerical viscosity in our hydrodynamic model); If it crosses the Eulerian cell boundary, the momentum and energy carried by this marker particle should be added to its new Eulerian cell and subtracted from the old one.

After the above two steps, each cell has new values of energy and momentum. The new rest-frame density n, pressure p and velocity $\boldsymbol{v}$ must be calculated, to prepare for the execution of next iteration. It is in this step that considerable errors might occur. The problem arises from the surface cells of the fluid system. Assume that a cell with 4^3 maker particles will have a normal density, n_0. If, e.g. a surface cell contains 32 marker particles, does this imply the density is $\frac{1}{2}n_0$? However the marker particles might not evenly distributed in all cells but occupy only a small volume close to the interior cells, so that the true density is larger than n_0. In essence, it is because the true surface of the nuclear matter is not the edges of the cell. At initial stage, the surface to volume ratio is small, the problem is not so problematic. However, with the expansion of fluid system, there are more and more surface cells and thus the simulation becomes far away from reality. This is the reason why the hydrodynamic simulation becomes invalid at the later stage of expansion.

2.3 Initial state and freeze out

The heavy ion collisions are usually divided into four stages, the initial stage, QGP stage, hadronization and hadron rescattering. The hydrodynamics is a powerful prescription for the second stage, but the initial stage and the hadron cascade are out of the applicability of hydrodynamics. The hadron cascade stage has been well described by kinetic models. Nowadays, people are more and more aware of the importance of the initial state, because the final state can be very different for different initial state. The initial state used in this thesis is developed by [3], where for non central collisions the system after impact is tilted and thus carries a substantial angular momentum. This angular momentum will lead to a rotating system, and then new interesting phenomenons, such as chiral vortical effect and hyperon polarization may occur. The detailed discussion about the initial state in [3] and its development can be seen in Section 4.2 and Chapter 5.

A hydrodynamic model can simulate the collision and calculate the post freeze out measurables, which can be used to compare with the experimental data. It is not an easy task to properly break up the hydrodynamic evolution and obtained the correct measurables. Although a continuous freeze out process can be implemented in fluid dynamics by introducing source and drain terms, the most widely applied process is sudden freeze out(FO).

In our model, the matter suffers a sudden freeze out by crossing a three dimensional time-like hypersurface, where the energy and momentum may change discontinuously. This discontinuity can be neglected if the pressure at the breakup is small or the flow is orthogonal to the FO surface. After freeze out, the continuum becomes independent particles, and final interactions and collisions are neglected among these particles.

Considering a FO hypersurface S with normal vector $d\sigma^\mu$, on the both sides of the discontinuity we have Rankine-Hugoniot conditions:

$$[N^\mu d\sigma_\mu] = 0 \ , \ [T^{\mu\nu} d\sigma_\mu] = 0 \ , \ [s^\mu d\sigma_\mu] \geq 0 \ , \tag{2.22}$$

where the square brackets $[q] = q_1 - q_2$ denote the quantity difference before and after the discontinuity. These equations imply the conservation of some quantities, e.g. total particle number, energy and momentum, while the four current N^μ and energy momentum tensor $T^{\mu\nu}$ are not continuous across the surface.

The flow velocity will also change if its direction is not parallel to the freeze out surface normal ($d\sigma^\mu$). This modifies the freeze out method of Cooper and Frye [4] because even if the direction is the same as the surface normal but with different EoS, the parameters of post-freeze out matter will also change, such as the temperature, since the particle interaction energy should be added to the kinetic energy of non-interacting particles [5].

By Eqs.(2.22), the post freeze out quantities, N^μ and $T^{\mu\nu}$ can be determined if the surface is chosen and the pre freeze out quantities N_0^μ, $T_0^{\mu\nu}$ are known. To determine the FO hypersurface from the solution of hydrodynamic problem is very involved, thus it is usually prescribed directly. From the N^μ and $T^{\mu\nu}$, we can determine the particle distribution, e.g. for ideal gas we have:

$$N^\mu = \int \frac{d^3p}{p^0}\, f_0(x,p)\ ,$$

where f_0 is the phase space distribution of the ideal gas. Once the distribution function is known, we can calculate many quantities that can be measured in experiments, such as the total particle number: $N = \int_S N^\mu d\sigma_\mu$. Frequently we simply assume that the normal of FO hypersurface is parallel to the flow velocity, $u^\mu = d\sigma^\mu$, which is usually satisfied in the models with spherical or cylindrical symmetry.

On the other hand, the experimental measurables are usually differential quantities normalized per event, such as the quantity ($\boldsymbol{dN/d^3p}$), satisfying the normalization

$$N = \int_S \frac{dN}{d^3p} d^3p = \int_S \left(\int \frac{d^3p}{p^0} p^\mu f_0(x,p) \right) d\sigma_\mu = \int_S n(x) u^\mu d\sigma_\mu\ , \tag{2.23}$$

Similarly, the overall transverse momentum in reaction plane (RP) is

$$p^x_{tot} = \int_S \frac{dN}{d^3p} p^x d^3p = \int_S \left(\int \frac{d^3p}{p^0} p^\mu p^x f_0(x,p) \right) d\sigma_\mu = \int_S T^{\mu x} d\sigma_\mu\ . \tag{2.24}$$

Some most common measurables are the baryon and pion measurables. The local baryon momentum space distribution assumes the Jüttner distribution, and the local pion distribution assumes a Relativistic Bose distribution:

$$f_\pi(x,p) = \frac{g_\pi}{(2\pi\hbar)^3} \frac{1}{\exp\frac{p^\mu u_\mu}{T} - 1}\ .$$

In both cases there are several measurables, such as rapidity distribution $\frac{dN_{\rm cell}}{dy}$, the transverse momentum spectra $\frac{dN_{\rm cell}}{p_\perp dp_\perp}$, collective sidewards flow $\frac{dp^x_{\rm cell}}{dy}$, and the average transverse momentum $\frac{dN_{\perp,\mathrm{cell}}}{dy}$.

It is important to mention that in Eqs. (2.23, 2.24), the post freeze out phase space distribution of particles $f(x,p)$ should not include particles which propagate backwards into the mater and do not freeze out yet. To avoid these "negative contributions" one should use the cut Jüttner [6] or cancelling Jüttner [7, 8] distributions as post freeze out distributions.

see more details in [1].

Chapter 3

Polarization in non-relativistic limit

In high energy peripheral heavy ion collisions there is a substantial amount of initial angular momentum directly after the Lorentz contracted nuclei penetrate each other [3]. The formed Quark Gluon Plasma locally equilibrates, the shear flow leads to local rotation, i.e. vorticity, and then it expands, while its rotation slows down. Early simulation studies neglected effects arising from the non-vanishing angular momentum, but much interest has increased recently [9–12]. With non-vanishing viscosity, in peripheral collisions the initial shear flow leads to an order of magnitude larger vorticity [13]. This vorticity may be further enhanced by the Kelvin Helmholtz Instability (KHI). The Λ polarization is one of the experimental signals indicating the rotation and vorticity in heavy ion collisions.

Previously, we calibrated an exact rotating model based on a (3+1)D fluid dynamical model, the relativistic particle-in-cell method (PICR), to fine-tune the initial parameters of the rotating and expanding fireball [14]. Thus, based on the exact model in Ref. [15], we develop an analytic solution for Λ polarization in non-relativistic limit, and calculate the polarization magnitude and structure.

3.1 The Exact rotating fluid dynamical model

By including rotation effect, Ref. [14] is applied and extended to an exact solution of fluid dynamics of heavy ion collisions, to estimate the rate of slowing down of rotation due to the system expansion. This model entails after a realistic (3+1)-dimensional hydrodynamic simulation at 2.76 TeV, where the Kelvin-Helmholtz instability may exist to enhance the rotation.

Ref. [14] assumed azimuthal symmetry, and uses the cylindrical coordinates in spatial dimensions $(r_\rho = \rho, r_\phi = \rho\phi, r_y = y)$, which are respectively called 'out, side, long' directions. The boundary values of these coordinates are $(R,\ S,\ Y)$. Then the scaling variable s is introduced and its components are defined in terms of cylindrical coordinates :

$$s_\rho = r_\rho^2/R^2,\ s_\phi = r_\phi^2/S^2 = r_\rho^2/R^2,\ s_y = r_y^2/Y^2\,,$$

where $S = R\phi$ is the roll length on the outside circumference. Due to the azimuthal symmetry in this case, the scaling variable s is re-defined as:

$$s \equiv s_\rho + s_y = \frac{x^2 + y^2}{R^2} + \frac{y^2}{Y^2}\ .$$

Different from Ref. [16], here the y- and z-axes are interchanged to resonate with choice of axes in heavy ion collision literature, in which the reaction plane, in which the system rotates, is spanned by $\boldsymbol{e}_x$ and $\boldsymbol{e}_z$, leaving the axis of rotation to be defined by $\boldsymbol{e}_y$. In the above equation, we have $r = \sqrt{x^2 + z^2}$ with an equation of motion, $\dot{\boldsymbol{r}}(t) = \boldsymbol{v}(\boldsymbol{r}, t)$. Then a linear velocity profile both in the radial, r, and in the axial, y, directions was assumed. This leads to a flow development where a fluid element starting from a point (r_0, y_0, ϕ_0), and at a later time, t, reaches the point

$$\begin{aligned} r(t) &= r_0 \frac{R(t)}{R(t_0)}, \\ y(t) &= y_0 \frac{Y(t)}{Y(t_0)}, \\ \phi(t) &= \phi_0 + \int dt\, \omega(t), \end{aligned} \tag{3.1}$$

showing explicitly how the solutions evolve with time, in a rotating and expanding fluid. These equations follow the time-evolution of the scaling variables in the radial and axial directions. This is a Cylindrically symmetric setup with $X(t) = Z(t)$, $\sqrt{X^2(t) + Z^2(t)} = R(t)$ and, in general, $Y(t) \neq R(t)$.

From the Euler equation:

$$n\, m(\partial_t + \boldsymbol{v}\nabla)\boldsymbol{v} = -\nabla p \ ,$$

where the thermodynamic variables of system, e.g. temperature, T, and particle density, n, are assumed to be time-independent distributions with respect to the scaling variable s:

$$\begin{aligned} T &= T_0 \left(\frac{V_0}{V}\nu(s)\right)^{1/\kappa} \tau(s) \ , n(s) = n_0 \frac{V_0}{V} e^{-\frac{1}{2}s} \\ \nu(s) &= \frac{1}{\tau(s)} \exp\left(-\frac{1}{2}\int_0^s \frac{du}{\tau(u)}\right) \\ &= 1 \cdot \exp\left(-\frac{1}{2}\int_0^s du\right) \ , \end{aligned}$$

one can find the ordinary differential equation:

$$R\ddot{R} - W/R^2 = Y/\ddot{Y} = \frac{T_0}{m}(\frac{V_0}{V})^{\gamma} \ , \tag{3.2}$$

where γ is the Lorentz factor and $W \equiv \omega_0^2 R_0^4$ with the subscript '0' denoting the quantity at initial time. Here the EoS is simply assumed to be:

$$\epsilon = \kappa p \ and \ p = nT \ ,$$

where κ is a constant.

Then by requiring the energy conservation, Ref [14] finally obtained the exact solution for the differential equation (3.2), and showed the rate of decrease of angular speed and rotational energy due to the explosively longitudinal and transverse expansion.

3.2 Relativistic thermodynamics with spin

Considering a rotating relativistic gas system at global equilibrium, with finite angular momentum $\boldsymbol{J}$, chemical potential μ and temperature T, then the density operator $\hat{\rho}$ which contains the whole physics of this system, should be supplemented by a rotation term:

$$\hat{\rho} = \frac{1}{Z} \exp\Big[- \hat{H}/T + \omega \hat{\boldsymbol{J}} + \mu \hat{Q} \Big] \ ,$$

where $Z = tr(\exp[-\hat{H}/T + \omega\hat{\boldsymbol{J}} + \mu\hat{Q}])$ is the partition function. In the Boltzmann limit, the particles are distinguishable and thus the above partition function can be viewed as the product of partition functions of a single particle. By projecting the density operator of single-particle into the polarization states (denoted by r and s): $< p, s| \ \rho \ |p, r >$, the phase space distribution of single-particle can be obtained [17]:

$$f(x,p)_{rs} = \frac{1}{2} \exp(\xi - \beta^{\mu} p_{\mu}) \ \ \Big[D^S([p]^{-1} R_{\omega}(i\omega/T)[p]) + D^S([p]^{\dagger} R_{\omega}(i\omega/T)[p]^{\dagger -1} \Big]_{rs} \ ,$$

where $\beta^{\mu} = u^{\mu}/T = (1, \boldsymbol{\omega} \times \boldsymbol{x})$ is the inverse temperature four-vector, $\xi = \mu/T$ is the chemical potential μ divided by temperature T, $R_{\omega}(i\omega/T)$ is a rotation operation of an angle $\phi = i\omega/T$ around the axis of angular velocity ω, $[p] \in SL(2, C)$ denotes the Lorentz transformation taking the time-like vector $m\hat{t} = (m, 0, 0, 0)$ to p, and D^S is the representation of the SL(2,C) group.

For the spin 1/2 Fermi-Dirac statistics in Boltzmann limit, the single-particle distribution can be reduced as:

$$f(x,p) = \frac{1}{2m}\bar{U}(p)\Big(\exp[\xi - \beta^{\mu}p_{\mu}]\exp[\frac{1}{2}\omega^{\mu\nu}\Sigma_{\mu\nu} + I]\Big)U(p) \ ,$$

where $U(p) = (u_{+}(p), u_{-}(p))$ consists of two spinsors $u_{+}(p)$ and $u_{-}(p)$ with normalization of $u_r\bar{u}_r = 2m$ ($\bar{U}(p) = U^{\dagger}(p)\gamma^0$); $\Sigma^{\mu\nu} = (i/4)[\gamma^{\mu}, \gamma^{\nu}]$ are the generators of Lorentz transformation of spinsors; $\omega^{\mu\nu} = (\omega/T)(\delta^1_{\mu}\delta^2_{\nu} - \delta^1_{\nu}\delta^2_{\mu})$ is a tensor that can be proved to be the vorticity tensor divided by temperature. In fact, by requiring global equilibrium and the conservation of angular momentum, Ref. [18] found that $\omega^{\mu\nu} = -\frac{1}{2}(\partial_{\mu}\beta_{\nu} - \partial_{\nu}\beta_{\mu})$, and thus it is called 'thermal vorticity'. For local equilibrium, the single-particle distribution should depend on x also, and the above equation is modified to be:

$$f(x,p) = \frac{1}{2m}\bar{U}(p)\Big(\exp[\beta(x)^{\mu}p_{\mu} - \xi(x)]\exp[-\frac{1}{2}\omega(x)^{\mu\nu}\Sigma_{\mu\nu} + I]\Big)^{-1} U(p) \ , \tag{3.3}$$

Similarly, for the antiparticles, the single-particle distribution reads:

$$f(x,p) = -\frac{1}{2m}\Bigg(\bar{V}(p)\Big(\exp[\beta(x)^{\mu}p_{\mu} + \xi(x)]\exp[\frac{1}{2}\omega(x)^{\mu\nu}\Sigma_{\mu\nu} + I]\Big)^{-1} V(p)\Bigg)^{T} \ , \tag{3.4}$$

where $V(p) = (v_{+}(p), v_{-}(p))$ also consists of two spinsors $v_{+}(p)$ and $v_{-}(p)$ for anti-particles with normalization of $u_r\bar{u}_r = 2m$. Then the energy momentum tensor and four current are:

$$\begin{aligned} T^{\mu\nu} &= \int \frac{d^3p}{\epsilon}p^{\mu}p^{\nu}(tr_2 f + tr_2\bar{f}) = \frac{1}{2}\int \frac{d^3p}{\epsilon}p^{\mu}p^{\nu}(trX + tr\bar{X}) \ , && (3.5) \\ N^{\mu} &= \frac{1}{2}\int \frac{d^3p}{\epsilon}p^{\mu}(trX - tr\bar{X}), && (3.6) \end{aligned}$$

where the symbol tr_2 denotes summing over the polarization states r and s, the tr

without subscript is ordinary trace operation , and the extracted term:

$$X = \Big(\exp[\beta(x)^{\mu} p_{\mu} - \xi(x)] \exp[-\frac{1}{2}\omega(x)^{\mu\nu}\Sigma_{\mu\nu} + I] \Big)^{-1} \ ,$$

$$\bar{X} = \Big(\exp[\beta(x)^{\mu} p_{\mu} + \xi(x)] \exp[\frac{1}{2}\omega(x)^{\mu\nu}\Sigma_{\mu\nu} + I] \Big)^{-1} \ .$$

The canonical spin tensor can also be calculated through the distribution function:

$$\begin{aligned} S^{\lambda,\mu\nu} &\equiv tr\big(\bar{\Psi}\frac{1}{2}\{\gamma^{\lambda}, \Sigma^{\mu\nu}\}\Psi\big) \\ &= \frac{1}{2}\int \frac{d^3p}{2\epsilon} tr_2(f(x,p)\bar{U}\{\gamma^{\lambda}, \Sigma^{\mu\nu}\}U) - tr_2(\bar{f}^T(x,p)\bar{(V)}\{\gamma^{\lambda}, \Sigma^{\mu\nu}\}V) \\ &= \frac{1}{2}\int \frac{d^3p}{\epsilon}(p^{\lambda}\Theta^{\mu\nu} + p^{\nu}\Theta^{\lambda\mu} + p^{\mu}\Theta^{\nu\lambda} + p^{\lambda}\bar{\Theta}^{\mu\nu} + p^{\nu}\bar{\Theta}^{\lambda\mu} + p^{\mu}\bar{\Theta}^{\nu\lambda}) \end{aligned} \tag{3.7}$$

where $\Theta^{\mu\nu} = tr(X\Sigma^{\mu\nu})$ and $\bar{\Theta}^{\mu\nu} = -tr(\bar{X}\Sigma^{\mu\nu})$. Finally, Ref. [15] defined the polarization four-vector, also named as Pauli-Lubanski pseudovector:

$$\Pi_{\mu} = -\frac{1}{2}\epsilon_{\mu\rho\sigma\tau} J^{\rho\sigma} \frac{p^{\tau}}{m} \ , \tag{3.8}$$

where $\epsilon_{\mu\rho\sigma\tau}$ is the four-dimensional totally antisymmetric Levi-Civita symbol, $J^{\rho\sigma}$ is the relativistic total angular momentum. The average polarization is obtained by dividing the total angular momentum density, $dJ^{0,\rho\sigma}(x,p)/d^3p$, by the particle density, $tr_2 f$, in the phase space [x, p]:

$$< \Pi_{\mu}(x,p) >= -\frac{1}{2}\epsilon_{\mu\rho\sigma\tau} \frac{dJ^{0,\rho\sigma}(x,p)}{d^3p} \frac{1}{tr_2 f} \frac{p^{\tau}}{m} \ .$$

Furthermore the total angular momentum, $J^{\lambda,\rho\sigma}$, is defined as:

$$J^{\lambda,\rho\sigma} = x^{\rho} T^{\lambda\sigma} - x^{\sigma} T^{\lambda\rho} + S^{\lambda,\rho\sigma}(x) \ ,$$

thus the density of total angular momentum is:

$$\frac{dJ^{0,\rho\sigma}(x,p)}{d^3p} = (x^\rho p^\sigma - x^\sigma p^\rho) tr_2 f(x,p) + \frac{dS^{0,\rho\sigma}(x,p)}{d^3p} \ ,$$

where the Levi-Civita tensor will eliminate the first term, i.e. the orbital angular momentum density, remaining the spin angular momentum density only. Therefore, the average polarization four-vector for particles becomes:

$$< \Pi_\mu(x,p) >= -\frac{1}{4tr_2 f}\epsilon_{\mu\rho\sigma\tau}\frac{1}{\epsilon}(p^0\Theta^{\rho\sigma} + p^\sigma\Theta^{0\rho} + p^\rho\Theta^{\sigma 0})\frac{p^\tau}{m} = -\frac{1}{2trX}\epsilon_{\mu\rho\sigma\tau}\Theta^{\rho\sigma}\frac{p^\tau}{m} \quad (3.9)$$

and at the lowest order of $\omega^{\mu\nu}$, we have:

$$< \Pi_\mu(x,p) >\approx -\frac{1}{8}\epsilon_{\mu\rho\sigma\tau}(1-n_F)\omega^{\rho\sigma}(x)\frac{p^\tau}{m} \ , \quad (3.10)$$

where

$$n_F = \frac{1}{e^{\beta(x)p-\xi}+1}$$

is the Fermi-Jüttner distribution.

For the antiparticles, the formula is the same by replacing n_F with $\bar{n}_F$. Therefore, one can see that, the direction of polarization vector for particles and antiparticles in this method is identical, which is opposed to electromagnetic phenomena. This result stems from the charge conjugation of the spin tensor $S^{\lambda,\rho\sigma}$.

With $\omega_{\mu\nu} = -\frac{1}{2}(\partial_\mu\beta_\nu - \partial_\nu\beta_\mu)$, the polarization vector can be decomposed into time and spatial components:

$$\Pi = (\Pi^0, \mathbf{\Pi}) = \frac{1-n_F}{8m}\Big((\nabla\times\beta)\cdot\boldsymbol{p},\ \epsilon(\nabla\times\beta) - \partial_t\beta\times\boldsymbol{p} - \nabla\beta^0\times\boldsymbol{p}\Big) \ . \quad (3.11)$$

In relativistic heavy ion collisions, it is interesting to calculate the average of spatial component of polarization vector. For example, we integrate the Λ's polarization vector over some volume, and ultimately over all of space, weighted by the number density, normalized by number of particles in that volume, leaving a momentum-dependent polarization four-vector in the participant frame of reference

$$\Pi_\mu(p) = \hbar\epsilon_{\mu\sigma\rho\tau}\frac{p^\tau}{8m}\frac{\int d\Sigma_\lambda p^\lambda n_F(x,p)(1-n_F(x,p))\partial^\rho\beta^\sigma}{\int d\Sigma_\lambda p^\lambda n_F(x,p)} \ . \tag{3.12}$$

Besides, in experiments, the Λ polarization is determined by measuring the angular distribution of the decay protons in the Λ's rest frame. In this frame the Λ polarization is $\mathbf{\Pi}_0(\boldsymbol{p})$, which can be obtained by Lorentz boosting the polarization $\mathbf{\Pi}(\boldsymbol{p})$ from the participant frame to the Λ's rest frame, [19],

$$\mathbf{\Pi}_0(\boldsymbol{p}) = \mathbf{\Pi}(p) - \frac{\boldsymbol{p}}{p^0(p^0+m)}\mathbf{\Pi}(p)\cdot\boldsymbol{p} \ , \tag{3.13}$$

where $(p^0, \boldsymbol{p})$ is the Λ's four-momentum and m its mass.

3.3 Solution for the Λ polarization vector

As the Λ is transversely polarized, $\Pi^\mu p_\mu = 0$, one can confine himself to the spatial part of Π^μ. From equation (3.11), the simplified spatial part of polarization vector is:

$$\mathbf{\Pi}(p) = \frac{\hbar\epsilon}{8m}\frac{\int dV n_F(x,p)\,(\nabla\times\boldsymbol{\beta})}{\int dV n_F(x,p)} + \frac{\hbar\boldsymbol{p}}{8m}\times\frac{\int dV n_F(x,p)\,(\partial_t\boldsymbol{\beta}+\nabla\beta^0)}{\int dV n_F(x,p)} \ . \tag{3.14}$$

where $n_F(x,p)$ is the phase space distribution of the Λs. In a previous calculation [19], the p dependence of n_F, was considered negligible in the integral and the time derivative and gradient terms were also assumed to be smaller. The present calculation shows that in general these terms are not negligible and that which terms are dominant depends on the particular conditions.

The detailed deduction of an analytic solution for Λ polarization in non-relativistic limits is shown in Appendix B, here we just extract the final result, i.e. the analytical formula for Λ polarization in non-relativistic limits:

$$\mathbf{\Pi}(p) = \frac{\hbar}{8mT}\left[\frac{p_y c_9}{c_3\sqrt{c_4}}\frac{M_{-1,\frac{1}{2}}}{M_{-\frac{1}{2},0}}\boldsymbol{e}_x + \Big(2\epsilon\omega - \frac{|p_x|c_9}{c_3\sqrt{c_4}} \times \frac{M_{-1,\frac{1}{2}}}{M_{-\frac{1}{2},0}}\Big)\boldsymbol{e}_y + \Big(\frac{|p_x|c_7c_1}{2c_2} - \frac{p_y c_8}{c_3\sqrt{c_4}}\frac{M_{-1,\frac{1}{2}}}{M_{-\frac{1}{2},0}}\Big)\boldsymbol{e}_z\right] \quad (3.15)$$

where $c_{1,2...,9}$ are given parameters (see specific definitions in Appendix B), and $M_{a,b}(x)$ is the so called ‘Whittaker Function’.

We adopt the parametrization of the model from Ref. [20], with the initial conditions $R_0 = 2.5$ fm, $Y_0 = 4.0$ fm, $\dot{R}_0 = 0.20$ c, $\dot{Y}_0 = 0.25$ c, $\omega_0 = 0.1$ c/fm, $\kappa = 3/2$, $T_0 = 300$ MeV. For this configuration $E_{tot} = 576$ MeV/nucl. After hydrodynamic evolution in the Exact rotating model, we calculate the Λ polarization of the system, according to the analytic solution of equation (3.15), and show the results in the next section.

3.4 Results and Analysis

Notice that Eq. (3.15) is the analytical solution in the non-relativistic limit. The 'Whittaker Function', $M_{\mu,\nu}(z)$, is the confluent hypergeometric function. For the relativistic case, the integrations of the Λ-polarization vector cannot be performed analytically, because of the presence of $\gamma = 1/\sqrt{1 - v_r^2 - v_y^2 - v_\phi^2}$, which will make the integrations more involved. Thus, a numerical solution for the Λ-polarization would be needed.

The effect of vorticity is shown in Fig. 3.1. The non-relativistic Exact model can handle reactions with modest energy and modest rotation, so the overall vorticity and the resulting polarization is not too large. Furthermore the rotation and vorticity decrease with time while the radial and axial expansion increases. This expansion leads to the second term of polarization in Eq. (4.2), $\mathbf{\Pi}_2$, which depends on $\partial_t\boldsymbol{\beta}$ (while the $\boldsymbol{\nabla}\beta^0$ terms vanishes in the non-relativistic approximation). Due to the simplicity of the Exact model, the vorticity arising from the shear flow of the peripheral initial state is constant in space and depends on the time only. However, due to the construction of thermal vorticity, both the angular momentum and the temperature in the denominator decrease with time, thus $\nabla \times \boldsymbol{\beta}$ is hardly decreasing with the time, and it has a significant value,

-0.13, in natural units. At the same time in this model the time-dependent vorticity is smaller by almost an order of magnitude. The time-dependent vorticity components also decrease faster than the one originating from the initial shear flow.

Nevertheless the second term in the polarization is of comparable magnitude to the term arising from local vorticity. See Fig. 3.1 (right panel).

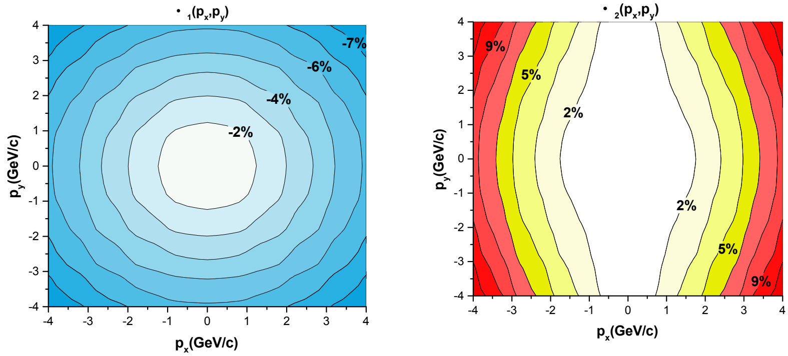

Figure 3.1: (color online) The left panel and right panel are respectively the first term, $\mathbf{\Pi}_1(\boldsymbol{p})$, and the absolute value of second term, $\mathbf{\Pi}_2(\boldsymbol{p})$, of Λ polarization , in the participant Center of Mass (CM) frame at time $t = 0.5$ fm/c after the equilibration of the rotation, in the Exact model. The first term, $\mathbf{\Pi}_1(\boldsymbol{p})$, points into the $-y$-direction and changes from -1.5% at the CM-momentum ($p_x = p_y = 0$), to -8% in the corners, in 1% steps per contour line. The negative percentage indicates that the polarization is in the $-y$-direction. The structure is just like that of the energy weighted vorticity. Due to azimuthal symmetry of the Exact Model the p_x and p_z dependence of $\mathbf{\Pi}$ are the same.The second term, $\mathbf{\Pi}_2(\boldsymbol{p})$, changes from zero at the CM-momentum ($p_x = p_y = 0$), up to 20% in the corners at $p_x = -4$GeV/c, in 2.5% steps per contour line. In the corners at $p_x = 4$GeV/c, the polarization is 12%. The second term $\mathbf{\Pi}_2(\boldsymbol{p})$ is orthogonal to $\boldsymbol{p}$, and it is smaller, especially at CM-momenta, where it is negligible. This term arises from the expansion, which is increasing rapidly in the Exact model with time and also increases with the radius. At large radius the larger expansion leads to larger momenta. The structure of the 2nd component of polarization arises from the asymmetries of the different components of $\mathbf{\Pi}_2(\boldsymbol{p})$.

The presented plots are such that p_x points into the direction of the observed Λ-particle, while the p_y is the axis direction. All results should be either symmetric or antisymmetric for a $\pm p_y$ change. On the other hand reversing the p_x axis must not change the data, as the x-axis is chosen to be the direction of the argument of $\mathbf{\Pi}(\boldsymbol{p})$, which must be azimuthally symmetric in the $[x, y]$-plane.

The polarization arising from the dynamics of the radial and spherical expansion, $\mathbf{\Pi}_2$, was not discussed before in the literature, as the dominance of the vorticity effect was anticipated and studied up to now. The $\mathbf{\Pi}_2$ plots in Figs. 3.1, 3.2, 3.3, show the components of the polarization arising from the dynamics of the spherical expansion. The most interesting y-component arises from the x-component of the momentum and the z-component of the thermal velocity change $\dot{\beta}_z$ (left panel of Fig. 3.2).

Now if we study the axis directed components, this is given by $\Pi_y = \Pi_{1y} + \Pi_{2y}$. Both these terms have a negative maxima of the same magnitude, -8%, at the corners, $p_x, p_y = \pm 4$GeV/c, thus these terms add up constructively and result in Λ-particle polarizations reaching -16% at high momenta. At small momenta the polarization is still the same sign but has a reduced value of the order of 1.5% arising from the vorticity (right panel of Fig. 3.2).

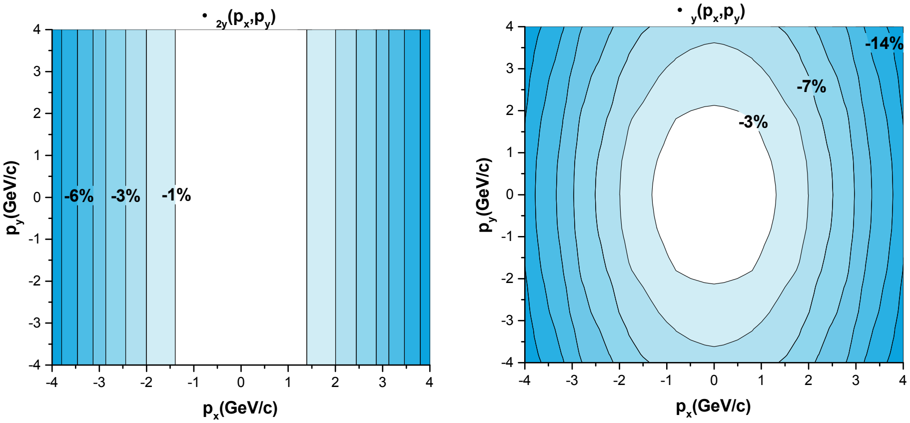

Figure 3.2: (color online) The left panel is the second term's y-component of Λ-polarization, $\mathbf{\Pi}_2(\boldsymbol{p})$, and the right panel is the complete y-component containing both the first term and second term of the polarization, $\mathbf{\Pi}_2(\boldsymbol{p})$. Both are in the participant Center of Mass (CM) frame at time $t = 0.5$ fm/c after the equilibration of the rotation, in the Exact model. The $\mathbf{\Pi}_2(\boldsymbol{p})$ does not depend of p_y, as shown in Eq. (B.30).

In this Exact model the x and z components of the polarization arise only from the second term, $\mathbf{\Pi}_2(\boldsymbol{p})$. The x component is reaching ±8%, while the z component is smaller, it reaches about ±3%. These both are asymmetric for $\pm p_y$ change, and show an opposite symmetry. The x-component is proportional to p_y and the dynamics of radial expansion. Thus, it follows the signature of p_y, (see left panel of Fig. 3.3). The z-component is proportional to p_y and the dynamics of radial expansion, thus it follows the signature of p_y (right pannel of Fig. 3.3). The z-component is proportional to $p_x\dot{\beta}_y$ and inversely proportional to $p_y\dot{\beta}_x$ (see right panel of Fig. 3.3). These two effects compensate each other so the maxima of the polarization are smaller and the symmetry is opposite to that of the x-component. This term is sensitive to the balance between the axial expansion and the radial expansion in the model.

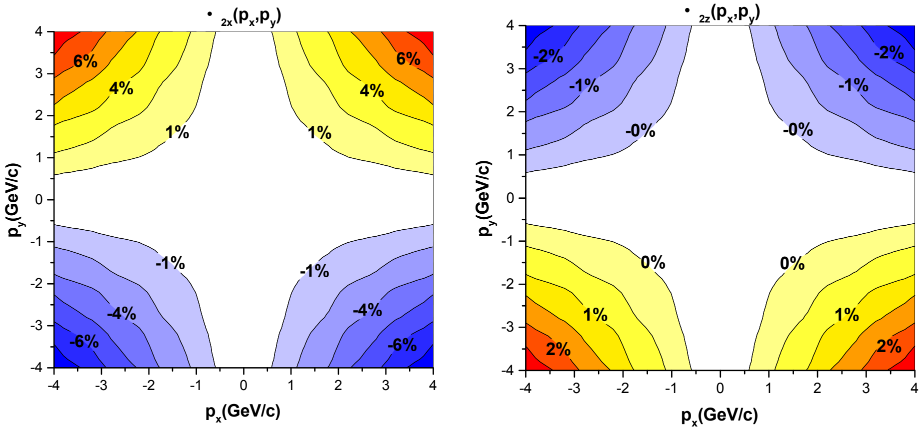

Figure 3.3: (color online) The x (left) and z (right) components of the Λ-polarization, $\mathbf{\Pi}_{2x}(\boldsymbol{p})$ and $\mathbf{\Pi}_{2z}(\boldsymbol{p})$, in the participant Center of Mass (CM) frame for the second term containing the $(\partial_t\boldsymbol{\beta})$-contribution, at time $t = 0.5$ fm/c after the equilibration of the rotation, in the Exact model. The polarization vanishes at the CM-momentum ($p_x = p_y = 0$), and changes from zero up or down in the corners. These two terms arise from the expansion, which is increasing rapidly in the Exact model with time and also increases with the radius. At large radius the larger expansion leads to larger momenta.

The Λ polarization is measured via the angular distribution of the decay protons in the Λ's rest frame, as shown in Eq. 3.13. The resulting distribution is shown in Fig. (3.4). This new study indicates that the dynamics of the expansion may lead to non-negligible contribution to the observable polarization. The structure of $\Pi_{0y}(\boldsymbol{p})$ is similar to the one obtained in Ref. [19], but here the contribution of the "second", $\partial_t\boldsymbol{\beta}$ term is also included, which makes the y-directed polarization stronger at high p_x values, 12%, while it was 9% in Ref. [19], both in the negative y-direction. Furthermore, the second term changes the structure, of the momentum dependence of $\Pi_{0y}(\boldsymbol{p})$, and it becomes $\pm p_x$ asymmetric.

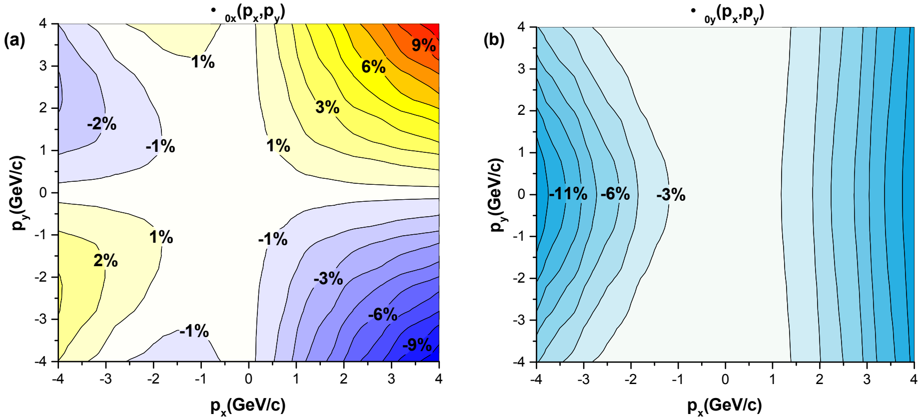

Figure 3.4: (color online) The (a) radial, x, and (b) axial, y, components of Λ-polarization, $\boldsymbol{\Pi}_0(\boldsymbol{p})$, in the Λ's rest frame. For $\Pi_{0x}(\boldsymbol{p})$ the contours represent changes of 1% from -9.5% in the upper left-hand corner to 9.5% in the upper right-hand corner, whereas the contours of $\Pi_{0y}(\boldsymbol{p})$ change in steps of 2% ranging from $\Pi_{0y} = 0$ (!) at the CM momentum ($p_x = p_y = 0$) to -12% for $p_x = \pm 4\text{GeV/c}$ at the edges. Both plots are asymmetric due to the Lorentz boost to the Λ rest frame.

Recently the vorticity and polarization were also studied in two fluid dynamical models [21]. The initial states that were used from Bozek and Gubser neglected fully the initial shear flow in the central domain of the reaction, in contrast to other models where this is present [3, 22–24]. This results in negligible thermal vorticity in the central domain of the collision (Figs. 3, 13 of Ref. [21]), and consequently a negligible polarization from the vorticity from the "first term" discussed here. Thus, the observed vorticity arises from the "second term".

On the other hand there is qualitative agreement between Figs. 12 of Ref. [21] and this work in the sense that only the y-directed (i.e. [x,z] or [x,η]) component of the vorticity leads to an overall average net polarization. This arises in both models from the initial angular momentum and points into the $-y$-direction. In Ref. [21] this arises as a consequence of viscous evolution of the initial, vorticity-less flow, while in our Exact model it is present in the initial state.

Recent preliminary experimental results reported for the first time [25], significant Λ and $\bar{\Lambda}$ polarization for peripheral collisions at RHIC for beam energies $\sqrt{s_{NN}} = 7.7 - 39$ GeV aligned with the axis direction of angular momentum of the participant system. Furthermore, the Λ and $\bar{\Lambda}$ polarizations were pointing in the same direction confirming our approach.

In this work we analyzed and compared the two terms of polarization, in the Exact model. Including both rotation, expansion, and vorticity arising from both of these effects enables us to study the consequences of the two terms separately. This study indicates that the assumptions regarding the initial state are influencing the predictions on the observed vorticity, while in all cases observable polarization is predicted.

Chapter 4

Global Λ polarization for intermediate energy

In previous chapter, we have developed a non-relativistic analytic solution of Λ polarization for an Exact rotating model. We found that the second term in polarization 4-vector is not negligible, but has a considerable contribution to the polarization, especially at the later stage of the hydrodynamic evolution, where the longitudinal rotation slows down and intensive transverse expansion starts.

In this chapter, we calculate the Λ polarization based on the 3+1-dimensional Particle-in-Cell Relativistic (PICR) hydrodynamics model, which is introduced in the Section 2.2.

4.1 Polarization effect: from experiments to theory

The nontrivial polarization effect in high energy collisions, since it was firstly observed in Fermilab with both polarized and unpolarized incident beam [26, 27], had been raising people's interest. The Λ hyperon is well suited to measure the polarization because through the decay $\Lambda^0 \to p + \pi^-$ with proton carrying the spin information, the Λ becomes its own spin-analyzer. Afterwards, more experimental research had been launched continuously, including nucleon collisions and heavy ion collisions [28–34]. Theoretical studies have also been underway synchronously with the experiments [15, 19, 21, 35, 37–

41, 52].

These experiments had observed that, 1) the Λ polarization is perpendicular to the reaction plane, 2) and increases with the Λ's transverse momentum (p_T) and its Feynman-x, taken to be $x_F = p_L/\sqrt{s}$ [29, 30, 32]. However, no significant evidence was found to indicate the energy dependence of the hyperon polarization, which we will discuss in this paper.

The Λ polarization in experiments was measured through the angular distribution of emitted protons in Λ's rest frame:

$$\frac{dN}{dcos\theta} = (1 + \alpha P cos\theta)/4\pi, \tag{4.1}$$

where θ is the angle between the proton momenta $\boldsymbol{p}_p$ and the Λ's spin $\boldsymbol{S}_\Lambda$, P is the polarization amplitude, and the decay parameter α is taken to be 0.647 ± 0.013 [26, 33]. To perform the measurement and calculation, it is crucial to determine the Reaction Plane (RP) and Center of Mass (CM) of the participant system. Recently it was pointed out that in collider experiments the CM frame determination might not be accurate enough due to the nuclear fragmentation effects while the early fixed target experiments can get rid of this issue [42].

From the experiments, theorist suggested that the hyperon polarization originates from the initial substantial angular momentum, $\boldsymbol{L}$, in non central collisions, since the global polarization aligns with the orbital angular momentum. The initial angular momentum is dependent on impact parameter, or centrality percentage, taking a shape of quadratic function that peaks around 9% centrality percentage, as shown in Refs. [43, 44]. In the RHIC's Au+Au collisions at 62.4 GeV and 200 GeV, no centrality dependence of the global hyperon polarization was analyzed [45], due to the insignificant polarization. Recently, stronger polarization signal was observed in RHIC's Beam Energy Scan (BES) program in the energy region below 100 GeV [46]. Therefore, in this thesis we will try to explore this issue again.

During the past decades, two different perspectives were developed for the transition mechanism from initial angular momentum to the final state hyperon polarization, i.e. the hydrodynamic perspective and partonic kinetic perspective. From the partonic micro-perspective, the initial angular momentum is transferred to the partons through the interaction of spin-orbit coupling in viscous QGP [52], and then the global polarized quarks are recombined into hadrons, in which the Thomas precession of the quark spin was applied [47].

In the hydro- and thermo- dynamical description, the initial angular momentum is manifested in a longitudinal velocity shear, which, with small shear viscosity, results into a rotating system with substantial vorticity and even Kelvin-Helmholtz instability [48]. Assuming local equilibrium at freeze out and equipartition of the spin degree of freedom, Ref. [15] put forward a polarization 3-vector for spin 1/2 particles and antiparticles based on the generalization of Cooper-Frye formula for particles with spin.

It was recently pointed out that the detailed balance of Cooper-Frye formula on Freeze-Out(FO) hypersurface requires a non-vanishing polarization in fluid before FO [49]. However, the absence of pre-FO polarization should not significantly effect the polarization calculation based on Ref. [15]. One can calculate that, the spin of each baryon is $L = \hbar/2 \approx 98.5\, MeV\cdot fm/c$. As the polarization is between 1 - 10 % at different beam energies in the RHIC BES program, this gives $L \approx 1 - 10\, MeV\cdot fm/c$ for the angular momentum carried by one baryon. On the other hand the total angular momentum is around [14]: $L = 1.05 \times 10^4 \hbar = 205.8 \times 10^4\, MeV\cdot fm/c$. This is distributed among a few hundred baryons in semi-peripheral reactions at not too high energies, i.e. very few antibaryons, which gives an angular momentum per baryon: $L \approx 10^4\, MeV\cdot fm/c$. This is 3 - 4 orders of magnitude bigger than the spin angular momentum carried by one baryon in the vortical flow. Therefore, even if 1 - 10% of spins are already polarized before FO, carrying only one per mil of the total angular momentum, they will neither effectively impact the fluid dynamical evolution, nor significantly change the detailed balance during FO process, thus keeping the validity of the polarization 3-vector, i.e.

Eqs. (3.11,3.12).

4.2 Initial state and hydrodynamic model

In Ref. [50] the flow vorticity was evaluated and reported . Based on these results we report the Λ polarization results for the same reactions. The initial state Yang-Mills flux-tube model [3] describes the development from the initial touching moment up to 2.5 fm/c. Then the PICR Hydro code is calculated for another 4.75 fm/c, so that the final freeze out time is 7.25 fm/c.

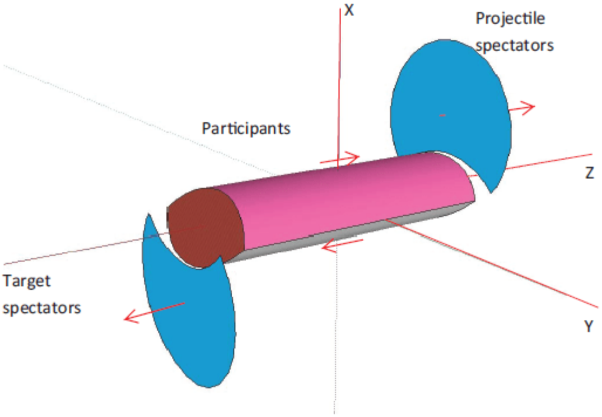

Figure 4.1: The three-dimensional view of the collisions shortly after the impact. The projectile spectators are going along the z direction; and the target spectators are going along the z axis.The collision region is assumed to be a cylinder with an almond-shaped profile and tilted end surfaces, where the top side is moving to the right and the bottom is moving to the left. The participant cylinder can be divided into streaks, and each streak has its own velocity, as shown in Fig. 2(a). The velocity differences among the streaks result in rotation, turbulence and even KHI.

The fluid dynamical calculation and the initial state model used here, has been tested in several model calculations in the last decade. It describes correctly the initial shear flow characteristics. The angular momentum distribution is based on the assumption that the initial angular momentum of the participants (based on straight propagation geometry) is streak by streak conserved, thus the model satisfies angular momentum conservation both locally and globally. Fig.4.1 shows the 3-dimensional view of the simulated collisions shortly after the impact, and it could naturally generate a longitudinal velocity shear along the x direction, as shown in Fig. 4.2(a). This type of longitudinal velocity shear is a requirement for the subsequent rotation, turbulence and even Kelvin Helmholtz instability (KHI), just as discussed in our previous paper [51], as well as in refs. [52, 53]. The vortical flow formed in the equilibrated hydro evolution, as shown in Figs. 4.2(b)(c)(d), can give rise to the polarization due to the equipartion principle or spin-orbit coupling.

Both in the initial state and subsequent CFD simulation, the frequently used 'Bag Model' EoS was applied: $P = c_0^2 e^2 - \frac{4}{3}B$, with constant $c_0^2 = \frac{1}{3}$ and a fixed Bag constant B [1, 3]. The energy density takes the form: $e = \alpha T^4 + \beta T^2 + \gamma + B$, where α, β, γ are constants arising from the degeneracy factors for (anti-)quarks and gluons.

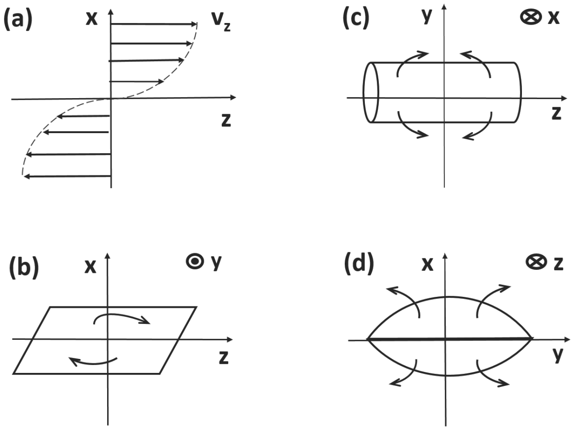

Figure 4.2: The schematic hydro flow velocity after the collisions shown in Fig. 1. Panel (a) is the longitudinal velocity profile along the x direction, and it gives rise to the v_1 type of flow in the reaction plane, i.e. Panel (b). Panel (c) is the anti-v_2 type of flow in the [y-z] plane, and Panel (d) is the v_2 type of flow in the [x-y] plane.

4.3 Freeze out Stage

The fluid dynamical model is in principle not adequate to describe the final, post freeze-out (FO) particle distributions, the abundance of the particle species and also their polarization. This is so because the post freeze-out distributions must not be in local thermal equilibrium and must not have interactions among the final emitted particles. Furthermore, the emitted particles should not move back into the interacting zone, i.e. towards the pre-FO side of the FO hypersurface. How to handle the freeze-out is described in great detail in [54]. It indicates two ways to handle this process: (i) consider the post-FO matter as if it has an Equation of State (EoS). This is only possible if the post FO EoS is that of a non-interacting ideal gas and the FO hypersurface is timelike. (ii) The other approach is that the post FO matter is described by a dynamical model with weak and rapidly decreasing interaction, like UrQMD or PACIAE models, matched to the QGP fluid on the FO hypersurface. The change at crossing this hypersurface is in general significant, as the pre-FO matter is strongly interacting, supercooled QGP, while the post-FO matter is weakly interacting and has different (usually less) degrees of freedom in both situations. The FO change across the hypersurface is stronger if the latent heat of the transition is larger.

The precise way to perform this transition is described in [54]. This method is demonstrated in several earlier fluid dynamical model calculations (also using the PICR method), for precision calculations of flow harmonics.

As mentioned in the introduction, at high energies (RHIC and LHC) the Constituent Quark Number Scaling and the large strangeness abundance clearly indicate a supercooling and rapid hadronization. Furthermore, at these energies the transition is in the crossover domain of the EoS, thus the expected changes are smaller, and the major part of the FO hypersurface is time-like, which allows to use ideal gas post FO distributions, as we do it here using the method of [15]. These are the conditions which make the changes in mechanical parameters (e.g. $\boldsymbol{v}$) small at freeze-out while the temperature changes are larger [54].

Thus, just in the case of Constituent Quark Number Scaling, we assume that other mechanical processes like mechanical polarization will not significantly change at freeze-out at RHIC and LHC energies. This conclusion is restricted to local thermal and flow equilibrium, and should not apply to some of the microscopic processes, which dominate $p + p$ reactions.

Also, in case of freeze-out through space-like FO hypersurfaces, the mechanical parameters change significantly, the post-FO distribution is far from a thermal distribution (it is a Cut-Juttner of Canceling Juttner distribution), and thus the conditions of [15] that we use, are not satisfied.

4.4 Λ Polarization for NICA and FAIR

Different from Chapter 3, in this chapter we numerically solve the polarization 3-vector, i.e. the Eq. (4.2):

$$\mathbf{\Pi}(p) = \frac{\hbar\epsilon}{8m} \frac{\int dV n_F(x,p)\,(\nabla \times \boldsymbol{\beta})}{\int dV n_F(x,p)} + \frac{\hbar \boldsymbol{p}}{8m} \times \frac{\int dV n_F(x,p)\,(\partial_t \boldsymbol{\beta} + \nabla \beta^0)}{\int dV n_F(x,p)} \ .$$

Here the *first term* is the classical vorticity term, while the *second term* is the relativistic modification. The above convention of $\mathbf{\Pi}(p)$ [15] is normalized to max. 50%, while in the experimental evaluation it is 100 %, thus we present the values of $2\mathbf{\Pi}(p)$ [55], unlike in earlier calculations [19, 21, 40].

In Fig. 4.3 the dominant y component of the polarization vector $\mathbf{\Pi}(p)$, for the first and second terms are shown. The first term is pointing into the negative y direction with a maximum of -26%. The structure of first term arises from the v_1 type of flow in Fig. 4.2(b), which is also unipolar and negative y directed. The second term has different structure, it points in the opposite direction and has a maximum of +22%, i.e./ $\sim$ 4% less than the absolute value of the first term.

In Fig. 4.4 the x component of the polarization vector $\mathbf{\Pi}(p)$, for the first and second

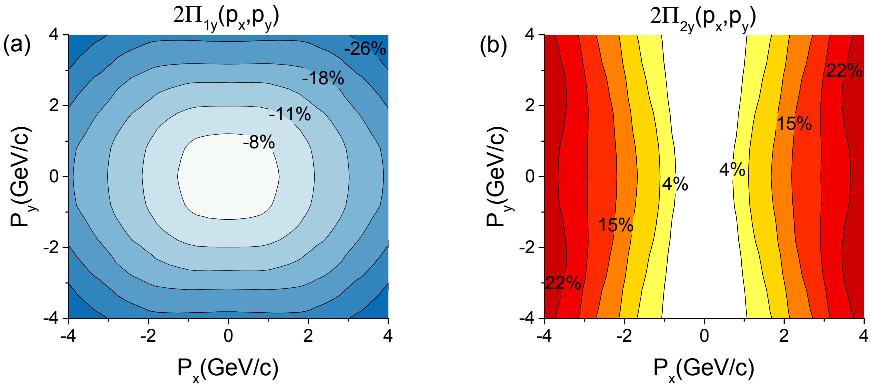

Figure 4.3: The first (left) and second (right) term of the dominant y component of the Λ polarization for momentum vectors in the transverse, $[p_x, p_y]$, plane at $p_z = 0$, for the FAIR U+U reaction at $\sqrt{s_{NN}} = 8.0$ GeV.

terms are shown. The first term is about four times smaller than the y component, $\pm 6\%$, and the positive and negative values are symmetric in a way that the integrated value of the polarization over the momentum space in the transverse plane is vanishing. This sign distribution is just the manifestation of anti-v_2 type of flow in [y-z] plane, seen in Fig. 4.2(c) with a dipole structure. The second term is about half of the y component, $\pm 17\%$, and the positive and negative values are symmetric in a way that the integrated value of the polarization over the momentum space in the transverse plane is vanishing. Furthermore the first and second terms have opposite signs at the same momentum values in the transverse plane, which decreases further their effect.

In Fig. 4.5 the z component of the polarization vector $\mathbf{\Pi}(p)$, for the first and second terms are shown. The first term has a maximum of $\pm 2\%$, and the positive and negative values are symmetric in a way that the integrated value of the polarization over the momentum space in the transverse plane is vanishing. This sign distribution is also the manifestation of the anti-v_2 type of flow in [x-y] plane, i.e. a dipole structure in Fig. 4.2(d). The second term has similar structure to the first one, with a maximum of $\pm 2\%$ also, but the first and second terms have similar structure in the momentum space.

In Fig. 4.6 the dominant y component of the polarization vector $\mathbf{\Pi}(p)$, for the sum of

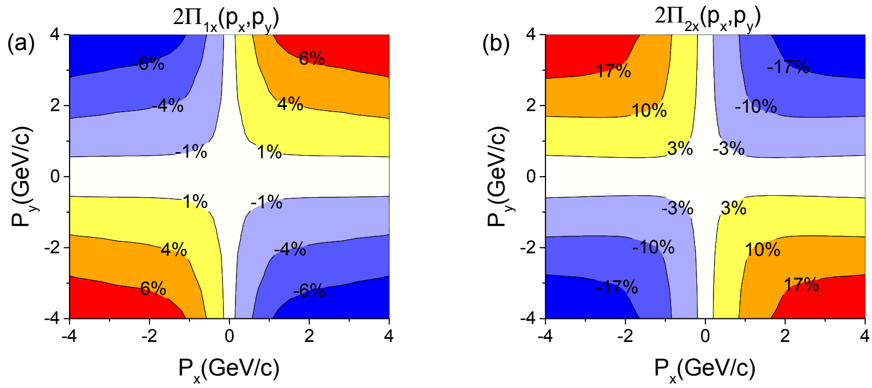

Figure 4.4: The first (left) and second (right) term of the x component of the Λ polarization for momentum vectors in the transverse, $[p_x, p_y]$, plane at $p_z = 0$, for the FAIR U+U reaction at $\sqrt{s_{NN}} = 8.0$ GeV.

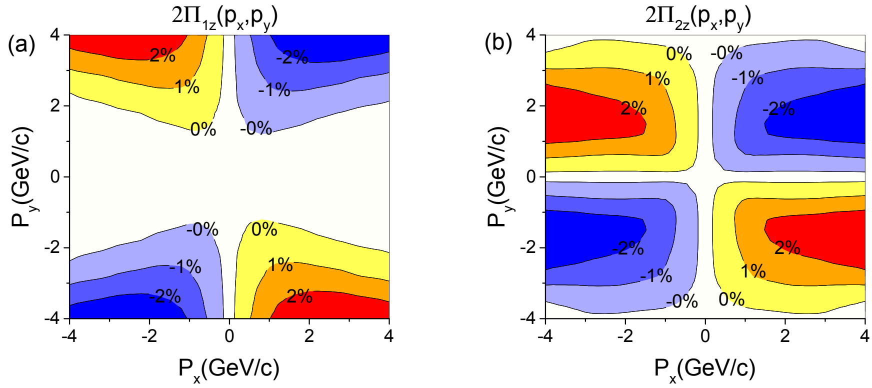

Figure 4.5: The first (left) and second (right) term of the z component of the Λ polarization for momentum vectors in the transverse, $[p_x, p_y]$, plane at $p_z = 0$, for the FAIR U+U reaction at $\sqrt{s_{NN}} = 8.0$ GeV.

the first and second terms is shown. The top figure is the distribution of the polarization in the center-of-mass frame while the bottom figure is in the local rest frame of the Λ.

Fig. 4.7 shows the modulus of the polarization vector $\mathbf{\Pi}(p)$. The maximum at high $|p_y|$ and low $|p_x|$ is the same as the absolute value of the Π_{0y} component. Here the other components have only minor contributions to the final observed polarization. At the corners, at high $|p_y|$ and high $|p_x|$, the contribution of the x and z components of $\mathbf{\Pi}(p)$ dominates, while the y component has a minimum.

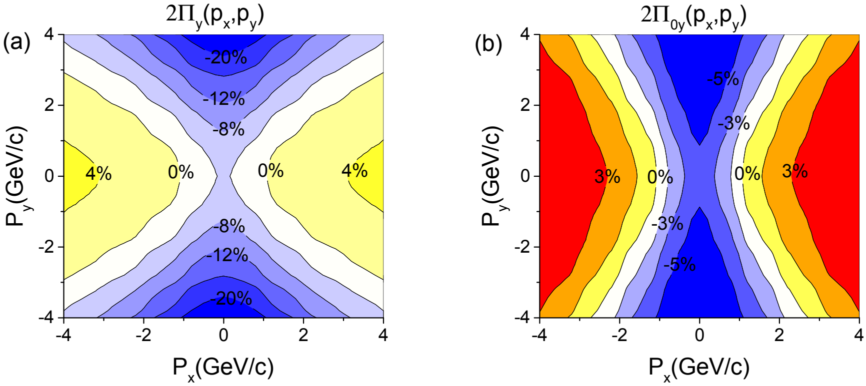

Figure 4.6: The y component of the Λ polarization for momentum vectors in the transverse, $[p_x, p_y]$, plane at $p_z = 0$, for the FAIR U+U reaction at $\sqrt{s_{NN}} = 8.0$ GeV. The top figure is in the calculation frame, while the bottom figure is boosted to the frame of the Λ [19].

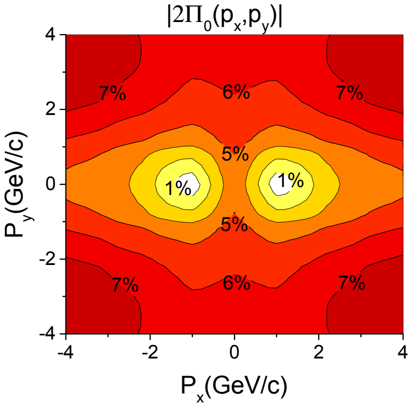

Figure 4.7: The modulus of the Λ polarization for momentum vectors in the transverse, $[p_x, p_y]$, plane at $p_z = 0$, for the FAIR U+U reaction at $\sqrt{s_{NN}} = 8.0$ GeV. The figure is in the frame of the Λ.

Fig. 4.8 shows the y component and the modulus of the polarization vector $\mathbf{\Pi}(p)$ for the NICA Au+Au reaction at $\sqrt{s_{NN}} = 9.3$ GeV. The structure and magnitude of the polarization is similar to the reactions at FAIR. The negative maximum at high $|p_y|$ and low $|p_x|$ arises from the classical vorticity in the y component. The positive maximum at high $|p_x|$ and low $|p_y|$ arises from the relativistic modifications of the second term. The momentum space average is dominated by the first term.

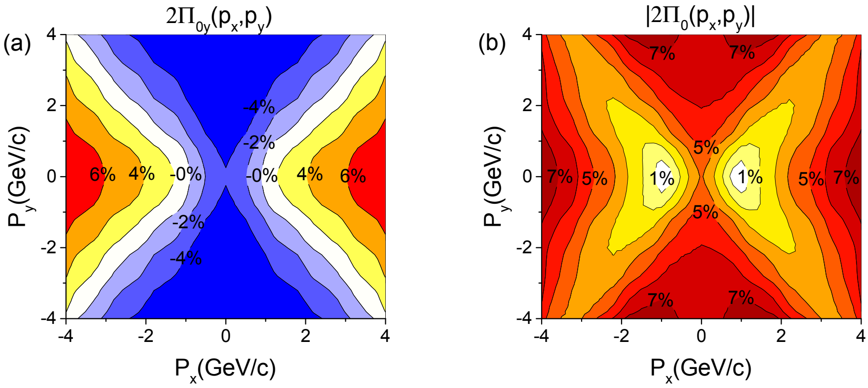

Figure 4.8: The y component (left) and the modulus (right) of the Λ polarization for momentum vectors in the transverse, $[p_x, p_y]$, plane at $p_z = 0$, for the NICA Au+Au reaction at $\sqrt{s_{NN}} = 9.3$ GeV. The figure is in the frame of the Λ.

The polarization studies at ultra-relativistic, RHIC and LHC energies, turned out to be sensitive to both the classical vorticity of the flow (first term) and the relativistic modifications arising from rapid expansion expansion at later stages of the flow (second term) [19, 55].

Initially the contribution of the classical vorticity is stronger than the relativistic modification term, i.e. the 'second' term. This is in line with earlier observations [50, 56]. The effect of this decrease is also visible in the polarization results. The Λ polarization was evaluated at earlier freeze out time, $t = 2.5 + 1.7\text{fm/c} = 4.2\text{fm/c}$ for the FAIR U+U reaction. See Fig. 4.9

The y component and the modulus of the polarization vector $\mathbf{\Pi}(p)$ have very similar structure and magnitude, although the y component points in the negative y direction as the angular momentum vector from the initial shear flow. This indicates that the other, x and z, components are of the order of 1% only at moderate momenta where the y component and the modulus are of the order of 5-6%. At the "corners", at high $|p_y|$ and high $|p_x|$, the contribution of the x and z components of $\mathbf{\Pi}(p)$ are approaching that of the y component, so that the modulus is larger than the y component, by 4-5%. Still the contribution of these second term components is clearly smaller than the classical

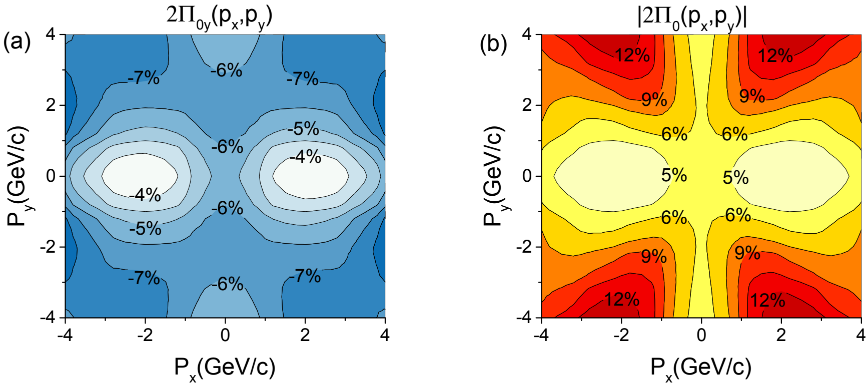

Figure 4.9: The y component (left) and the modulus (right) of the Λ polarization for momentum vectors in the transverse, $[p_x, p_y]$, plane at $p_z = 0$, for the FAIR U+U reaction at $\sqrt{s_{NN}} = 8$ GeV at the earlier freeze out time of $t = 4.2$ fm/c. The figure is in the frame of the Λ.

vorticity component.

It is important to mention the role of the initial condition. The *second term*, the relativistic modification, develops during the expansion of the system and is not very sensitive to the initial state. This is shown by the fact that the structure of the x component of polarization, Π_{2x} in the dominant Fig. 4.4b, is very similar to Fig. 14b of ref. [21]. At the same time here the initial shear and classical vorticity are present in the initial state with strong stopping and dominance of the Yang-Mills field, [3, 57], while in ref. [21] this is not present. As a consequence the final polarization estimates in the y direction are different in the two models.

4.5 Centrality and energy dependence, time evolution

As we pointed out in our previous discussion, the x and y components of polarization, $2\Pi_x$ and $2\Pi_x$, in transverse momentum space $[p_x, p_y]$ are rather trivial and form a symmetric dipole structure, which results in vanishing global polarization along the x and y direction in the participant CM frame. Meanwhile, as expected, the $-y$ directed polarization, aligned with the initial angular momentum, dominates the modulus of polarization 3-

vector, $2|\boldsymbol{\Pi_0(p_x, p_y)}|$. Fig. 1 in Ref. [58] shows the dominant y component and the modulus of Λ polarization, in Au-Au collisions at 11.5 GeV. One can see that the top and down figures have similar structure and magnitude, which indicates a trivial influence of the x and y components on the global polarization.

Since the $-y$ directed global Λ polarization in experimental results is averaged polarization over the Λ's momentum space, we evaluated the average of the y component of the polarization $\langle \Pi_{0y} \rangle_p$. We integrated the y component of the obtained polarization, Π_{0y}, over the momentum space as follows:

$$\begin{aligned} \langle \Pi_{0y} \rangle_p &= \frac{\int dp\, dx\, \Pi_{0y}(p,x)\, n_F(x,p)}{\int dp\, dx\, n_F(x,p)} \\ &= \frac{\int \ dp\, \Pi_{0y}(p)\, n_F(p)}{\int \ dp\, n_F(p)} \end{aligned} \tag{4.2}$$

to calculate the global polarization. The word 'global' means averaging over phase space $[\boldsymbol{x},\ \boldsymbol{p}]$. Besides, we replace the $\langle \Pi_{0y} \rangle_p$ with $-\langle \Pi_{0y} \rangle_p$, since in experiments the angular momentum's direction, i.e. negative y direction is the conventional direction for global polarization.

4.5.1 Angular momentum, Impact Parameter and Centrality

According to the alignment of polarization and the system's angular momentum, theorists suggested to attribute the polarization to the initial orbital angular momentum arising in non-central collisions. Refs. [43, 44] have analytically deduced and schematically displayed the initial angular momentum in the reaction region as a function of impact parameter b, taking the form of quadratic function, which roughly peaks at $b = 0.25b_m$ or $0.3b_m$. If the angular momentum is translated into polarization without any other significant perturbative mechanism, one should also observe the polarization's dependence on impact parameter. In other words, the initial angular momentum of the participant system is initiated by the inequality of local nuclear density in the transverse plane, and this inequality is dependent on the impact parameter. Thus, the initial impact parameter dependence of the late-state polarization should in principle be observed.

Fig. 4.10 shows the global polarization of Au+Au collisions as a function of ratio of impact parameter b to Au's nuclear radius R, i.e. $b_0 = b/2R$. One could see that the polarization at different energies indeed approximately takes a linear increase with the increase of impact parameter, except for 62.4GeV due to the vanishing polarization signals at relatively central collisions. This linear dependence clearly indicates that the polarization in our model arises from the initial angular momentum. However, the polarization's linear dependence on b is somewhat different from the angular momentum's quadratic dependence on b. This is because the angular momentum L is an extensive quantity dependent on the system's mass, while the polarization Π is an intensive quantity.

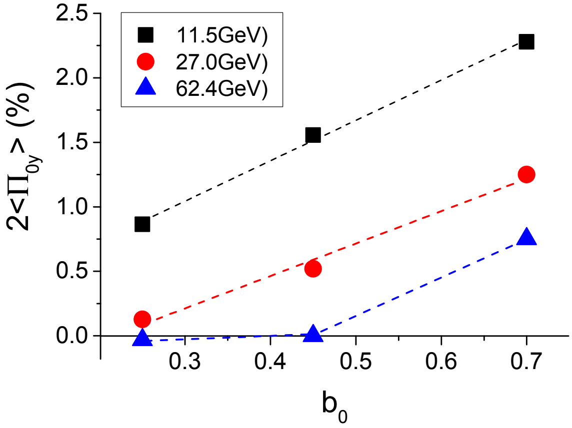

Figure 4.10: The linear dependence of global polarization, $2\langle\Pi_{0y}\rangle_p$, as a function of impact parameter ratio b_0 at 11.5 GeV, 27.0 Gev and 62.4 GeV.

An earlier Λ global polarization measurement by STAR in Au+Au collisions at 62.4 GeV and 200 GeV, had observed a not significant indication of centrality dependence, due to the occurrence of negative polarization, as well as large error bars [34, 59]. The result of opposite directed global polarization at different centralities would be weird, if we assume that polarization comes from the angular momentum. Besides, no experimental Λ polarization measurements, previous to the present ones had observed the opposite pointing direction of global Λ polarization [26–31]. This might be because of the inappropriate choice of momentum space. However, from the Figs. 5 and 7 in Ref. [34, 59] one could still see that, the polarization signal becomes stronger at larger centrality, while at small centrality percentage (below 40%) the signal is weak and vanishing. Similar behavior occurs in our simulation results for 62.4 GeV, specifically the polarization value also vanishes when the centrality percentage goes below 20%, and increases as the centrality increases.

The recently reported global Λ polarization observation in STAR's BES I program has shown a positive signal for both Λ and $\bar{\Lambda}$, thus it is promising to eliminate the disturbing opposite polarization direction that occurred in previous experiments [26–31], and this confirms our predictions. Besides, the RHIC's Event Plane Detector (EPD) on upgrading for future BES II with higher EP resolution, will provide a better chance to determine the issue of centrality dependence of Λ polarization [60]. With experimental CM identification one could also verify the momentum dependence of the polarization as shown in Fig. 1 of Ref. [58].

4.5.2 Energy Dependence and Time evolution

The increases of Λ polarization with its Feynman-$x_F = p_L/\sqrt{s}$, as well as transverse momentum p_T, had been observed in experiments and can be partly attributed to the $s\bar{s}$ pair production mechanism. It was also predicted that the polarization should also depend on the collision energy $\sqrt{s}$, although early experiments did not find evident signals to confirm this [29, 30, 32]. Recently with an exploration at low energy domain between 7.7 GeV to 27.0 GeV, the RHIC BES I program had successfully observed the energy dependence of Λ polarization with a higher EP resolution and better background extraction.

Using the PICR hydrodynamic model, we calculated the global Λ polarization at the following energies: 11.5 GeV, 14.5 GeV, 19.6 GeV, 27 GeV, 39 GeV, 62.4 GeV, and 200

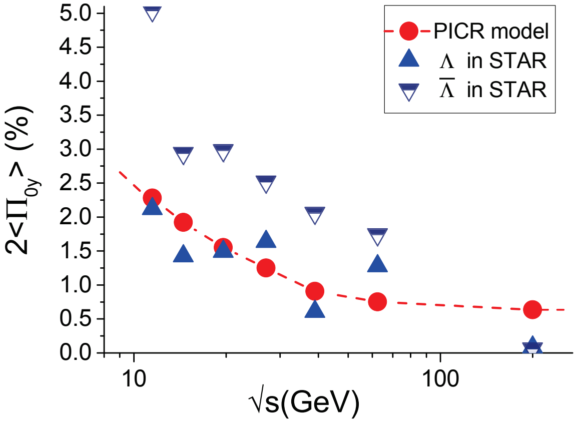

Figure 4.11: The global polarization, $2\langle\Pi_{0y}\rangle_p$, in our PICR hydro-model (red circle) and STAR BES experiments (blue triangle), at energies $\sqrt{s}$ of 11.5 GeV, 14.5 GeV, 19.6 GeV, 27.0 GeV, 39.0 GeV, 62.4 GeV, and 200 GeV. The experimental data were extracted from Ref. [46], with solid triangle for Λ and hollow triangle for $\bar{\Lambda}$, dropping the error bars.

GeV, and plotted them with red round symbols in Fig. 4.11. The impact parameter is $b_0 = 0.7$, i.e. the centrality percentage is $C = 49\%$. For comparison the data of Λ and $\bar{\Lambda}$ polarization from STAR (RHIC) were inserted into Fig. 4.11 with blue triangle symbols. One could see that our model fits fairly well the experimental data. Although the experimental $\bar{\Lambda}$ polarization is larger than the Λ polarization, it will not change the averaged polarization very much, because the production ratio of $\bar{\Lambda}$ to Λ is very small in high energy collisions [61].

Fig. 4.11 clearly shows that Λ polarization is dependent on collision energy; it drops very fast with increasing energy from 11.4 GeV to 62.4 GeV, and tends to saturate after 62.4 GeV. From thermodynamical perspective, the polarization decreases with energy, and this can be attributed to the higher temperature in higher energy collisions. The drastic thermal motion of particles will decrease the quark polarization rate, which according to Ref. [52] is inversely proportional to the collision energy. One the other hand, simulating results by AMPT has shown that the averaged classical vorticity decreases with the collision energy [56, 62], thus of course leads to the decline of global Λ po-

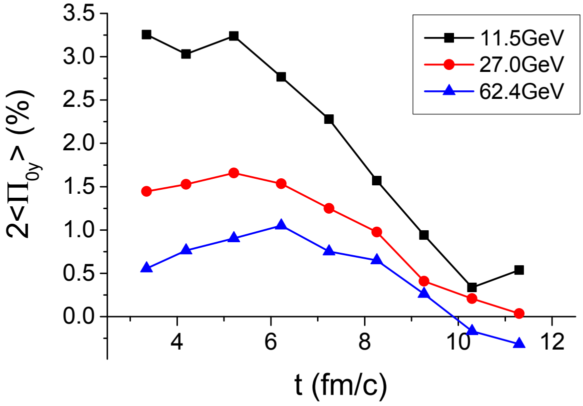

Figure 4.12: The calculated time evolution of global polarization, $2\langle\Pi_{0y}\rangle_p$, for energy $\sqrt{s}$= 11.5 GeV, 27 GeV and 62.4 GeV.

larization. The higher polarization of $\bar{\Lambda}$s can most probably attributed to the stronger spin-orbit coupling between $\bar{\Lambda}$s and normal nuclear matter than the coupling between Λs and normal nuclear matter.

It is also interesting to take a glance on the time evolution of Λ polarization, shown in Fig. 4.12. In this figure, the Λ polarization increases slowly at early stage, then falls down very fast. The negative polarization values that occur at 62.4 GeV after 10 fm/c, demonstrate the loss of validity of the hydrodynamic model at late stages of system expansion, due to the large surface to volume ratio. Besides, at early stages, no Λs are produced, so the climbing segment of the curves before 4 fm/c is not observable.

4.6 Summary and Conclusion

With a Yang-Mills field initial state and high resolution (3+1)D Particle-in-Cell Relativistic (PICR) hydrodynamics simulation, we calculate the Λ polarization for intermediate energies , i.e. NICA and FAIR energies (Section 4.4), and for different energies, different impact parameters (Section 4.5). We found that:

1), y-directed component of Λ polarization is dominant, aligning with the initial angular momentum;

2), the x and z components are trivial and form a symmetric dipole structure in transverse momentum space $[p_x, p_y]$;

3), we plotted the global polarization as a function of impact parameter b and a linear dependence on b was observed;

4), the global Λ polarization in our model decreases very fast in low energy domain, and the decline curve fits very well with the recent experimental results of Beam Energy Scan (BES) program launched by STAR (RHIC). This is a very exciting new founding, which indicates the significance of thermal vorticity and system expansion;

5), the time evolution of Λ polarization shows the limitation of hydrodynamic model at later stages of system expansion.

It is worth to mention a little about the determination of Event Plane (EP) in experimental. For the correct determination of the momentum space dependence of Λ polarization, we have to know the reaction plane and the Center of Mass (CM) of the participant system in a peripheral heavy ion reaction. The Event by Event (EbE) determination of the longitudinal CM of participants could be measured by the forward backward asymmetry of the particles in the Zero Degree Calorimeters (ZDCs). In colliders only single neutrons are measured in the ZDCs, so one has to extrapolate from these to the total spectator momenta. This method to detect the EbE CM was proposed in Refs. [42, 63].

At collider experiments, e.g. the LHC-ALICE or RHIC-STAR, this determination was not performed up to now, with the argument [64] that nuclear multi-fragmentation may also lead to fluctuation of single neutron hits in ZDCs, and therefore CM frame would have been determined inaccurately. However, at FAIR's fixed target experiments, it is possible to detect all the fragments from multi-fragmentation of spectators, thus the CM frame can be determined accurately.

Since the experimental measurement of global Λ polarization is conducted around different azimuthal angle, it is crucial to accurately define the EbE CM frame. In symmetric collider experiments, the CM frame de facto fluctuates around the actual CM frame. The fixed target FAIR setup can get rid of this uncertainty perfectly. The Compressed Byronic Matter (CBM) experiments will be able to measure the polarization effects at SIS-100 and SIS-300 with millions times higher intensity and event rate, up to six order of magnitude than at the RHIC Beam Energy Scan program.

The higher multiplicity, thus allows for the high resolution measurement of the momentum space dependence of the Λ polarization, which can be decisive to determine the dominant polarization mechanism.

Therefore, we hope that after upgrading the Event Plane Detector, the STAR will provide a higher resolution EP determination and centrality, to determine precisely the centrality dependence of global Λ polarization.

Chapter 5

Inital state with shear

We have discussed in Section 4.2 about the Initial State (IS) model used in this thesis. It is characterized by the substantial initial angular momentum based on streak-by-streak energy-momentum conservation, and the shear flow that can lead to rotation and turbulence in hydrodynamic simulation with numerical viscosity. This model was firstly developed by Ref. [3] about 16 years ago. Recently the Λ polarization measured in RHIC BES program has indicated the shear and vorticity should not be neglected. On the other hand several parton kinetic and field theoretical models implemented recently show a different initial state configuration, e.g. an IS of Figure 5.1 from AMPT model. While in our early model the off-center streaks were assumed to have relatively weak fields and therefore showed large longitudinal extent, the kinetic models in Fig. 5.1 show a more compact IS, where the streaks away from the center are more compact and experience stronger fields.

To reflect these progresses, we want to revisit the early IS model, to adapt to the new developments in experiments and theoretical simulation [65–67], while keeping all basic features such as local shear, angular momentum conservation and local vorticity. Furthermore, as several field theoretical models are developed recently in the proper-time and space-time rapidity, $[\tau, x, y, \eta]$, coordinates, we will present the model in the same way to make it useful for other approaches. On the other hand we will continue

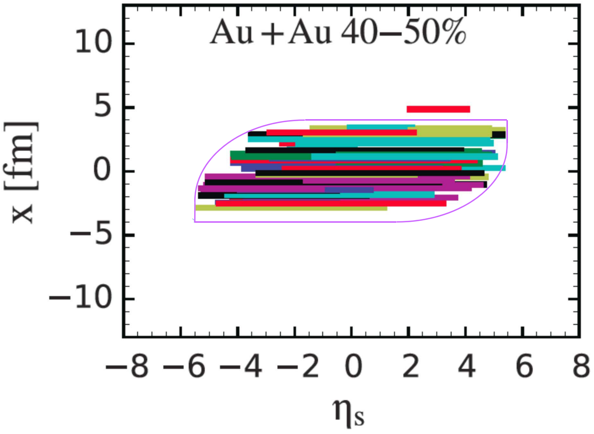

Figure 5.1: (color online) Initial State streaks indicate the energy density distribution with fluctuating initial conditions from A Multi-Phase Transport (AMPT) model, ref. [12]. The model simulates a Au+Au collisions at the energy $\sqrt{s_{NN}} = 200$GeV of centrality percentage 40-50% in the reaction plane in $[x, \eta_s]$ coordinates. The energy density distribution remains compact and the off-center side streaks are actually shorter than the central streaks. At the same time the off-center side streaks have obviously moved forward and backward indicating angular momentum conservation and significant local shear. The inserted thin magenta line surrounding the matter distribution shows the characteristic shape of the initial state obtained in the AMPT model.

to use fluid dynamical models in Cartesian coordinates, $[t, x, y, z]$, as e.g. the Particles in Cell Relativistic model (PICR), since in these codes the numerical effects are under control, while in coordinates with size-changing and anisotropic computational cells the consequences of numerical viscosity and super-luminal effects are problematic.

5.1 Configuration and Milne Coordinate

Let us consider a peripheral heavy ion collision at highly relativistic energies. The projectile and target are strongly Lorentz contracted before the collision, while the parton momentum distributions of the projectile and target are at the same time strongly Lorentz elongated.

We divide up the transverse plane into cells of about 1 fm^2 size. These surface elements of the projectile and target hit and inter-penetrate each other. After a time of one or two fm/c, the partons of the projectile and target in this surface element form a streak from the pre collisions projectile and target slabs, which is about two to four fm long. Due to the large momentum spread of the initial partons the original slabs will have a mixture of projectile and target partons at each point of the slab. In peripheral collisions in a given slab, there will be a projectile/target asymmetry (except at the exact center of the transverse plane). Thus, the final streaks will have a finite longitudinal momentum, due to the longitudinal momentum conservation from the two original slabs. Streaks on the projectile side of the transverse plane ($x > 0$) will have a forward momentum, while on the target side ($x < 0$) a backward one. Thus, each streak will have its own center-of-mass (c.m.) reference system and among these streaks there will be an initial shear. This compact system will have at this time ($\sim 1-2$ fm/c) an angular momentum. Its partons will be mixed from the projectile and target. The chromo-magnetic forces (string tension) will attract the leading partons. So, the system will not expand with the speed of light but will be held back by the fields. The original Lorentz elongation of the momentum distribution and the field attraction will lead to an initial parton distribution, which will be close to uniform, as both the target and projectile partons can populate the whole length of the moving slab [66].

From the initial geometry we know the c.m. momentum of each streak at each transverse, $[x, y]$ point. We assume that at $t =$2 fm/c all streaks are within the $z \in \pm 2$ fm boundaries. The slabs are moving with their c.m. velocities, and the ends of the slabs are expanding longitudinally (z) in their own reference frame. This would be similar to the well known yo-yo motion of a color string. The motion of the ends of the streaks could be described (streak by streak separately) with the trajectories as shown in refs. [3, 68, 69].

For a streak i, at a transverse plane point, x_i, z_i, which **in its own reference frame**, at the streak ends, $z_i = \pm 2$ fm, expands, and we will assume that the slab has a rapidity profile as in the Bjorken flow expansion. Then, for each such slab we can construct a fictitious starting point at some τ_0 proper time earlier.

Let us have two projectile and target slabs colliding head on with each other for a streak i at a given transverse point. These slabs have baryon charge, energy and momentum, N_1, E_1, P_{1z} and N_2, E_2, P_{2z}, respectively. The pre-collision projectile slab moves with the beam rapidity y_0 while the target slab with $-y_0$.

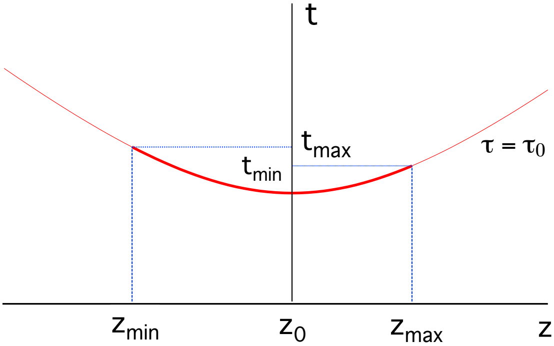

Figure 5.2: Space-time sketch of a slab-slab collision in the collider c.m. frame. At proper time τ_0 after the collision, the projectile slab stretches from t_{min}, z_{min} to $\tau_0, 0$, and the target slab from $\tau_0, 0$ to t_{max}, z_{max}.

In Fig. 5.2 the streak-streak collision happens at proper time τ_0 time after the initial time t_0 and the corresponding touching point at this time, z_0.

Let us determine these two parameters, from the others. The transformation between the usual Cartesian coordinates $x^\mu = (t, x, y, z)$ and Milne coordinates $\tilde{x}^\mu = (\tau, x, y, \eta)$ is given as

$$\begin{aligned} t - t_0 &= \tau \cosh \eta \ , \\ z - z_0 &= \tau \sinh \eta \ , \\ \tau &= \sqrt{(t-t_0)^2 - (z-z_0)^2} \ , \\ \eta &= \frac{1}{2} \ln \left(\frac{t - t_0 + z - z_0}{t - t_0 - (z - z_0)} \right) \\ &= \operatorname{artanh} \frac{z - z_0}{t - t_0} \ , \end{aligned} \tag{5.1}$$

where η is the space-time rapidity. Consequently, if $z_0 = 0$ and $t_0 = 0$ then

$$\begin{aligned} dt &= \cosh\eta\, d\tau + \tau \sinh\eta\, d\eta \\ dz &= \sinh\eta\, d\tau + \tau\cosh\eta\, d\eta \\ dz\, dt &= \tau d\eta d\tau. \end{aligned} \tag{5.2}$$

In case of the longitudinal Bjorken scaling flow, the local flow velocity of matter $u_i^\mu = x_i^\mu/\tau = (\cosh\eta, 0, 0\ \sinh\eta)$. Then the velocity of the Bjorken flow at point (t, z) is

$$\begin{aligned} v_z &= \frac{z - z_0}{t - t_0} && \text{and for the streak} - \text{ends} \\ v_{z-max} &= \frac{z_{max} - z_0}{t_{max} - t_0} && v_{z-min} = \frac{z_{min} - z_0}{t_{min} - t_0}\ , \end{aligned} \tag{5.3}$$

and the end points satisfy $\eta_{min} < \eta < \eta_{max}$, and $z_{max} = z_0 + \tau_0 \sinh\eta_{max}$, $z_{min} = z_0 + \tau_0 \sinh\eta_{min}$.

5.2 Conservation law

Conservation laws can be assessed across any time-like hypersurface, also across a $\tau =$ constant hypersurface. The hypersurface normal four vector is given as,

$$d^3\Sigma_\mu^{(t,z)} = \tau\,(\cosh\eta, 0, 0, -\sinh\eta)\, dxdyd\eta = \tau A u_\mu d\eta, \tag{5.4}$$

where A is the transverse cross section of the streak (in the $[x, y]$-plane).

The net baryon four current for a streak is $N^\mu = nu^\mu$, and thus the net baryon number crossing a constant τ- hypersurface element is

$$dN = d^3\Sigma_\mu N^\mu = n\tau A\, d\eta, \tag{5.5}$$

Thus, the baryon number conservation for a streak, assuming uniform η-distribution is:

$$N_i = N_1 + N_2 = \tau_0 n(\tau_0) A \left[\eta_{max} - \eta_{min}\right] \,, \tag{5.6}$$

where e is the energy density, $(N_1 + N_2)$ is an invariant scalar given by the Projectile (1) and Target (2) baryon charge contribution to a given streak, and the difference, $(\Delta\eta_i = \eta_{max} - \eta_{min})$, should also be boost invariant quantity.

In this section we drop the streak index i from the limiting rapidities, η_{max} and η_{min} for easier reading.

For the energy conservation the energy-momentum tensor is $T^{\mu\nu} = eu^\mu u^\nu - p\Delta^{\mu\nu} + \pi^{\mu\nu}$, where $\Delta^{\mu\nu} = g^{\mu\nu} - u^\mu u^\nu$ is the projection tensor and $\pi^{\mu\nu}$ is the shear-stress tensor, both orthogonal to the flow velocity. For a given reference frame $E = P^0$ (Notice that E is not an invariant scalar!)

$$\begin{aligned} dE &= d^3\Sigma_\mu T^{0\mu} = \tau A \left[eu^0 u^\mu - p\Delta^{0\mu} + \pi^{\mu 0}\right] u_\mu d\eta \\ &= \tau A\, e\, u^0\, d\eta = \tau A\, e\, \cosh\eta\, d\eta. \end{aligned} \tag{5.7}$$

Integrating this between η_{max} and η_{min}, leads to

$$E_i = E_1 + E_2 = \tau_0 e(\tau_0) A (\sinh\eta_{max} - \sinh\eta_{min}) \,, \tag{5.8}$$

where $E_1 + E_2$ and $(\sinh\eta_{max} - \sinh\eta_{min})$ are frame dependent. Nevertheless, the equations for N and E have the same form in any boosted frame.

Then from these

$$\begin{aligned} n(\tau_0) &= \frac{N_1 + N_2}{\tau_0\, A\, (\eta_{max} - \eta_{min})} \\ e(\tau_0) &= \frac{E_1 + E_2}{\tau_0\, A\, (\sinh\eta_{max} - \sinh\eta_{min})} \end{aligned} \tag{5.9}$$

Here the second equation indicates that in case of a boosted frame $(E_1 + E_2)$ changes the same way as $(\sinh\eta_{max} - \sinh\eta_{min})$, while $e(\tau)$ is boost invariant.

Now for the longitudinal momentum

$$P_z = \int d^3\Sigma_\mu T^{z\mu} \tag{5.10}$$

and it follows that

$$\begin{aligned} P_z &= \tau_0 A \int [e u^z u^\mu - p\Delta^{z\mu} + \pi^{\mu z}] u_\mu d\eta \\ &= \tau_0 A \int e\, u^z\, d\eta = \tau_0 A\, e \int \sinh\eta\, d\eta, \end{aligned} \tag{5.11}$$

however, the integration for $[\eta_{min}, 0]$ is positive, while for $[0, \eta_{max}]$ negative, so

$$P_{iz} = P_{1z} - P_{2z} = \tau_0 A\, e\, (\cosh\eta_{max} - \cosh\eta_{min}) \ . \tag{5.12}$$

If we want to connect eqs. (5.8), and (5.12), with the experimental energy and momentum in the collider frame, we have to evaluate these in the reference frame of the collider, because we have separated the projectile and target contributions at $\eta = 0$ in that frame!

Comparing eqs. (5.8) and (5.12) we can express the total momentum of a streak in terms of the total energy, as

$$P_{1z} - P_{2z} = (E_1 + E_2) \frac{\cosh\eta_{max} - \cosh\eta_{min}}{\sinh\eta_{max} - \sinh\eta_{min}} \ . \tag{5.13}$$

This equation (may be /can be) used to determine z_{min} and z_{max}. Using

$$t = t_0 + \tau\cosh\eta, \qquad z = z_0 + \tau\sinh\eta \tag{5.14}$$

we get

$$\frac{P_{1z} - P_{2z}}{E_1 + E_2} = \frac{t_{max} - t_{min}}{z_{max} - z_{min}} \ . \tag{5.15}$$

Then using eq. (5.1) and observing that $\tau_{max} = \tau_{min} = \tau_0$, we get

$$\frac{P_{1z}-P_{2z}}{E_1+E_2} = \frac{\sqrt{\tau_0^2 + (z_{max}-z_0)^2} - \sqrt{\tau_0^2 + (z_{min}-z_0)^2}}{z_{max} - z_{min}} \,. \tag{5.16}$$

At finite impact parameter the asymmetry of the projectile and target side leads to a finite momentum, P_{iz}, for the peripheral streak i.

5.3 The implementation of the model

The implementation of the model is rather involved, the complete mathematical deduction can be seen in Ref. 7 of Appendix C. This work has not been published yet, thus here we extract some significant points:

1) From the given transverse resolution of streaks, the impact parameter, and the beam energy we can get the total net baryon charge, N_i, energy, E_i and momentum, P_{iz} of streak i, the same way as this is done in ref. [3]. Thus the calculation starts from the the central, $i = c$, streak.

2) It is assumed that $e_i(\tau_0) = e_c(\tau_0) =$ const. for all streaks, i, at initial time τ_0.

3) From the Fig. 5.1, we assumed that the front end of the side streak is at the same point as that of the central streak (as seen in Fig. 5.3), but the time coordinate of the mid point of the side streak, t_{imid_P}, falls on the hyperbola of the central streak.

4) The fluid elements show a Bjorken type of scaling expansion:

$$e_i(\tau') = e_c(\tau_0) \left(\frac{\tau'}{\tau_0}\right)^{-4/3} \text{ and } \; n_i(\tau') = n_c(\tau_0) \left(\frac{\tau'}{\tau_0}\right)^{-1} \,.$$

5) In this IS model, different streaks may have different mathematical origin of space-time hyperbola, thus they have different final state hypersurfaces. However, it is difficult for a hydrodynamic model to deal with multiple hypersurfaces, when we connect the IS model to a hydrodynamic model. Thus we have to chose a single hypersurface, and then propagate all the other hypersurfaces of different streaks to this chosen hypersur-

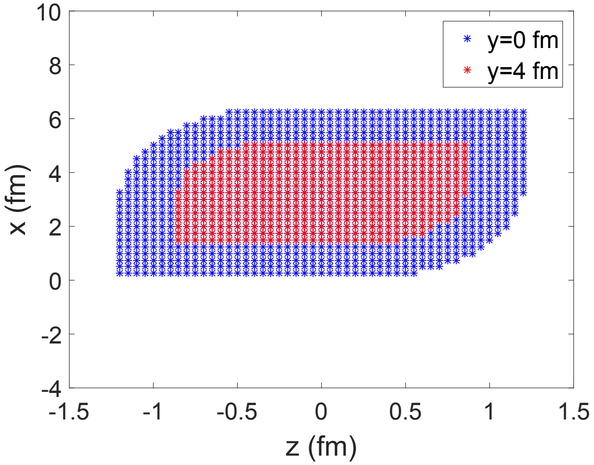

Figure 5.3: The initial configuration of the streaks in the reaction plane, on the $[x, \eta, \tau_0 = 1\text{fm/c}]$-hypersurface for $y = 0$ (blue streaks) and for $y = 4\text{fm}$ (red streaks) overlayed. The streak energy density is uniform and it is the same for all streaks. The configuration is qualitatively similar to the parton cascade result shown in Fig. 5.1. This example is calculated for a Au+Au reaction at 100+100 GeV/nucl. energy and impact parameter $b = 0.5(R_{Pb} + R_{Pb}) = 6.5\text{fm}$. The central streak lenght is 2.36 fm with a uniform energy density of $e_c = 156.31\text{GeV/fm}^3$, and $\tau_0 = 1.0\text{fm}$. The $y = 0$ plane crosses the x-axis at $x = 3.25\text{fm}$. All the other figures were calculated with the same reaction parameters.

face, which in our model is a constant time t hypersurface or a constant proper time τ hypersurface.

Finally, we show here the final energy density and baryon density distribution after Bjorken expansion and propagation, in Fig. 5.4, where a constant time $t = 1.78 fm/c$ hypersurface is chosen.

5.4 Shear and Vorticity

The parametrically constructed initial state, can be utilized in different calculation frames, and it is able to incorporate initial shear, in contrary to several other initial state parametrizations. The lack of initial shear reduces the vorticity and possibility for polarization in these models, which contradicts to recent observations.

The velocity distribution in the presented Initial State models are shown in the two

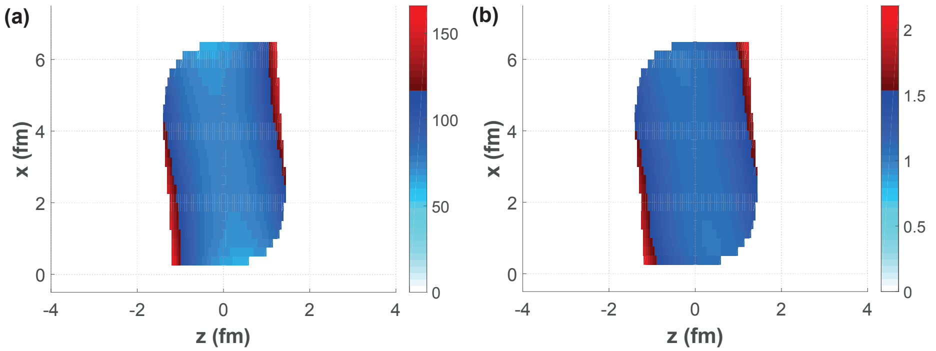

Figure 5.4: The reaction plane, $y = 0$, $[x, z]$ contour plot of the energy density (left panel) and baryon density (right panel) in units of GeV/fm^3 and fm^3, propagated to the constant time, $t_{is} = 1.78\text{fm}/c$ hypersurface. The propagated initial density shows maximal energy densities at the forward and backward edges of the reaction plane. The baryon density distribution is proportional with the energy density distribution as a consequence of the assumption that the energy density and baryon charge density are uniform at $\tau_i = \tau_0$ for each streak in its own frame as shown in Fig. 5.3. The space-time dependence arises from the propagation to the t_{is}=const. hypersurface. The reaction parameters are the same as listed in Fig. 5.3

subfigures of Fig. 5.5 in the reaction plane, $y = 0$. In both cases among the different layers of the matter there is considerable shear, particularly for peripheral layers, e.g. $y = 4$fm, see the left panel of Fig. 5.5. The right one of Fig. 5.5 indicates that the velocity profile shows dominant longitudinal expansion, which gradually may decrease the central shear. Thus, the development of Kelvin Helmholtz Instability (KHI) [48] in this configuration is less probable than it is described in earlier calculations with a different initial state.

The shear will lead to strong vorticity. This vorticity vector pointing in the $-y$ direction, dominates the vorticies developing due to the expansion later in the flow. Furthermore, due to symmetry reasons the vorticities in the other directions cancel each other to a large extent [41, 58], except eventual unbalanced vorticities due to random fluctuations [70, 71].

The Energy weighted classical vorticity, $\omega_y(x, \eta)$ is shown in Fig. 5.6 (left). This component is overall negative arising from the initial rotation, i.e. it is pointing in the

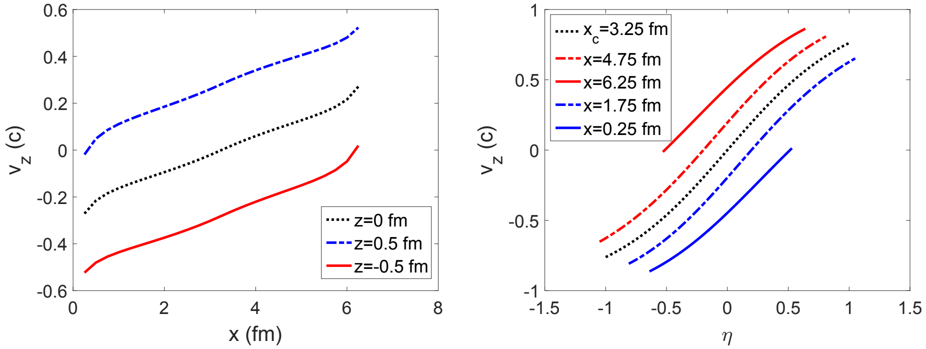

Figure 5.5: The left panel is z-directed velocity distribution versus the x position (at $y = 0$), in the $z = 0$fm central plane (dash line) propagated to the constant time, $t_{is} = 1.78$fm/c hypersurface. The velocity distribution for the $z = \pm 0.5$fm forward/backward shifted positions are shown by dash-dotted and solid lines respectively. The right panel is the z-directed velocity distribution versus the η coordinate (at $y = 0$), for the central streak (at $x_c = 3.25$ fm). Semi-peripheral streaks ($x = 1.75\,\&\,4.75$ fm) and peripheral streaks ($x = 0.25\,\&\,6.25$ fm), propagated to the constant proper time, $\tau_{is} = 1.0$ fm/c hypersurface are also shown. The reaction parameters are the same as listed in Fig. 5.3

$-y$ direction. The central part of the momentum domain at this initial moment shows smaller vorticity, due to the Bjorken expansion of the model.

The classical vorticity, $\omega_x(y, \eta)$ is shown in Fig. 5.6 (right). This component is antisymmetric across the $y = 0$ surface. As a consequence the contribution of this component vanishes in the complete averaging. The central part of the domain at this initial moment shows smaller vorticity.

The vorticity is observed via the observed polarization, Π_y, of emitted Λ and $\bar{\Lambda}$ particles [15, 19, 55]. The symmetries of the vorticity field and of the momentum dependence of the polarizations are tightly related [15]. The present experiments show only the overall Λ and $\bar{\Lambda}$ polarizations summed up for all emission momenta. Thus, in the c.m. frame the polarization components, Π_x and Π_z must vanish, due to the symmetries of vorticity components, ω_x and ω_z, except a smaller contribution from random fluctuations.

At the same time the x and y vorticity components carry valuable information, but these can only be extracted if the participant c.m. is identified Event by Event (EbE) [42, 63]. This identification based on the spectators detected via the zero degree calorime-

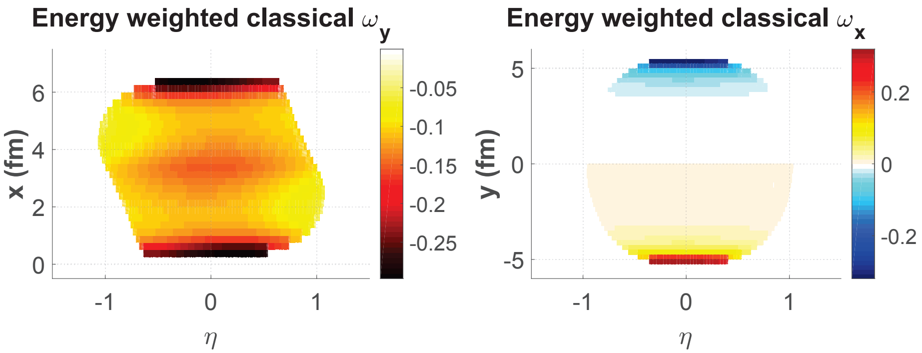

Figure 5.6: The left panel is y-component of the classical energy weighted vorticity on the $[x, \eta]$ plane, at $y = 0$. This is the dominant component of vorticity, and it points everywhere in the $-y$ direction. This example is obtained by propagation of the initial configuration to the c.m. hypersurface at $\tau = \tau_0 = 1$fm/c. The at the upper and lower edges the vortcity approaches -0.3. The right panel is x-component of the classical vorticity on the $[y, \eta]$ plane at $x = 3.0$fm. This component of vorticity, has similar values as the y component, but it is antisymmetric, $\omega_x(y_{max}, \eta = 0) = -\omega_x(y_{min}, \eta = 0)$. So the two identical but opposite signed vorticites yield a vanishing overall sum.

ters is not performed yet experimentally [64], due to assumed, unrelated fluctuations of other origins. Now this identification method could be tested by evaluating the sum of polarizations, Π_x and Π_z, with and without EbE identification of participant c.m. With c.m. identification the x and y polarization components should vanish or become minimal. The $\Pi_x(\boldsymbol{p})$ and $\Pi_z(\boldsymbol{p})$ distributions should also show the symmetries arising from the symmetries of the vorticities. This will provide valuable information on the details of the initial state models, which cannot be easily detected in other ways.

5.5 Discussion

The presented model is a simple realization for peripheral heavy-ion collisions, with initial shear and vorticity, in Milne coordinates. Unlike the large majority of the Bjorken type of models that do not discuss the longitudinal degrees of freedom, we divide the transverse plane to streaks, which are longitudinally finite. At every transverse point $i \equiv [x, y]$ we have a longitudinal streak with well defined end points, $z_{i,P}^{max}$ and $z_{i,P}^{min}$ or the corresponding points in Milne coordinates $\eta_{i,P}^{max}$ and $\eta_{i,P}^{min}$ on the Projectile side. We describe the Target side similarly. We obtain these points from the streak by streak energy and momentum conservation, and from simple assumptions regarding the streak ends and streak center points.

There exist a few models in Milne coordinates, which do discuss the longitudinal degrees of freedom in the collisions, and satisfy energy and momentum conservations. For example ref. [72] introduces streak ends, $z_p(\tau)$ and $z_t(\tau)$, but these are uniform, i.e. identical for all transverse points. This model could be generalized in the same way to varying peripheral streaks, so that energy and momentum conservation is applied streak by streak, and as a consequence shear and vorticity will be included in the model. In this case every transverse streak would have a different constant proper time hyperbola, with different origins in the space-time $[t_{i0}, z_{i0}]$.

In case of Color Glass Condensate in the initial state, the colour field slows down the leading charges of the expanding system, as discussed in [73–75]. One can follow the trajectory of the longitudinal edges up to a τ =const. hypersurface at space-time rapidities η_1^* and η_2^*. These values limit the longitudinal extent of the flux-tube with the gluon field or plasma. The field may even contribute to a large compression of the baryon charge at the forward and backward edges [68, 76]. This model could also be generalized to varying peripheral streaks, so that energy and momentum conservation is applied streak by streak and the streak ends, η_1^* and η_2^*, would be different in each peripheral streak, i.

The model parametrization can be adjusted to the different parton cascade approaches, and field theoretical considerations, and thus it may provide a base for further studies of different physical processes.

Chapter 6

Summary and outlook

In this work, based on hydrodynamic simulation of high-energy collisions, we have studied the polarization vector from relativistic spin thermodynamics. We firstly developed an analytics solution for an Exact rotating model in non-relativistic limits, finding that the second term of the polarization vector, arising from system expansion, has a comparable contribution as the first term arising from vorticity. Then we predicted the polarization effect at NICA and FIAR energies, and explore the dependence of polarization on different parameters, e.g. the impact parameter, collision energy and evolution time. Our results fit very well with the experimental results and theoretical expectations.

Nowadays people have comprehended rather well the polarization effects in heavy ion collisions, but many problems still exists in this field. Here we extract some interesting points:

1) What is the full relativistic fluid dynamics for a particle system with spin?

We have introduced the relativistic thermodynamics with spin in Section 3.2, starting from the modified partition function of the system, but in fact we have also included there the hydrodynamics by calculating the particle 4-current and energy-momentum tensor. However, there was still no fluid dynamics for spin system developed so far. A recent Ref. [77], has proposed a fluid dynamical framework with spin to help us to understand the space-time evolution of spin and polarization.

2) Why is the polarization of Λ at RHIC BES program is larger than that of anti-Λ?

A speculation was that the polarization induced by the magnetic field created in heavy ion collisions may split the polarization effect arising from the vorticity. However, the recent STAR results showed a vanishing magnetic field, and even if the magnetic field exists its duration time is too short. Some people also suggested that the baryon chemical potential will influence the splitting effect [59], but finally it turned out that the splitting induced by chemical potential is rather small and thus can not account for the large difference. A recent Ref. [78], attempted to connect the polarization effect with axial anomaly in Chiral Vortical Effect, and then attributed the splitting effect to smaller number of anti-Λs than Λs while the axial charge is the same for both.

3) What is the relation between the final hyperon polarization and the quark's Chiral Vortical Effect?

The Chiral Vortical Effect (CVE) is in essence also a kind of spin polarization effect induced by rotation, but when considering the chirality restoration of massless quark in hot dense QGP, the quarks and anti-quarks will move in opposite directions, thus leading to a current, which is called the 'CVE'. What is the relation between them? Can we predict the other one when we know one of them? The Ref. [78] is a good attempt.

The polarization effect induced by rotation in high-energy collisions is an exciting research field, which can help to decipher the spin and quark's QCD behavior. This field is developing very fast, and I hope we could continue to work out more creative results after this thesis.

Bibliography

[1] Introduction to Relativistic Heavy Ion Collisions, L.P. Csernai, (John Wiley and Sons, Chichester, 1994) ISBN-471-93420-8.

[2] L.D. Landau, Izv. Akad. Nauk Ser. Fiz. **17**, 51 (1953).

[3] V.K. Magas, L.P. Csernai and D.D. Strottman, Phys. Rev. C **64**, 014901 (2001); Nucl. Phys. A **712**, 167 (2002).

[4] F. Cooper and G. Frye, Phys. Rev. D **10**, 186 (1974).

[5] L.P. Csernai, Zh. Eksp. Teor. Fiz. **92**,379 (1987); Sov. JETP **65**, 213 (1987).

[6] K.A. Bugaev, Nucl. Phys. A **606**, 559 (1996).

[7] Cs. Anderlik, L.P. Csernai, F. Grassi, Y. Hama, T. Kodama, Zs. Lázár and H. Stöcker, Heavy Ion Phys. **9**, 193 (1999).

[8] K. Tamosiunas and L.P. Csernai, Eur. Phys. J. A **20**, 269 (2004).

[9] B. McInnes, and E. Teo, Nucl. Phys. B **878**, 186 (2014).

[10] B. McInnes, Nucl. Phys. B **887**, 246 (2014).

[11] K. Okamoto, C. Nonaka, and Y. Akamatsu, Poster, presented at: The XXV International Conference on Ultrarelativistic Nucleus-Nucleus Collisions, Sept. 27 - Oct. 3, 2015, Kobe, Japan; (published electronically).

[12] L.G. Pang, G.-Y. Qin, V. Roy, X.-N. Wang, and G.-L. Ma, Invited talk presented at: The XXV International Conference on Ultrarelativistic Nucleus-Nucleus Collisions, Sept. 27 - Oct. 3, 2015, Kobe, Japan; (published electronically).

[13] L.P. Csernai, V.K. Magas, and D.J. Wang, Phys. Rev. C **87**, 034906 (2013).

[14] L.P. Csernai, D.J. Wang, and T. Csörgő, Phys. Rev. C **90**, 024901 (2014).

[15] F. Becattini, V. Chandra, L. Del Zanna, and E. Grossi, Annals of Physics **338**, 32 (2013).

[16] T. Csörgő, and M.I. Nagy, Phys. Rev. C **89**, 044901 (2014).

[17] F. Becattini, L. Tinti, Annals of Physics **325**, 1566 (2010).

[18] F. Becattini, Phys. Rev. Lett. **108**, 244502 (2012).

[19] F. Becattini, L.P. Csernai, and D.J. Wang, Phys. Rev. C **88**, 034905 (2013).

[20] L.P. Csernai, and J.H. Inderhaug, Int. J. Mod. Phys. E **24**, 1550013 (2015).

[21] F. Becattini, G. Inghirami, V. Rolando, A. Beraudo, L. Del Zanna, A. De Pace, M. Nardi, G. Pagliara, and V. Chandra, Eur. Phys. J. C **75**, 406 (2015).

[22] G.-Y. Chen, and R.J. Fries, Phys. Lett. B **723**, 417 (2013).

[23] G. Graef, M. Bleicher, and M. Lisa, Phys. Rev. C **89**, 014903 (2014).

[24] J. Kapusta, R.J. Fries, G.-Y. Chen, and L. Yi, Invited talk presented at The XXV International Conference on Ultrarelativistic Nucleus-Nucleus Collisions, Sept. 27 - Oct. 3, 2015, Kobe, Japan; (published electronically).

[25] M. A. Lisa, Invited talk at the XI workshop on Particle Correlations and Femtoscopy (WPCF2015), November 3-7, 2015, Warsaw, Poland.

[26] G. Bunce, R. Handler, R. March, P. Martin, L. Pondrom, and M. Sheaff, Phys. Rev. Lett. **36**, 1113 (1976).

[27] A. Lesnik, D. M. Schwartzf, I. Ambats, E. Hayes, W. T. Meyer, C. E. W. Ward, T. M. Knasel, 5 E. G. Swallow, and R. Winston II, and T. A. Romanowski, Phys. Rev. Lett. **35**, 770 (1975).

[28] M. Anikina *et al.*, Z. Phys. C: Particles and Fields **25**, 1 (1984).

[29] A. M. Smith *et al.* (R608 Collaboration), Phys. Lett. B **185**, 209, (1987).

[30] E. J. Ramberg *et al.*, Phys. Lett. B **338**, 403-408, (1994).

[31] A. Morelos *et al.* (E761 Collaboration), Phys. Rev. Lett. **71**, 2172, (1993).

[32] I. Abt *et al.* (HERA-B Collaboration), Phys. Lett. B **638**, 415-421, (2006).

[33] I. Selyuzhenkov *et al.*(STAR Collaboration), J. Phys. G: Nucl. Part. Phys. **32**, S557-S561 (2006).

[34] B. I. Abelev *et al.*, Phys. Rev. C **76**, 024915 (2007).

[35] Z.-T. Liang, and X.-N. Wang, Phys. Rev. Lett. **94**, 102301 (2005).

[36] X.-G. Huang, P. Huovinen, and X.-N. Wang, Phys. Rev. C **84**, 054910 (2011).

[37] B. Betz, M. Gyulassy, and G. Torrieri, Phys. Rev. C **76**, 044901 (2007).

[38] A. D. Panagiotou, Phys. Rev. C **33**, 1999 (1986).

[39] C.C. Barros and Y. Hama, arXiv:hep-ph/0507013v1.

[40] Y.-L. Xie, R.C. Glastad, and L.P. Csernai, Phys. Rev. C **92**, 064901 (2015).

[41] Y.L. Xie, M. Bleicher, H. Stöcker, D.J. Wang, and L.P. Csernai, Phys. Rev. C **94**, 054907 (2016).

[42] L. P. Csernai, G. Eyyubova, and V. K. Magas, Phys. Rev. C **86**, 024912 (2012).

[43] F. Becattini, F. Piccinini, and J. Rizzo, Phys. Rev. C **77**, 024906 (2008).

[44] J.-H. Gao, S.-W. Chen, W.-T. Deng, and Z.-T. Liang, Q. Wang, and X.-N. Wang, Phys. Rev. C **77**, 044902 (2008).

[45] I. Karpenko and F. Becattini, arXiv:1610.04717.

[46] M. A. Lisa *et al.* (STAR Collaboration), Invited talk presented at the QCD Chirality Workshop 2016, Feb. 23-26, 2016, Los Angeles, USA.

[47] T. A. DeGrand, and H. I. Miettinen, Phys. Rev. D **24**, 2419 (1981).

[48] L. P. Csernai, D. D. Strottman, and Cs. Anderlik, Phys. Rev. C **85**, 054901 (2012).

[49] D. Montenegro, L. Tinti, and G. Torrieri, arxive:1701.08263.

[50] L. P. Csernai, D. J. Wang, M. Bleicher, and H. Stöcker, Phys. Rev. C **90**, 021904(R) (2014).

[51] L. P. Csernai, J. I. Kapusta, L.D. McLerran, Phys. Rev. Lett. **97**, 152303 (2006).

[52] X.-G. Huang, P. Huovinen, and X.-N. Wang, Phys. Rev. C **84**, 054910 (2011).

[53] Z.-T. Liang and X.-N. Wang, Phys. Lett. B **629**, 20-26 (2005).

[54] Y. Cheng, L. P. Csernai, V. K. Magas, B. R. Schlei, and D. D. Strottman, Phys. Rev. C **81**, 064910 (2010).

[55] F. Becattini, L. P. Csernai, D. J. Wang, and Y. L. Xie, Phys. Rev. C **93**, 069901(E) (2016).

[56] Y. Jiang, Z.-W. Lin, and J.-F. Liao, arXiv:1602.06580v1.

[57] L. P. Csernai and J. I. Kapusta, Phys. Rev. D **31** 2795 (1985).

[58] Y. L. Xie, D. J. Wang, L. P. Csernai, Phys. Rev. C **95** 031901(R) (2017).

[59] R.-H. Fang, L.-G. Pang, Q. Wang, and X.-N. Wang, Phys. Rev. C **94**, 024904 (2016).

[60] J.-L. Zhang *et al.* (STAR Collaboration), Invited talk presented at the 16th International Conference on Strangeness in Quark Matter, Jun. 27-July 1, 2016, Berkeley, USA.

[61] T. Anticic *et al.* (NA49 Collaboration), Phys. Lett. B **93**, 022302-1 (2004).

[62] W.-T. Deng and X.-G. Huang, Phys. Rev. C **93**, 064907 (2016).

[63] L. P. Csernai and H. Stöcker, J. Phys. G **41**, 124001 (2014).

[64] J. Schukraft (private communication).

[65] D.-M. Zhou, Y.-L. Yan , X.-L. Li , X.-M. Li, B.-G. Dong, X. Cai, B.-H. Sa, Computer Physics Communications **193**, 8994 (2015).

[66] V. Vovchenko, Iu. A. Karpenko, M.I. Gorenstein, L.M. Satarov, I.N. Mishustin, B. Kämpfer, and H. Stöcker, Phys. Rev. C **94**, 024906 (2016), [arXiv:1604.06346];

[67] W.-T. Deng, and X.-G. Huang, arXiv: 1609.01801 [nucl-th].

[68] M. Gyulassy, and L.P. Csernai, Nucl. Phys. A **460**, 723 (1986).

[69] I.N. Mishustin, and K.A. Lyakhov, Phys. Rev. C **76**, 011603 (2007). I.N. Mishustin, and K.A. Lyakhov, Physics of Atomic Nuclei, **75**, 371 (2012).

[70] S. Floerchinger and U.A. Wiedemann, Phys. Rev. C **88**, 044906 (2013).

[71] S. Floerchinger and U. A. Wiedemann, Journal of High Energy Physics, **11**, 100 (2011); and J. Phys. G: Nucl. Part. Phys. **38**, 124171 (2011).

[72] I.N. Mishustin and K.A. Lyakhov, Physics of Atomic Nuclei, **75**, 371-392 (2011).

[73] R. J. Fries, J. I. Kapusta and Y. Li, Nucl. Phys. A **774**, 861-864 (2006).

[74] S. Ozonder and R.J. Fries, Phys. Rev. C **89**, 034902 (2014).

[75] G. Chen, R.J. Fries, J.I. Kapusta and Y. Li, Pgys. Rev. C **92**, 064912 (2015).

[76] Ming Li and Joseph I. Kapusta, Phys. Rev. C **95**, 011901(R) (2017).

[77] W. Florkowski, B. Friman, A. Jaiswal, and E. Speranza, arXiv:1705.00587.

[78] A. Sorin, O. Teryaev, Phys. Rev. C **95**, 011902(R) (2017).

[79] I.S. Gradstein, and I.M. Ryzhik, *Table of integrals, series, and products* (Academic Press, 2007).

[80] L.P. Csernai, S. Velle, and D.J. Wang, Phys. Rev. C **89**, 034916 (2014).

[81] Horst Stöcker: *Taschenbuch Der Physik*, (Harri Deutsch, 2000), 1.3.2/6d.

Appendix A

The CFD cell structure

In computational fluid dynamics (CFD) the configuration space is divided into many fluid cells. These fluid cells are spatially cubic and have the same cell size, d, in all spatial directions. The x, y, z axes situate at the edge lines of the first row cells in 3 directions, thus they are parallel to all the edges of the cells. The centers of the first row cells are at a distance $\frac{1}{2}d$ to the 3 axes.

It is sufficient to describe the cells only at positive y coordinate, since we have a initial state which is symmetric on negative and positive y direction with respect to the reaction $[x, z]$ plane. This means the negative y side cells are just the mirror image of the positive side ones. Thus, the cells with negative y values are not calculated and stored in the code.

By labeling each cell center by the indexes i, j, k for x, y, z axes, the coordinate of the cell with index i, j, k is defined as:

$$\boldsymbol{x}_{ijk} = \left((i - i_{mid} - \frac{1}{2})d,\ (j - \frac{1}{2})d,\ (k - k_{mid} - \frac{1}{2})d\right), \tag{A.1}$$

where

$$\begin{aligned} i &= i_{min}, i_{min}{+}1,\ i_{min}{+}2, \ldots\ i_{max}\ , \\ j &= 1,\ 2,\ 3, \ldots\ j_{max}\ , \\ k &= k_{min},\ k_{min}{+}1,\ k_{min}{+}2, \ldots\ k_{max}\ . \end{aligned}$$

Here we always choose the values $i_{min} > 0$ and $k_{min} > 0$ in order to avoid zero or negative i, j, k indexes. i_{mid} and k_{mid} are used to determine the center of mass and the center of our calculation frame at $\boldsymbol{x} = (0, 0, 0)$. The $x = 0$ line locates between the cells with indexes i_{mid} and $i_{mid}{+}1$. The $z = 0$ line locates between the cells with indexes k_{mid} and $k_{mid}{+}1$. The $y = 0$ line just lie on the edges of $j = 1$ cells. Since the negative y-directed cells are not stored in the list, when we calculate some measurable quantities, i.e., the two particle correlation calculation and the Λ polarization, we should not forget to take into account the contribution by the mirror image side. These mirror side cells have the same invariant scalar quantities as positive cells while the 4-vector components take different values:

$$\begin{aligned} q(-x,-y,-z) &= q(x,y,z)\ , \\ \gamma(-x,-y,-z) &= \gamma(x,y,z)\ , \\ v_x(-x,-y,-z) &= -v_x(x,y,z)\ , \\ v_y(-x,-y,-z) &= -v_y(x,y,z)\ , \\ v_z(-x,-y,-z) &= -v_z(x,y,z)\ , \end{aligned} \tag{A.2}$$

where the 4-velocity is $u^\mu = \gamma(1, v_x, v_y, v_z)$ and the spatial velocity $\boldsymbol{v} = (v_x, v_y, v_z)$. The cell with indexes $(i,\ j,\ k)$ always has the corresponding mirror image cell with the indexes $(i,\ j,\ k)\ \longrightarrow\ (\,2i_{mid}{-}i{+}1,\ -j,\ 2k_{mid}{-}k{+}1\ )$.

Appendix B

Analytic solution for Λ polarization in non-relativistic limit

As the Λ is transversely polarized, $\Pi^\mu p_\mu = 0$, one can confine himself to the spatial part of Π^μ. The simplified spatial part of polarization vector is:

$$\mathbf{\Pi}(p) = \frac{\hbar\epsilon}{8m} \frac{\int dV n_F(x,p)\,(\nabla \times \boldsymbol{\beta})}{\int dV n_F(x,p)} + \frac{\hbar \boldsymbol{p}}{8m} \times \frac{\int dV n_F(x,p)\,(\partial_t \boldsymbol{\beta} + \nabla \beta^0)}{\int dV n_F(x,p)} \,. \tag{B.1}$$

where $n_F(x,p)$ is the phase space distribution of the Λs. In a previous calculation [19], the p dependence of n_F, was considered negligible in the integral and the time derivative and gradient terms were also assumed to be smaller. The present calculation shows that in general these terms are not negligible and that which terms are dominant depends on the particular conditions.

We adopt the parametrization of the model from Ref. [20], with the initial conditions $R_0 = 2.5$ fm, $Y_0 = 4.0$ fm, $\dot{R}_0 = 0.20$ c, $\dot{Y}_0 = 0.25$ c, $\omega_0 = 0.1$ c/fm, $\kappa = 3/2$, $T_0 = 300$ MeV. For this configuration $E_{tot} = 576$ MeV/nucl.

B.1 The denominator

We first perform the integral in the denominator:

$$A(p) \equiv \int dV\, n_F = \int\limits_{0}^{R} r\, dr \int\limits_{-Y}^{+Y} dy \int\limits_{0}^{2\pi} d\phi\; n_F(x,p) \ . \tag{B.2}$$

According to Eq. (3) in Ref. [20] in terms of the scaling variable, s, we have:

$$\begin{aligned} n &= n_0 \frac{V_0}{V} \nu(s) \ , && \text{(B.3)} \\ \nu(s) &= \frac{1}{\tau(s)} \exp\left(-\frac{1}{2} \int_0^s \frac{du}{\tau(u)} \right) \\ &= 1 \cdot \exp\left(-\frac{1}{2} \int_0^s du \right) \ , && \text{(B.4)} \end{aligned}$$

where the simplifying choice of $\tau(s) = 1$ is used in the last step. Therefore:

$$n(s) = n_0 \frac{V_0}{V} e^{-\frac{1}{2}s} \ . \tag{B.5}$$

The EoS is assumed to be: $\epsilon(s) = \kappa T(t) n(s)$ and the energy density $\epsilon(s)$ is calculated as in Eq. (29) in Ref. [20], therefore:

$$n(s) = \frac{\epsilon}{\kappa T(t)} = \frac{C_N}{\kappa T} e^{-\frac{s_y}{2}} e^{-\frac{s_\rho}{2}} \ , \tag{B.6}$$

where $C_N = \kappa n_0 T_0 (\frac{V_0}{V})^{1+1/\kappa}$.

From Ref. [19], the Fermi-Jüttner distribution is:

$$n_F(x,p) = \frac{1}{e^{p^\mu \beta_\mu - \xi} + 1} \approx \frac{1}{e^{p^\mu \beta_\mu - \xi}} = \frac{e^{\mu/T}}{e^{p^\mu \beta_\mu}} \ , \tag{B.7}$$

where the $\xi = \mu/T$, and μ is the chemical potential. The thermal flow velocity, $\beta^\mu(x) \equiv u^\mu(x)/T$, is different at different space-time points x.

The invariant scalar density for the Jünttner distribution is:

$$n = \frac{4\pi m^2 K_2(m/T)}{(2\pi\hbar)^3} e^{\mu/T} = \frac{e^{\mu/T}}{C_0} \tag{B.8}$$

where the $C_0^{-1} = 4\pi m^2 T K_2(m/T)/(2\pi\hbar)^3$. With C_0 and $n(s) = n$, the Fermi-Jüttner distribution can be written as:

$$n_F(x,p) = \frac{e^{\mu/T}}{e^{p^\mu \beta_\mu}} = \frac{C_0 n(s)}{e^{p^\mu \beta_\mu}} \ . \tag{B.9}$$

Now we introduce cylindrical coordinates for the location in the configuration place $x = (r, y, \phi)$, and using the scaling expansion model [14, 16] with the scaling variables s , s_r , s_y. Now, substituting Eqs. (B.6,B.9) into the denominator of $\Pi(p)$, and parametrizing the range of integrations as in [20] one obtains:

$$A(p) = \frac{C_N C_0}{\kappa T} \int_{-aY}^{aY} dy \ \exp\left(-\frac{y^2}{2Y^2}\right) \int_0^{bR} r dr \ \exp\left(-\frac{r^2}{2R^2}\right) \int_0^{2\pi} d\phi \, e^{-p^\mu \beta_\mu} \ . \tag{B.10}$$

The scalar product in cylindrical coordinates takes the form $p^\mu \beta_\mu = (p^0, \boldsymbol{p})(\beta_0, \boldsymbol{\beta}) = p^0 \beta_0 - \boldsymbol{p}\,\boldsymbol{\beta} = p^0 \beta_0 - p_r \beta_r - p_y \beta_y - p_\phi \beta_\phi$.

In our integral the p^μ is given or 'fixed' as the argument of $\boldsymbol{\Pi}(p)$, while the $\boldsymbol{\beta} = \boldsymbol{\beta}(x)$ is changing. The integration with respect to ϕ starts from the direction of the $\boldsymbol{p}$-vector. According to the Eq. (5) in [20]:

$\boldsymbol{v} = v_r \boldsymbol{e}_r + v_\phi \boldsymbol{e}_\phi + v_y \boldsymbol{e}_y = \frac{\dot{R}}{R} r \boldsymbol{e}_r + \omega r \boldsymbol{e}_\phi + \frac{\dot{Y}}{Y} y \boldsymbol{e}_y$, and $\boldsymbol{\beta} = u^i/T = \gamma \boldsymbol{v}/T$. Thus, in the integral for ϕ we exploit the fact that in the Exact model the radial, r, and axial, y, components of the thermal velocity, $\boldsymbol{\beta}$, do not depend on ϕ, while the tangential component does not depend on y, i.e. $\beta_\phi = \gamma r\, \omega/T$, but its direction is changing with respect to the direction of $\boldsymbol{p}$. As the integral is over the whole 2π angle we can start it at any point of ϕ, so we start it from the externally given $\boldsymbol{p}$-direction. Consequently, with this choice of the x-axis, $\boldsymbol{p} = (p_r, p_y, 0)$, and $p_z = p_\phi = 0$. In this azimuthally symmetric, exact model it is sufficient to calculate $\Pi(\boldsymbol{p})$ for one direction of $\boldsymbol{p}$ in the $[x, z]$-plane.

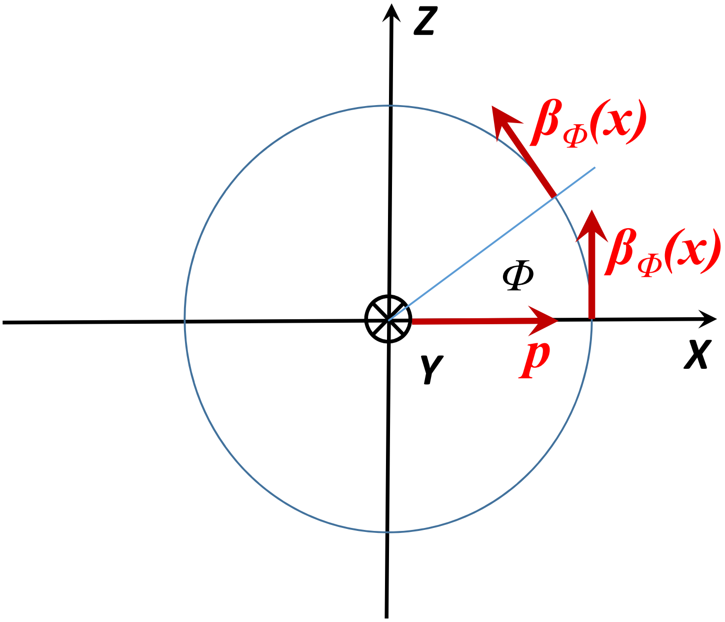

Figure B.1: (color online) The direction of axes, as well as the momentum, $\boldsymbol{p}$, and flow, $\boldsymbol{\beta}$, vectors. The azimuth angle is measured from the direction of the $\boldsymbol{p}$-vector, i.e. from the x-axis.

The direction of the thermal flow velocity, $\boldsymbol{\beta}$, is tangential to the direction ϕ, i.e. it points to the $\boldsymbol{e}_{\phi+\pi/2}$-direction. Thus, the scalar product is:

$$\boldsymbol{p}\cdot\boldsymbol{\beta}(r,\,y,\phi) = |p_x|\beta_r \cos{(\phi)} + p_y\beta_y + |p_x|\beta_\phi \cos\left(\phi{+}\frac{\pi}{2}\right)\ ,$$

where ϕ is the azimuth angle of the position around the y, rotation axis, counted starting from the x-axis. See Fig. B.1.

So, inserting the last expression for $p^\mu\beta_\mu$ into the last term of the integral Eq. (B.10), the integral with respect to ϕ will take the form:

$$\int_0^{2\pi} d\phi\, e^{-p^\mu\beta_\mu} = \int_{-\pi}^{\pi} d\phi\, e^{a\cos(\phi)-b\sin(\phi)} = 2\pi I_0\left(\sqrt{a^2{+}b^2}\right), \tag{B.11}$$

where $a = |p_x|\beta_r = |p_x|\gamma\dot{R}r/TR$ and $b = |p_x|\beta_\phi = |p_x|\gamma r\,\omega/T$, and we used integral no. 3.338(4) in [79]. If we define

$$c_3 = \sqrt{\left(\frac{p_x\gamma\dot{R}}{TR}\right)^2 + \left(\frac{p_x\gamma\,\omega}{T}\right)^2} = \frac{|p_x|\gamma}{T}\sqrt{(\dot{R}/R)^2 + \omega^2}\ ,$$

then $\sqrt{a^2+b^2} = c_3 r$, and:

$$\int_0^{2\pi} d\phi\, e^{-p^\mu\beta_\mu} = e^{-\gamma p^0/T}\, e^{p_y\beta_y} \times 2\pi I_0\left(c_3 r\right). \tag{B.12}$$

Now, substituting this back into Eq. (B.10):

$$\begin{aligned} A(p) &= \int dV\ n_F(p,s) \\ &= \frac{C_N C_0}{\kappa T}\int\limits_{-aY}^{aY} dr_y \int\limits_0^{bR} r\,dr\ \exp\left(-\frac{y^2}{2Y^2} - \frac{r^2}{2R^2}\right) \\ &\quad \times e^{-\gamma p^0/T}\, e^{p_y\beta_y} \cdot 2\pi I_0\left(c_3\, r\right)\ . \end{aligned} \tag{B.13}$$

Now we may use the same simplifying non-relativistic assumption as in Eq. (5) of Ref. [20], i.e. we approximate u^μ by v^μ as $\boldsymbol{v} = v_r\boldsymbol{e}_r + v_y\boldsymbol{e}_y + v_\phi\boldsymbol{e}_\phi = \frac{\dot{R}}{R}r\boldsymbol{e}_r + \frac{\dot{Y}}{Y}y\boldsymbol{e}_y + \omega r\boldsymbol{e}_\phi$, and thus $\gamma = 1$. It follows then:

$$\begin{aligned} A(p) &= \int dV\ n_F(p,s) \\ &= \frac{C_N C_0}{\kappa T}2\pi e^{-p^0/T}\int\limits_{-aY}^{aY} \exp\left(c_1 y - c_2 y^2\right)dy \int\limits_0^{bR} r\, I_0(c_3 r)\ \exp(-c_4 r^2)dr\ , \end{aligned} \tag{B.14}$$

where $c_1 = p_y\dot{Y}/(YT)$, $c_2 = 1/(2Y^2)$, $c_4 = 1/(2R^2)$ are constants.

Now we assume an infinite system with scaling Gaussian density profile, so that the integrals are evaluated up to infinity, i.e. the parameters $a = \infty$, $b = \infty$. Thus, the y

component integration in Eq. (B.14) is calculated as:

$$\int_{-\infty}^{+\infty} e^{c_1 y - c_2 y^2} dy = \sqrt{\frac{\pi}{c_2}} \exp\left(\frac{c_1^2}{4c_2^2}\right), \tag{B.15}$$

where we used the integral formula No. 2.33(1) in [79], and $\text{erf}\,(+\infty) = 1$, $\text{erf}\,(-\infty) = -1$.

For the integration of r component:

$$\int_0^{+\infty} r\, I_0(c_3 r)\, e^{-c_4 r^2} dr = \frac{1}{c_3\sqrt{c_4}} \exp\left(\frac{c_3^2}{8c_4}\right)\, M_{-\frac{1}{2},0}\left(\frac{c_3^2}{4c_4}\right), \tag{B.16}$$

where the $M_{-\mu,\nu}(z)$ is the so called 'Whittaker Function', No.6.643(2) in [79].

Now, we obtain the final form of Eq. (B.15):

$$A(p) = \frac{2\pi\sqrt{\pi}}{\kappa T} \frac{C_N C_0}{c_3\sqrt{c_2 c_4}} e^{-p^0/T} \exp\left(\frac{c_1^2}{4c_2^2}\right) \exp\left(\frac{c_3^2}{8c_4}\right)\, M_{-\frac{1}{2},0}\left(\frac{c_3^2}{4c_4}\right). \tag{B.17}$$

However, in the relativistic case, the integrations with respect to y and r can not be performed analytically, because of the presence of the factor $\gamma = 1/\sqrt{1 - v_r^2 - v_y^2 - v_\phi^2}$.

B.2 The numerator

Ref. [20] calculates the energy weighted vorticity, which is azimuthally symmetric, i.e. independent of the azimuthal angle ϕ. In the definition of the polarization, Eq. (B.1), we have $p^0\, n_F(p,x) = \epsilon\, n_F(p,x)$ for Λs with momentum p. In [20], however, the energy weighting is performed with the total energy density of the fluid $E_{tot} = E_{int} + E_{kin}$, which in general is not the same as $\epsilon\, n_F(p,x)$. On the other hand the bare vorticity is just a constant in the non-relativistic Exact model, while the EoS may be more general and it may lead to more involved $R(t)$ and $Y(t)$ dependence than the ideal Jüttner gas approximation would allow.

Thus, we use the direct, non-relativistic vorticity values, $\omega(t)$, from Ref. [20], and not the presented energy weighted vorticity. I.e.

$$\boldsymbol{\nabla} \times \boldsymbol{\beta} = -2\,\omega(t)\,\boldsymbol{e}_y/T(t)\ , \tag{B.18}$$

so that the thermal vorticity has only y-directed component in the Exact model. With the model parameters mentioned above, the thermal vorticity is $\hbar(\boldsymbol{\nabla} \times \boldsymbol{\beta}) = -0.13$ at $t = 0.5$ fm/c, and it decreases very slowly with time, about 1-2% per 1 fm/c. This constant vorticity will make the numerator simple:

$$B(p) \equiv \int dV\, n_F\big(\nabla \times \beta\big) = \frac{-2\omega \boldsymbol{e}_y}{T} \times A(p) \tag{B.19}$$

Therefore, the first term of polarization vector, i.e. Eq. (B.1) will be:

$$\boldsymbol{\Pi}_1(p) = -\frac{\hbar\epsilon}{8m}\frac{\int dV n_F(x,p)\,(\nabla{\times}\boldsymbol{\beta})}{\int dV n_F(x,p)} = \frac{\hbar\epsilon\omega}{4mT}\boldsymbol{e}_y, \tag{B.20}$$

which means the polarization vector arising from the vorticity, $\boldsymbol{\Pi}_1(p)$, in the Exact rotation model is a constant, (although time dependent), and parallel to the y-axis.

One may add the Freeze-Out (FO) probability to the integral. According to Ref. [80], the FO probability is $w_s = (p_\mu\, \hat{\sigma}_s^\mu)\ (\boldsymbol{p} \cdot \boldsymbol{u}(x))$, where the approximation is used that the FO direction, $\hat{\sigma}_s^\mu$ is parallel to the flow velocity, $\boldsymbol{u}(x) = \gamma \boldsymbol{v}(x)$. In the first term of the numerator, which depends on the constant y-directed vorticity this FO probability influences the numerator and denominator the same way, so the effect of the two integrals cancel each other in the FO probability also.

B.3 The second term

The numerator in second term of polarization vector reads:

$$\boldsymbol{C}(\boldsymbol{p}) \equiv \int dV n_F(x,p)\,(\partial_t \boldsymbol{\beta} + \boldsymbol{\nabla}\beta^0)\ . \tag{B.21}$$

If, in the non-relativistic limit, $\gamma = 1$ is assumed, then $\nabla\beta^0 = 0$, and $\partial_t\beta = \partial_t(\boldsymbol{v}/T)$, so we have to evaluate only the first term of the sum in the integrand. According to Ref. [20, 81], the time derivatives of velocity are:

$$\begin{aligned}
\partial_t v_r &= \left[(\frac{\ddot{R}}{R} - \frac{\dot{R}^2}{R^2}) - \omega^2\right] r \equiv c_5 r \\
\partial_t v_\phi &= \left(\dot{\omega} + 2\frac{\dot{R}}{R}\omega\right) r \equiv c_6 r \\
\partial_t v_y &= \left[\frac{\ddot{Y}}{Y} - \frac{\dot{Y}^2}{Y^2}\right] y \equiv c_7 y \ ,
\end{aligned} \tag{B.22}$$

where $c_5 = (\ddot{R}/R - \dot{R}^2/R^2 - \omega^2)$, $c_6 = (\dot{\omega} + 2(\dot{R}/R)\omega)$, and $c_7 = (\ddot{Y}/Y - \dot{Y}^2/Y^2)$.

Therefore,

$$\partial_t\boldsymbol{\beta} = \big(c_5 r\boldsymbol{e}_r + c_6 r\boldsymbol{e}_\phi + c_7 y\boldsymbol{e}_y\big)/T \ ,$$

provides the time-components of the vorticity in the three spatial directions. Here, as the model is symmetric, $\partial_t\beta_y$ vanishes, and with the model parameters mentioned above, at $t = 0.5$ fm/c and $r = 1$ fm $\frac{\hbar}{c}\partial_t\beta_r = 0.024$ and $\frac{\hbar}{c}\partial_t\beta_\phi = 0.009$. Both these vorticity components decrease slowly with time by about 0.0005 in 1 fm/c.

Eq. (B.21) is a volume integral of a vectorial quantity, which is not convenient to perform in cylindrical coordinates. So we transform it into Cartesian coordinates: $\boldsymbol{e}_r = \cos\phi\,\boldsymbol{e}_x + \sin\phi\,\boldsymbol{e}_z$, $\boldsymbol{e}_\phi = -\sin\phi\,\boldsymbol{e}_x + \cos\phi\,\boldsymbol{e}_z$. Therefore, $T\cdot\partial_t\boldsymbol{\beta} = \big(c_5\cos\phi - c_6\sin\phi\big)r\,\boldsymbol{e}_x + \big(c_5\sin\phi + c_6\cos\phi\big)r\,\boldsymbol{e}_z + c_7 y\,\boldsymbol{e}_y$.

The integral of Eq. (B.21) can be expanded as:

$$\begin{aligned}
\boldsymbol{C}(\boldsymbol{p}) &= \int dV n_F(x,p)\,\partial_t\boldsymbol{\beta} \\
&= \frac{C_N C_0}{\kappa T} e^{-p_0/T} \iiint r dr d\phi dy \,\exp\big(c_1 y - c_2 y^2\big) \\
&\qquad \times \exp\big(a\cos\phi - b\sin\phi - c_4 r^2\big)\,\partial_t\boldsymbol{\beta} \ ,
\end{aligned} \tag{B.23}$$

where a and b are defined after Eq. (B.11).

It is convenient to define an integrating operator, $\bar{A}$ as:

$$\begin{aligned}
\bar{A} &= \int dV n_F(x,p)\ \times \\
&= \iiint r\,dr\,d\phi\,dy\,e^{c_1 y - c_2 y^2} e^{a\cos\phi - b\cos\phi - c_4 r^2} \times\ ,
\end{aligned}$$

and then Eq. (B.23) will be:

$$\boldsymbol{C}(\boldsymbol{p}) = \bar{A} \cdot \partial_t \boldsymbol{\beta} \equiv \frac{1}{T}\left(I\boldsymbol{e}_x + J\boldsymbol{e}_z + H\boldsymbol{e}_y\right)\ , \tag{B.24}$$

where we defined:

$$\begin{aligned}
I &\equiv \bar{A} \cdot \big(c_5 \cos\phi - c_6 \sin\phi\big) r\ , \\
J &\equiv \bar{A} \cdot \big(c_5 \sin\phi + c_6 \cos\phi\big) r\ , \\
H &\equiv \bar{A} \cdot c_7 y\ .
\end{aligned}$$

Using the integral formula No. 2.33(6) of [79] the function H becomes:

$$H = \frac{2\pi\sqrt{\pi} C_N C_0}{\kappa T} e^{-p_0/T} \frac{c_7 c_1}{2 c_3 c_2 \sqrt{c_4 c_2}} \times \exp\left(\frac{c_3^2}{8c_4}\right) \exp\left(\frac{c_1^2}{4c_2^2}\right) M_{-\frac{1}{2},0}\left(\frac{c_3^2}{4c_4}\right)\ . \tag{B.25}$$

The function I can be expanded as a function of integrals over ϕ, r and y. The integral over ϕ brings in the Bessel function, $2\pi c_8 I_1(c_3 r)/c_3$ (See No. 3.937 (1) and (2) of [79]), where $c_8 = (c_5 a' - c_6 b')$, $a' = a/r = |p_x|\dot{R}/TR$, and $b' = b/r = |p_x|\omega/T$. Subsequently, the integral with respect to r brings in the 'Whittaker Function' and then the final form of I after performing the separable integration with respect to y leads to:

$$I = \frac{2\pi\sqrt{\pi} C_N C_0}{\kappa T} e^{-p_0/T} \frac{c_8}{c_3^2 c_4 \sqrt{c_2}} \times \exp\left(\frac{c_3^2}{8c_4}\right) \exp\left(\frac{c_1^2}{4c_2^2}\right) M_{-1,\frac{1}{2}}\left(\frac{c_3^2}{4c_4}\right)\ . \tag{B.26}$$

Evaluating the integral J is similar to I:

$$J = \frac{2\pi\sqrt{\pi}C_N C_0}{\kappa T} e^{-p_0/T} \frac{c_9}{c_3^2 c_4 \sqrt{c_2}} \times \exp\left(\frac{c_3^2}{8c_4}\right) \exp\left(\frac{c_1^2}{4c_2^2}\right) M_{-1,\frac{1}{2}}\left(\frac{c_3^2}{4c_4}\right) . \tag{B.27}$$

where the only difference is: $c_9 = (c_5 b' + c_6 a')$ compared to c_8 in I.

Then, substituting I, J, H back into Eq. (B.24), one can obtain the analytical solution for numerator in second term of polarization vector as:

$$\begin{aligned} \boldsymbol{C}(\boldsymbol{p}) &= \int dV n_F(x,p)\, \partial_t \boldsymbol{\beta} = \frac{1}{T}\left(I\boldsymbol{e}_x + J\boldsymbol{e}_z + H\boldsymbol{e}_y\right) \\ &= \frac{2\pi\sqrt{\pi}C_N C_0}{\kappa T^2} e^{-p_0/T} \exp\left(\frac{c_3^2}{8c_4}\right) \exp\left(\frac{c_1^2}{4c_2^2}\right) \times \\ &\left[\frac{c_8}{c_3^2 c_4 \sqrt{c_2}} M_{-1,\frac{1}{2}}\left(\frac{c_3^2}{4c_4}\right)\boldsymbol{e}_x + \frac{c_9}{c_3^2 c_4 \sqrt{c_2}} M_{-1,\frac{1}{2}}\left(\frac{c_3^2}{4c_4}\right)\boldsymbol{e}_z + \frac{c_7 c_1}{2c_3 c_2 \sqrt{c_4 c_2}} M_{-\frac{1}{2},0}\left(\frac{c_3^2}{4c_4}\right)\boldsymbol{e}_y\right] . \end{aligned} \tag{B.28}$$

Dividing this by $A(\boldsymbol{p})$, i.e. Eq. (B.17), one gets:

$$\frac{\boldsymbol{C}(\boldsymbol{p})}{A(\boldsymbol{p})} = \frac{1}{T}\Big[\frac{c_8}{c_3\sqrt{c_4}} \frac{M_{-1,\frac{1}{2}}}{M_{-\frac{1}{2},0}}\boldsymbol{e}_x + \frac{c_9}{c_3\sqrt{c_4}} \frac{M_{-1,\frac{1}{2}}}{M_{-\frac{1}{2},0}}\boldsymbol{e}_z + \frac{c_7 c_1}{2c_2}\boldsymbol{e}_y\Big]. \tag{B.29}$$

Then, we obtain the second term of polarization vector:

$$\begin{aligned} \boldsymbol{\Pi}_2(\boldsymbol{p}) &= \frac{\hbar \boldsymbol{p}}{8m} \times \frac{\boldsymbol{C}(\boldsymbol{p})}{A(\boldsymbol{p})} \\ &= \frac{\hbar}{8mT}\left[\frac{p_y c_9}{c_3\sqrt{c_4}} \frac{M_{-1,\frac{1}{2}}}{M_{-\frac{1}{2},0}}\boldsymbol{e}_x - \frac{|p_x| c_9}{c_3\sqrt{c_4}} \frac{M_{-1,\frac{1}{2}}}{M_{-\frac{1}{2},0}}\boldsymbol{e}_y \Big(\frac{|p_x| c_7 c_1}{2c_2} - \frac{p_y c_8}{c_3\sqrt{c_4}} \frac{M_{-1,\frac{1}{2}}}{M_{-\frac{1}{2},0}}\Big)\boldsymbol{e}_z\right]. \end{aligned} \tag{B.30}$$

As we can see, and as is given also by the definition, Eq. (B.1), the second term of polarization is orthogonal to the particle momentum:

$$\boldsymbol{\Pi}_2(\boldsymbol{p}) \;\perp\; \boldsymbol{p} \;, \tag{B.31}$$

thus if we use the choice that $\boldsymbol{p}$ should be in the $[x, y]$-plane and its z-component should vanish, then the y-component of $\mathbf{\Pi}_2(\boldsymbol{p})$, should depend on p_x only.

Appendix C

Publications

Publications in Scientific Journals

1. Λ polarization in an exact rotating and expanding fluid dynamical model for peripheral heavy ion reactions,
   Y.-L. Xie, R.C. Glastad, and L.P. Csernai
   Phys. Rev. C **92**, 064901 (2015)
   10.1103/PhysRevC.92.064901

2. Erratum: Λ polarization in peripheral heavy ion collisions
   F. Becattini, L. P. Csernai, D. J. Wang, and Y. L. Xie
   Phys. Rev. C **93**, 069901(E) (2016)
   10.1103/PhysRevC.93.069901

3. Λ polarization in peripheral collisions at moderate relativistic energies
   Y.L. Xie, M. Bleicher, H. Stöcker, D.J. Wang, and L.P. Csernai
   Phys. Rev. C **94** 054907 (2016)
   10.1103/PhysRevC.95.031901

4. Global Λ polarization in high energy collisions
   Y. L. Xie, D. J. Wang, L. P. Csernai
   Phys. Rev. C **95** 031901(R) (2017)
   10.1103/PhysRevC.95.031901

5. PHYSICAL BASIS OF SUSTAINABLE DEVELOPMENT

L. P. Csernai, I. Papp, S. F. Spinnangr, Y. L. Xie

Journal of Central European Green Innovation 4 (2) pp. 39-50 (2016)

Publications in Conference Proceedings

6. Λ polarization in an exact rotating and expanding fluid dynamical model for peripheral heavy ion reactions

   Y. L. Xie

   EPJ Web of Conerences **117**, 03016 (2016)

   10.1051/epjconf/201611703016

Manuscript in preparation

7. Initial State with Shear in Peripheral Collisions

   V. K. Magas, Y. L. Xie, D. D. Strottman, and L. P. Csernai

Talks and Posters in Conferences

8. Λ Polarization in an Exact Rotating and Expanding Model for Peripheral Heavy Ion Collisions

   Poster Presentation, at the 12th International Conference on Nucleus-Nucleus Collisions (NN2015), June 21-26, 2015, Catania, Italy. (Published as 6)

9. Λ Polarization in an Exact Rotating and Expanding Model for Peripheral Heavy Ion Collisions

   Invited Talk, at the International Workshop on Exploring the Shores of Fundamental Matter: Advances around the Northern Seas (NorSAC-2015), July 29 - August 4, 2015, Bergen, Norway.

10. Λ plolarization in peripheral heavy ion collisions

    Inited Talk, at the China-Bergen Workshop, July 28 - August 3, 2016, Bergen, Norway.

11. Global Λ polarization in high energy collisions

    Invited Talk, at the International School "Relativistic Heavy Ion Collisions, Cosmology and Dark Matter, Cancer Therapy", May 15-26, 2017, Oslo, Norway.

Paper 1

Λ polarization in an exact rotating and expanding fluid dynamical model for peripheral heavy ion reactions

PHYSICAL REVIEW C **92**, 064901 (2015)

Λ polarization in an exact rotating and expanding fluid dynamical model for peripheral heavy ion reactions

Yilong Xie, Robert C. Glastad, and László P. Csernai
Institute of Physics and Technology, University of Bergen, Allegaten 55, N-5007 Bergen, Norway

(Received 28 July 2015; revised manuscript received 12 October 2015; published 2 December 2015)

We calculate the Λ polarization in an exact analytical, rotating model based on parameters extracted from a high resolution (3+1)D particle-in-cell relativistic hydrodynamics calculation. The polarization is attributed to effects from thermal vorticity and for the first time the effects of the radial and axial acceleration are also studied separately.

DOI: 10.1103/PhysRevC.92.064901 PACS number(s): 25.75.−q, 24.70.+s, 47.32.Ef

I. INTRODUCTION

In high energy peripheral heavy ion collisions there is a substantial amount of initial angular momentum directly after the Lorentz contracted nuclei penetrate each other. The formed quark gluon plasma locally equilibrates, the shear flow leads to local rotation, i.e., vorticity, and then it expands, while its rotation slows down.

Because of the finite impact parameter, the initial stages (IS) have a nonvanishing angular momentum [1,2]. For the initial stages, effective models such as the color glass condensate (CGC) or Glauber model are used. In general, we use experimental data, to construct a possible IS, at a given impact parameter for the participant nucleons, and their eccentricity. Early studies neglected effects arising from the nonvanishing angular momentum, but interest increased recently [3–6].

After many decades of refinements [7,8], hydrodynamical modeling became the best to describe the middle stages of heavy ion collisions at relativistic energies. Thus, rotation and its consequences in peripheral collisions were also studied in fluid dynamical models [9,10].

We look at polarization in effects arising from thermal vorticity in the exact rotating and expanding model [11], where we are modeling an appropriate time period of the collision [12]. Special attention was given to the collective motion, and to extract it from observables which could confirm that such descriptions are indeed plausible.

We calibrate an exact rotating model based on a (3+1)D fluid dynamical model, the relativistic particle-in-cell method (PICR), to fine tune the initial parameters of the rotating and expanding fireball [12].

In Ref. [13] the differential Hanbury Brown and Twiss (HBT) method was used to detect rotation in heavy ion collisions.

Without at least some viscosity and/or interaction one could not generate rotation from the original shear flow. On the other hand to develop instabilities or turbulence the viscosity should be small, so that the ratio of shear viscosity to entropy density η/s should be of the order of $\hbar/4\pi k_B$, which can be achieved at the phase transition between hadronic matter and QGP [14].

Thermal vorticity arises from the flow velocity field [15], and the inverse temperature field present in heavy ion collisions, and it arises mainly from a nonvanishing angular momentum in the initial stage.

Fluctuations in the transverse plane can generate significant vorticity, but in peripheral collisions the initial shear flow leads to an order of magnitude larger vorticity [15]. This vorticity may be further enhanced by the Kelvin-Helmholtz instability (KHI).

In our formalism, the dynamics of the system after local equilibration is computed using the relativistic (3+1)D fluid dynamical model PICR. This fluid dynamical (FD) computation with small viscosity shows enhanced collective rotation from an evolving KHI. In Ref. [16] a simple analytic model for this phenomenon is explored using a few material properties: the surface tension between the colliding nuclei, the viscosity, and the thickness of the flow layer. This enables a classical potential flow approximation, in which one may study the dynamics of an onsetting KHI.

A more recent calculation of the onset and effects of the KHI is performed in Ref. [12], in which the calibration of the "Exact" model takes place. Here, it is pointed out that this feature—the enhancement of rotation—is a dominant aspect of the (3+1)D fluid dynamical model, but it is also seen in UrQMD [17].

At high energy collisions, we need an initial state model, which describes the dynamics until local equilibration is reached. There are several options for describing this pre-equilibrium dynamics, using color glass condensate (CGC) fields, parton (or hadron) kinetic theory, or one-dimensional Yang-Mills field (or flux tube) models [1,2]. In the (3+1)D PICR fluid dynamical model that we use as our guidance for the FD development, this last choice is used.

It is important to mention that for peripheral collisions the initial shear and sometimes even the angular momentum are neglected, while realistic initial state models include these features [5,6,17].

From the initial shear flow, in the (3+1)D PICR fluid dynamical model the general rotation develops gradually in 1–2 fm/c time. Thus, the Exact model is applicable from this point of time on [12]. At the energies we discuss, by this time the matter is in the locally equilibrated QGP phase, and the local vorticity develops also. Because of the spin-orbit interaction the local vorticity and the spin of quarks equilibrate. The essential part of the dynamical development of flow (and other collective mechanical processes) takes place in the QGP phase, which is indicated by the constituent quark number scaling of the flow harmonics.

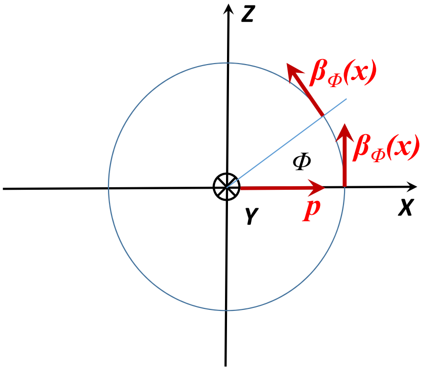

FIG. 1. (Color online) The direction of axes, as well as the momentum $\boldsymbol{p}$, and flow $\boldsymbol{\beta}$ vectors. The azimuth angle is measured from the direction of the $\boldsymbol{p}$ vector, i.e., from the x axis.

This most significant middle stage of the reaction can be modeled by the "Exact" model [11]. The model is based on a set of scaling variables,

$$(s_r, s_y) = \left(\frac{x^2+z^2}{R^2}, \frac{y^2}{Y^2}\right), \tag{1}$$

in terms of the transverse and axial coordinates, x, z, and y, and the characteristic radius R and axial length Y parameters. The scaling parameter $s = s_r + s_y$ is also introduced, being the scaling variable as it appears in the thermodynamical relations. Here we have interchanged the y and z axes to resonate with choice of axes in heavy ion collision literature, in which the reaction plane, in which the system rotates, is spanned by $\boldsymbol{e}_x$ and $\boldsymbol{e}_z$, leaving the axis of rotation to be defined by $\boldsymbol{e}_y$.

Reference [12] calibrates the parameters of the Exact model to the (3+1)D fluid dynamical model. The parameters are extracted for experiments at $\sqrt{S_{NN}} = 2.76A$ TeV with impact parameter $b = 0.7b_{\text{Max}}$ (see Figs. 1 and 2). In the (3+1)D PICR model, rotation may increase because of Kelvin-Helmholtz instability, whereas in the Exact model—and the later stages in the experiments themselves—rotation slows because of a transfer of energy to the explosively increasing radial expansion of the system. The Exact model, therefore, is suited to describe the period from the equilibration of rotation up to the freeze-out.

In [11] the solution for a flow of conserved number density, together with a constant, temperature-independent compressibility, and a velocity field is described. Hence the solutions take form, in cylindrical coordinates (r, y, ϕ), where $r = \sqrt{x^2+z^2}$ with an equation of motion, $\dot{\boldsymbol{r}}(t) = \boldsymbol{v}(\boldsymbol{r}, t)$. The Exact model assumes a linear velocity profile both in the radial r, and in the axial y directions. This leads to a flow development where a fluid element starting from a point (r_0, y_0, ϕ_0), and at a later time t reaches the point,

$$\begin{aligned} r(t) &= r_0 \frac{R(t)}{R(t_0)}, \\ y(t) &= y_0 \frac{Y(t)}{Y(t_0)}, \\ \phi(t) &= \phi_0 + \int dt\, \omega(t), \end{aligned} \tag{2}$$

showing explicitly how the solutions evolve in time, rotating and expanding fluid. These equations follow the time evolution of the scaling variables in the radial and axial directions. This is a cylindrically symmetric setup with $X(t) = Z(t)$, $\sqrt{X^2(t) + Z^2(t)} = R(t)$ and, in general, $Y(t) \neq R(t)$.

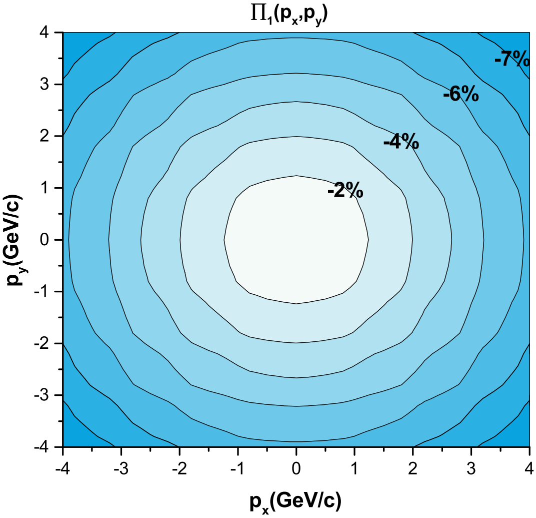

FIG. 2. (Color online) The polarization of Λ particles $\boldsymbol{\Pi}_1(\boldsymbol{p})$, in the participant center-of-mass (c.m.) frame for the first term containing the $(\nabla \times \boldsymbol{\beta})$ contribution, at time $t = 0.5$ fm/c after the equilibration of the rotation, in the Exact model. The polarization $\boldsymbol{\Pi}_1(\boldsymbol{p})$ points into the $-y$ direction and changes from -1.5% at the c.m. momentum ($p_x = p_y = 0$), to -8% in the corners, in 1% steps per contour line. The negative percentage indicates that the polarization is in the $-y$ direction. The structure is just like that of the energy weighted vorticity. Because of azimuthal symmetry of the Exact model the p_x and p_z dependencies of $\boldsymbol{\Pi}$ are the same.

We have chosen the x,z plane as our plane of rotation, with y being the axis of rotation. Our initial angular momentum, then, points in the negative y direction, with an absolute value of approximately $1.45 \times 10^4 \hbar$. In an attempt to determine new observables, we propose a search for Λ polarization. Although the polarization could be described similarly for all fermions, we chose the Λs, because it is straightforward to determine its polarization from its decay to p and π (where the p is emitted into the direction of the polarization). Actually such an experiment was already performed at RHIC, but the results were averaged for Λ emissions to all azimuths, while we predict significant polarization for particles emitted in the $\pm x$ direction in the reaction plane [18].

Our expectation is that this polarization, at least in part, will be able to account for the polarization as observed in peripheral regions in the first 10–15 fm/c following the impact in a heavy ion collision.

To evaluate the polarization in the Exact model we use the parametrization of the Exact model based on the realistic (3+1)D PICR fluid dynamical calculation [12], and use the vorticity calculated in the Exact model with these parameters in Ref. [19].

II. FREEZE-OUT AND POLARIZATION

Polarization of Λs was subject to theoretical studies before, both in $p + p$ and in heavy ion reactions. In single $p + p$ collisions forward production in small-transverse-momentum fragmentation was theoretically studied and also observed. These reactions did result in much higher polarizations up to about 30% [20].

To apply this approach to heavy ion collisions is a complex theoretical problem because several microscopic processes can contribute to polarization and these can be combined with different hadron formation mechanisms [21,22]. In Ref. [21] it was contemplated that the final heavy ion results are dependent on the hadronization mechanisms, and the effect of the decay products of the polarized hyperons on the v_2 flow harmonics v_2 were studied. Reference [22] has also studied the sensitivity of Λ production on the coalescence or recombination mechanisms of the hadron formation.

As the previous works discussed a wide variety and complexity of the microscopic description of hadronization and the resulting polarization, we have followed a simpler statistical picture, based on some simple assumptions of a dilute gas of particles, on the "Relativistic distribution function for particles with spin at local thermodynamical equilibrium" [23].

This work does not address the mechanisms of hadronization and the change of polarization during this process. It also barely discusses the equilibrium between particle polarization and local rotation in thermal equilibrium for dilute gases. Thus, this approach is primarily applicable to the final hadronic matter.

We follow the same reaction mechanism as used in all (3+1)D PICR publications since 2001. We do not assume a three-stage fluid dynamical process in the QGP phase, mixed phase, and hadronic phase because the fastest adiabatic development in the mixed phase would take 30–50 fm/c [24]. Such a long expansion time would contradict all two-particle correlation measurements showing a size and time span at FO of less than 10 fm. Furthermore it would also contradict the observed constituent quark number scaling and the observed large $\bar{\Omega}$ abundance. The only way out of these problems is supercooling in the QGP phase, followed by rapid hadronization [25,26], and almost immediate freeze-out.

Thus in the PICR fluid dynamical calculations we discuss exclusively the QGP phase, even for supercooled QGP. Based on the mechanical equilibrium, evidenced by the constituent quark number scaling, we have reason to assume that during the FD evolution there is ample time to equipartition the local rotation among all degrees of freedom in QGP from the spin-orbit interaction. As this is a strongly interacting form of matter the kinetic approximation as a dilute gas is not necessarily applicable, and the energy momentum and local angular momentum should also be carried by the fields.[1] We have to assume that the rapid hadronization maintains equipartition among all degrees of freedom carrying angular momentum. So, based on this assumption we use the approach of [23].

Actually the same applies the statistical and thermal equilibrium among (most of) the abundances of final hadron species. This can be understood based on the fact that the statistical factors are the same in rapid formation of hadrons as in thermal equilibrium.

We use the same assumptions for the Exact fluid dynamical model as we used for the (3+1)D PICR fluid dynamics. Based on the above, in the Exact model the energy weighted thermal vorticity was calculated [19]. We explored the total energy of the system and the energy of expansion, rotation, and internal energy components and their time dependence. We observed the transfer of energy from rotation to expansion, hence the rotation slows as the system expands until the freeze-out.

According to the quantum-field-theoretical approach [23], the expectation value of Λ polarization in an inverse temperature field, $\beta^\mu(x) = u^\mu(x)/T(x)$, is

$$\langle \Pi_\mu(x,p) \rangle = \frac{1}{8}\epsilon_{\mu\rho\sigma\tau}(1 - n_F)\partial^\rho \beta^\sigma(x)\frac{p^\tau}{m}, \tag{3}$$

where $\epsilon_{\mu\rho\sigma\tau}$ is the completely antisymmetric Levi-Civita symbol, n_F is the Fermi-Jüttner distribution for spin-1/2 particles [$(1 - n_F)$ is the Pauli blocking factor], and p is the Λ four-momentum. We integrate this over some volume, and ultimately over all of space, weighted by the number density, normalized by the number of particles in that volume, leaving a momentum-dependent polarization four-vector in the participant frame of reference,

$$\Pi_\mu(p) = \hbar\epsilon_{\mu\sigma\rho\tau}\frac{p^\tau}{8m}\frac{\int d\Sigma_\lambda p^\lambda n_F(x,p)(1 - n_F(x,p))\partial^\rho\beta^\sigma}{\int d\Sigma_\lambda p^\lambda n_F(x,p)}. \tag{4}$$

Note that, as opposed to electromagnetic phenomena, in which particle and antiparticle will have antialigned polarization vectors, here it is shown that Λ and $\bar{\Lambda}$ polarizations are aligned in vorticious thermal flow fields.

While the average values of polarization may be as low as 1%–2%, consistent with RHIC bounds, in some regions of momentum space we see a larger polarization, about 5% for momenta in the transverse plane and up to a momentum of 3 GeV/c. Kelvin-Helmholtz instabilities may further enhance rotation, hence the thermal vorticity, defined as

$$\varpi_{\mu\nu}(x) = \tfrac{1}{2}(\partial_\nu\beta_\mu - \partial_\mu\beta_\nu), \tag{5}$$

---

[1] If we would consider only three valence quarks in kinetic equilibrium according to [23], then the polarization of a coalesced baryon would be $\Pi_B \sim (\Pi_q)^3$, which would not be measurable.

and thereby the signal strength increases by 10%–20%. At LHC energies, there may be 5% Λ polarization from the corona effect, single nucleon-nucleon collisions occurring outside of the reaction zone of the collision itself. So attempts should be made to further the understanding of this background, and remove it from measurements to further isolate the Λ polarization as it arises from the collision itself.

The Λ polarization is determined by measuring the angular distribution of the decay protons in the Λ's rest frame. In this frame the Λ polarization is $\mathbf{\Pi}_0(\boldsymbol{p})$, which can be obtained by Lorentz boosting the polarization $\mathbf{\Pi}(\boldsymbol{p})$ from the participant frame to the Λ's rest frame [18],

$$\mathbf{\Pi}_0(\boldsymbol{p}) = \mathbf{\Pi}(p) - \frac{\boldsymbol{p}}{p^0(p^0+m)}\mathbf{\Pi}(p)\cdot\boldsymbol{p}, \tag{6}$$

where $(p^0,\boldsymbol{p})$ is the Λ's four-momentum and m its mass.

Based on this equation we see that to maximize polarization, we need to choose momenta for the Λ such that they lie in the reaction plane, hence we fix $\boldsymbol{p}$ in the positive x direction.

III. SOLUTION FOR THE Λ POLARIZATION

As the Λ is transversely polarized, $\Pi^\mu p_\mu = 0$, one can confine himself to the spatial part of Π^μ. The simplified spatial part of the polarization vector is

$$\mathbf{\Pi}(p) = \frac{\hbar\epsilon}{8m}\frac{\int dV n_F(x,p)\,(\nabla\times\boldsymbol{\beta})}{\int dV n_F(x,p)} + \frac{\hbar\boldsymbol{p}}{8m}\times\frac{\int dV n_F(x,p)\,(\partial_t\boldsymbol{\beta}+\nabla\beta^0)}{\int dV n_F(x,p)}, \tag{7}$$

where $n_F(x,p)$ is the phase space distribution of the Λs. In a previous calculation [18], the p dependence of n_F, was considered negligible in the integral and the time derivative and gradient terms were also assumed to be smaller. The present calculation shows that in general these terms are not negligible and which terms are dominant depends on the particular conditions.

We adopt the parametrization of the model from Ref. [19], with the initial conditions $R_0 = 2.5$ fm, $Y_0 = 4.0$ fm, $\dot{R}_0 = 0.20$ c, $\dot{Y}_0 = 0.25c$, $\omega_0 = 0.1$ c/fm, $\kappa = 3/2$, $T_0 = 300$ MeV. For this configuration $E_{\text{tot}} = 576$ MeV/nucl.

A. The denominator

We first perform the integral in the denominator:

$$A(p) \equiv \int dV\, n_F = \int_0^R r\,dr \int_{-Y}^{+Y} dy \int_0^{2\pi} d\phi\, n_F(x,p). \tag{8}$$

According to Eq. (3) in Ref. [19] in terms of the scaling variable s, we have

$$n = n_0\frac{V_0}{V}\nu(s), \tag{9}$$

$$\nu(s) = \frac{1}{\tau(s)}\exp\left(-\frac{1}{2}\int_0^s \frac{du}{\tau(u)}\right) = 1\times\exp\left(-\frac{1}{2}\int_0^s du\right), \tag{10}$$

where the simplifying choice of $\tau(s) = 1$ is used in the last step. Therefore,

$$n(s) = n_0\frac{V_0}{V}e^{-\frac{1}{2}s}. \tag{11}$$

The EoS is assumed to be $\epsilon(s) = \kappa T(t)n(s)$ and the energy density $\epsilon(s)$ is calculated as in Eq. (29) in Ref. [19], therefore,

$$n(s) = \frac{\epsilon}{\kappa T(t)} = \frac{C_N}{\kappa T}e^{-\frac{s_y}{2}}e^{-\frac{s_\rho}{2}}, \tag{12}$$

where $C_N = \kappa n_0 T_0(\frac{V_0}{V})^{1+1/\kappa}$.

From Ref. [18], the Fermi-Jüttner distribution is

$$n_F(x,p) = \frac{1}{e^{p^\mu\beta_\mu-\xi}+1} \approx \frac{1}{e^{p^\mu\beta_\mu-\xi}} = \frac{e^{\mu/T}}{e^{p^\mu\beta_\mu}}, \tag{13}$$

where the $\xi = \mu/T$, and μ is the chemical potential. The thermal flow velocity, $\beta^\mu(x) \equiv u^\mu(x)/T$, is different at different space-time points x.

The invariant scalar density for the Jünttner distribution is

$$n = \frac{4\pi m^2 K_2(m/T)}{(2\pi\hbar)^3}e^{\mu/T} = \frac{e^{\mu/T}}{C_0}, \tag{14}$$

where the $C_0^{-1} = 4\pi m^2 T K_2(m/T)/(2\pi\hbar)^3$. With C_0 and $n(s) = n$, the Fermi-Jüttner distribution can be written as

$$n_F(x,p) = \frac{e^{\mu/T}}{e^{p^\mu\beta_\mu}} = \frac{C_0 n(s)}{e^{p^\mu\beta_\mu}}. \tag{15}$$

Now we introduce cylindrical coordinates for the location in the configuration place $x = (r,y,\phi)$, and using the scaling expansion model [11,12] with the scaling variables s ,s_r ,s_y. Now, substituting Eqs. (12) and (15) into the denominator of $\Pi(p)$, and parametrizing the range of integrations as in [19] one obtains

$$A(p) = \frac{C_N C_0}{\kappa T}\int_{-aY}^{aY} dy\,\exp\left(-\frac{y^2}{2Y^2}\right)\int_0^{bR} r\,dr\,\exp\left(-\frac{r^2}{2R^2}\right) \times\int_0^{2\pi} d\phi\, e^{-p^\mu\beta_\mu}. \tag{16}$$

The scalar product in cylindrical coordinates takes the form $p^\mu\beta_\mu = (p^0,\boldsymbol{p})(\beta_0,\boldsymbol{\beta}) = p^0\beta_0 - \boldsymbol{p}\cdot\boldsymbol{\beta} = p^0\beta_0 - p_r\beta_r - p_y\beta_y - p_\phi\beta_\phi$.

In our integral the p^μ is given or "fixed" as the argument of $\mathbf{\Pi}(p)$, while the $\boldsymbol{\beta} = \boldsymbol{\beta}(x)$ is changing. The integration with respect to ϕ starts from the direction of the $\boldsymbol{p}$ vector. According to the Eq. (5) in [19],

$\boldsymbol{v} = v_r\boldsymbol{e}_r + v_\phi\boldsymbol{e}_\phi + v_y\boldsymbol{e}_y = \frac{\dot{R}}{R}r\boldsymbol{e}_r + \omega r\boldsymbol{e}_\phi + \frac{\dot{Y}}{Y}y\boldsymbol{e}_y$, and $\boldsymbol{\beta} = u^i/T = \gamma\boldsymbol{v}/T$. Thus in the integral for ϕ we exploit the fact that in the Exact model the radial r, and axial y components of the thermal velocity $\boldsymbol{\beta}$ do not depend on ϕ, while the tangential component does not depend on y, i.e., $\beta_\phi = \gamma r\,\omega/T$, but its direction is changing with respect to the direction of $\boldsymbol{p}$. As the integral is over the whole 2π angle we can start it at any point of ϕ, so we start it from the externally given $\boldsymbol{p}$ direction. Consequently, with this choice of the x axis, $\boldsymbol{p} = (p_r,p_y,0)$, and $p_z = p_\phi = 0$. In this azimuthally symmetric, exact model it is sufficient to calculate $\Pi(\boldsymbol{p})$ for one direction of $\boldsymbol{p}$ in the $[x,z]$ plane.

The direction of the thermal flow velocity $\boldsymbol{\beta}$ is tangential to the direction ϕ, i.e., it points to the $\boldsymbol{e}_{\phi+\pi/2}$ direction. Thus the scalar product is

$$\boldsymbol{p}\cdot\boldsymbol{\beta}(r,y,\phi) = |p_x|\beta_r\cos(\phi) + p_y\beta_y + |p_x|\beta_\phi\cos\left(\phi+\frac{\pi}{2}\right),$$

where ϕ is the azimuth angle of the position around the y rotation axis, counted starting from the x axis. See Fig. 1.

So, inserting the last expression for $p^\mu\beta_\mu$ into the last term of the integral Eq. (16), the integral with respect to ϕ will take the form,

$$\int_0^{2\pi} d\phi\, e^{-p^\mu\beta_\mu} = \int_{-\pi}^{\pi} d\phi\, e^{a\cos(\phi)-b\sin(\phi)} = 2\pi I_0(\sqrt{a^2+b^2}), \tag{17}$$

where $a = |p_x|\beta_r = |p_x|\gamma\dot{R}r/TR$ and $b = |p_x|\beta_\phi = |p_x|\gamma r\,\omega/T$, and we used integral No. 3.338(4) in [27]. If we define

$$c_3 = \sqrt{\left(\frac{p_x\gamma\dot{R}}{TR}\right)^2 + \left(\frac{p_x\gamma\,\omega}{T}\right)^2} = \frac{|p_x|\gamma}{T}\sqrt{(\dot{R}/R)^2+\omega^2},$$

then $\sqrt{a^2+b^2} = c_3 r$, and

$$\int_0^{2\pi} d\phi\, e^{-p^\mu\beta_\mu} = e^{-\gamma p^0/T}\, e^{p_y\beta_y} \times 2\pi I_0(c_3 r). \tag{18}$$

Now, substituting this back into Eq. (16),

$$\begin{aligned} A(p) &= \int dV\, n_F(p,s) \\ &= \frac{C_N C_0}{\kappa T}\int_{-aY}^{aY} dr_y \int_0^{bR} r\,dr\, \exp\left(-\frac{y^2}{2Y^2} - \frac{r^2}{2R^2}\right) \\ &\quad \times e^{-\gamma p^0/T}\, e^{p_y\beta_y} 2\pi I_0(c_3 r). \end{aligned} \tag{19}$$

Now we may use the same simplifying nonrelativistic assumption as in Eq. (5) of Ref. [19], i.e., we approximate u^μ by v^μ as $\boldsymbol{v} = v_r\boldsymbol{e}_r + v_y\boldsymbol{e}_y + v_\phi\boldsymbol{e}_\phi = \frac{\dot{R}}{R}r\boldsymbol{e}_r + \frac{\dot{Y}}{Y}y\boldsymbol{e}_y + \omega r\boldsymbol{e}_\phi$, and thus $\gamma = 1$. It follows, then,

$$\begin{aligned} A(p) &= \int dV\, n_F(p,s) \\ &= \frac{C_N C_0}{\kappa T} 2\pi e^{-p^0/T} \int_{-aY}^{aY} \exp(c_1 y - c_2 y^2) dy \\ &\quad \times \int_0^{bR} r\, I_0(c_3 r)\exp(-c_4 r^2) dr, \end{aligned} \tag{20}$$

where $c_1 = p_y\dot{Y}/(YT)$, $c_2 = 1/(2Y^2)$, $c_4 = 1/(2R^2)$ are constants.

Now we assume an infinite system with scaling Gaussian density profile, so that the integrals are evaluated up to infinity, i.e., the parameters $a = \infty$, $b = \infty$. Thus, the y component integration in Eq. (20) is calculated as

$$\int_{-\infty}^{+\infty} e^{c_1 y - c_2 y^2} dy = \sqrt{\frac{\pi}{c_2}}\exp\left(\frac{c_1^2}{4c_2^2}\right), \tag{21}$$

where we used the integral formula No. 2.33(1) in [27], and $\operatorname{erf}(+\infty) = 1$, $\operatorname{erf}(-\infty) = -1$.

For the integration of the r component,

$$\begin{aligned} &\int_0^{+\infty} r\, I_0(c_3 r)\, e^{-c_4 r^2} dr \\ &= \frac{1}{c_3\sqrt{c_4}}\exp\left(\frac{c_3^2}{8c_4}\right) M_{-\frac{1}{2},0}\left(\frac{c_3^2}{4c_4}\right), \end{aligned} \tag{22}$$

where the $M_{-\mu,\nu}(z)$ is the so-called "Whittaker Function," No. 6.643(2) in [27].

Now, we obtain the final form of Eq. (21):

$$\begin{aligned} A(p) = {}& \frac{2\pi\sqrt{\pi}}{\kappa T}\frac{C_N C_0}{c_3\sqrt{c_2 c_4}} e^{-p^0/T}\exp\left(\frac{c_1^2}{4c_2^2}\right) \\ &\times \exp\left(\frac{c_3^2}{8c_4}\right) M_{-\frac{1}{2},0}\left(\frac{c_3^2}{4c_4}\right). \end{aligned} \tag{23}$$

However, in the relativistic case, the integrations with respect to y and r cannot be performed analytically, because of the presence of the factor $\gamma = 1/\sqrt{1 - v_r^2 - v_y^2 - v_\phi^2}$.

B. The numerator

Reference [19] calculates the energy weighted vorticity, which is azimuthally symmetric, i.e., independent of the azimuthal angle ϕ. In the definition of the polarization, Eq. (7), we have $p^0\, n_F(p,x) = \epsilon\, n_F(p,x)$ for Λs with momentum p. In [19], however, the energy weighting is performed with the total energy density of the fluid $E_{\text{tot}} = E_{\text{int}} + E_{\text{kin}}$, which in general is not the same as $\epsilon\, n_F(p,x)$. On the other hand the bare vorticity is just a constant in the nonrelativistic Exact model, while the EoS may be more general and it may lead to more involved $R(t)$ and $Y(t)$ dependence than the ideal Jüttner gas approximation would allow.

Thus we use the direct, nonrelativistic vorticity values $\omega(t)$ from Ref. [19], and not the presented energy weighted vorticity, i.e.,

$$\nabla\times\boldsymbol{\beta} = -2\,\omega(t)\,\boldsymbol{e}_y/T(t), \tag{24}$$

so that the thermal vorticity has only the y-directed component in the Exact model. With the model parameters mentioned above (beginning of Sec. III), the thermal vorticity is $\hbar(\nabla\times\boldsymbol{\beta}) = -0.13$ at $t = 0.5$ fm/c, and it decreases very slowly with time, about 1%–2% per 1 fm/c. This constant vorticity will make the numerator simple:

$$B(p) \equiv \int dV\, n_F(\nabla\times\beta) = \frac{-2\omega\boldsymbol{e}_y}{T}\times A(p). \tag{25}$$

Therefore, the first term of polarization vector, i.e., Eq. (7) will be

$$\boldsymbol{\Pi}_1(p) = -\frac{\hbar\epsilon}{8m}\frac{\int dV n_F(x,p)\,(\nabla\times\boldsymbol{\beta})}{\int dV n_F(x,p)} = \frac{\hbar\epsilon\omega}{4mT}\boldsymbol{e}_y, \tag{26}$$

which means the polarization vector arising from the vorticity $\boldsymbol{\Pi}_1(p)$ in the Exact rotation model is a constant (although time dependent), and parallel to the y axis.

One may add the freeze-out (FO) probability to the integral. According to the Ref. [28], the FO probability is $w_s = (p_\mu\,\hat{\sigma}_s^\mu)(\boldsymbol{p}\cdot\boldsymbol{u}(x))$, where the approximation is used that the FO direction $\hat{\sigma}_s^{\mu}$ is parallel to the flow velocity $\boldsymbol{u}(x) = \gamma \boldsymbol{v}(x)$. In the first term of the numerator, which depends on the constant y-directed vorticity this FO probability influences the numerator and denominator the same way, so the effect of the two integrals cancel each other in the FO probability also.

C. The second term

The numerator in the second term of polarization vector reads

$$\boldsymbol{C}(\boldsymbol{p}) \equiv \int dV n_F(x,p)\,(\partial_t \boldsymbol{\beta} + \nabla \beta^0). \tag{27}$$

If, in the nonrelativistic limit, $\gamma = 1$ is assumed, then $\nabla\beta^0 = 0$ and $\partial_t \beta = \partial_t(\boldsymbol{v}/T)$, so we have to evaluate only the first term of the sum in the integrand. According to Refs. [19,29], the time derivatives of velocity are

$$\begin{aligned}
\partial_t v_r &= \left[\left(\frac{\ddot{R}}{R} - \frac{\dot{R}^2}{R^2}\right) - \omega^2\right] r \equiv c_5 r,\\
\partial_t v_\phi &= \left(\dot{\omega} + 2\frac{\dot{R}}{R}\omega\right) r \equiv c_6 r,\\
\partial_t v_y &= \left[\frac{\ddot{Y}}{Y} - \frac{\dot{Y}^2}{Y^2}\right] y \equiv c_7 y,
\end{aligned} \tag{28}$$

where $c_5 = (\ddot{R}/R - \dot{R}^2/R^2 - \omega^2)$, $c_6 = (\dot{\omega} + 2(\dot{R}/R)\omega)$, and $c_7 = (\ddot{Y}/Y - \dot{Y}^2/Y^2)$.

Therefore,

$$\partial_t \boldsymbol{\beta} = (c_5 r \boldsymbol{e}_r + c_6 r \boldsymbol{e}_\phi + c_7 y \boldsymbol{e}_y)/T,$$

provides the time components of the vorticity in the three spatial directions. Here, as the model is symmetric, $\partial_t \beta_y$ vanishes, and with the model parameters mentioned above (Sec. III), at $t = 0.5$ fm/c and $r = 1$ fm $\frac{\hbar}{c}\partial_t \beta_r = 0.024$ and $\frac{\hbar}{c}\partial_t \beta_\phi = 0.009$. Both these vorticity components decrease slowly with time by about 0.0005 in 1 fm/c.

Equation (27) is a volume integral of a vectorial quantity, which is not convenient to perform in cylindrical coordinates. So we transform it into Cartesian coordinates: $\boldsymbol{e}_r = \cos\phi\, \boldsymbol{e}_x + \sin\phi\, \boldsymbol{e}_z$, $\boldsymbol{e}_\phi = -\sin\phi\, \boldsymbol{e}_x + \cos\phi\, \boldsymbol{e}_z$. Therefore, $T \;\; \partial_t \boldsymbol{\beta} = (c_5 \cos\phi - c_6 \sin\phi) r\, \boldsymbol{e}_x + (c_5 \sin\phi + c_6 \cos\phi) r\, \boldsymbol{e}_z + c_7 y\, \boldsymbol{e}_y$.

The integral of Eq. (27) can be expanded as

$$\begin{aligned}
\boldsymbol{C}(\boldsymbol{p}) &= \int dV n_F(x,p)\, \partial_t \boldsymbol{\beta}\\
&= \frac{C_N C_0}{\kappa T} e^{-p_0/T} \iiint r dr d\phi dy \, \exp(c_1 y - c_2 y^2)\\
&\quad \times \exp(a\cos\phi - b\sin\phi - c_4 r^2)\partial_t \boldsymbol{\beta},
\end{aligned} \tag{29}$$

where a and b are defined after Eq. (17).

It is convenient to define an integrating operator $\bar{A}$ as

$$\begin{aligned}
\bar{A} &= \int dV n_F(x,p) \,\times\\
&= \iiint r\, dr\, d\phi\, dy\, e^{c_1 y - c_2 y^2} e^{a\cos\phi - b\cos\phi - c_4 r^2} \,\times\,,
\end{aligned}$$

and then Eq. (29) will be

$$\boldsymbol{C}(\boldsymbol{p}) = \bar{A}\partial_t \boldsymbol{\beta} \equiv \frac{1}{T}(I\boldsymbol{e}_x + J\boldsymbol{e}_z + H\boldsymbol{e}_y), \tag{30}$$

where we defined

$$\begin{aligned}
I &\equiv \bar{A}(c_5\cos\phi - c_6\sin\phi) r,\\
J &\equiv \bar{A}(c_5\sin\phi + c_6\cos\phi) r,\\
H &\equiv \bar{A} c_7 y.
\end{aligned}$$

Using the integral formula No. 2.33(6) of [27] the function H becomes

$$\begin{aligned}
H = {}& \frac{2\pi\sqrt{\pi} C_N C_0}{\kappa T} e^{-p_0/T} \frac{c_7 c_1}{2 c_3 c_2 \sqrt{c_4 c_2}}\\
& \times \exp\left(\frac{c_3^2}{8c_4}\right) \exp\left(\frac{c_1^2}{4c_2^2}\right) M_{-\frac{1}{2},0}\left(\frac{c_3^2}{4c_4}\right).
\end{aligned} \tag{31}$$

The function I can be expanded as a function of integrals over ϕ, r, and y. The integral over ϕ brings in the Bessel function, $2\pi c_8 I_1(c_3 r)/c_3$ [see No. 3.937 (1) and (2) of [27]], where $c_8 = (c_5 a' - c_6 b')$, $a' = a/r = |p_x|\dot{R}/TR$, and $b' = b/r = |p_x|\omega/T$. Subsequently, the integral with respect to r brings in the "Whittaker Function" and then the final form of I after performing the separable integration with respect to y leads to

$$\begin{aligned}
I = {}& \frac{2\pi\sqrt{\pi} C_N C_0}{\kappa T} e^{-p_0/T} \frac{c_8}{c_3^2 c_4 \sqrt{c_2}}\\
& \times \exp\left(\frac{c_3^2}{8c_4}\right) \exp\left(\frac{c_1^2}{4c_2^2}\right) M_{-1,\frac{1}{2}}\left(\frac{c_3^2}{4c_4}\right).
\end{aligned} \tag{32}$$

Evaluating the integral J is similar to I:

$$\begin{aligned}
J = {}& \frac{2\pi\sqrt{\pi} C_N C_0}{\kappa T} e^{-p_0/T} \frac{c_9}{c_3^2 c_4 \sqrt{c_2}}\\
& \times \exp\left(\frac{c_3^2}{8c_4}\right) \exp\left(\frac{c_1^2}{4c_2^2}\right) M_{-1,\frac{1}{2}}\left(\frac{c_3^2}{4c_4}\right),
\end{aligned} \tag{33}$$

where the only difference is $c_9 = (c_5 b' + c_6 a')$ compared to c_8 in I.

Then, substituting I, J, H back into Eq. (30), one can obtain the analytical solution for numerator in the second term of the polarization vector as

$$\begin{aligned}
\boldsymbol{C}(\boldsymbol{p}) &= \int dV n_F(x,p)\, \partial_t \boldsymbol{\beta} = \frac{1}{T}(I\boldsymbol{e}_x + J\boldsymbol{e}_z + H\boldsymbol{e}_y)\\
&= \frac{2\pi\sqrt{\pi} C_N C_0}{\kappa T^2} e^{-p_0/T} \exp\left(\frac{c_3^2}{8c_4}\right) \exp\left(\frac{c_1^2}{4c_2^2}\right)\\
&\quad \times \left[\frac{c_8}{c_3^2 c_4 \sqrt{c_2}} M_{-1,\frac{1}{2}}\left(\frac{c_3^2}{4c_4}\right)\boldsymbol{e}_x\right.\\
&\quad + \frac{c_9}{c_3^2 c_4 \sqrt{c_2}} M_{-1,\frac{1}{2}}\left(\frac{c_3^2}{4c_4}\right)\boldsymbol{e}_z\\
&\quad \left. + \frac{c_7 c_1}{2 c_3 c_2 \sqrt{c_4 c_2}} M_{-\frac{1}{2},0}\left(\frac{c_3^2}{4c_4}\right)\boldsymbol{e}_y\right].
\end{aligned} \tag{34}$$

Dividing this by $A(\boldsymbol{p})$, i.e., Eq. (23), one gets

$$\frac{\boldsymbol{C}(\boldsymbol{p})}{A(\boldsymbol{p})}=\frac{1}{T}\left[\frac{c_8}{c_3\sqrt{c_4}}\frac{M_{-1,\frac{1}{2}}}{M_{-\frac{1}{2},0}}\boldsymbol{e}_x+\frac{c_9}{c_3\sqrt{c_4}}\frac{M_{-1,\frac{1}{2}}}{M_{-\frac{1}{2},0}}\boldsymbol{e}_z+\frac{c_7c_1}{2c_2}\boldsymbol{e}_y\right]. \tag{35}$$

Then, we obtain the second term of the polarization vector:

$$\begin{aligned}\boldsymbol{\Pi}_2(\boldsymbol{p}) &= \frac{\hbar\boldsymbol{p}}{8m}\times\frac{\boldsymbol{C}(\boldsymbol{p})}{A(\boldsymbol{p})}\\ &= \frac{\hbar}{8mT}\left[\frac{p_yc_9}{c_3\sqrt{c_4}}\frac{M_{-1,\frac{1}{2}}}{M_{-\frac{1}{2},0}}\boldsymbol{e}_x-\frac{|p_x|c_9}{c_3\sqrt{c_4}}\frac{M_{-1,\frac{1}{2}}}{M_{-\frac{1}{2},0}}\boldsymbol{e}_y\right.\\ &\quad\left.+\left(\frac{|p_x|c_7c_1}{2c_2}-\frac{p_yc_8}{c_3\sqrt{c_4}}\frac{M_{-1,\frac{1}{2}}}{M_{-\frac{1}{2},0}}\right)\boldsymbol{e}_z\right].\end{aligned} \tag{36}$$

As we can see, and as is given also by the definition, Eq. (7), the second term of polarization is orthogonal to the particle momentum:

$$\boldsymbol{\Pi}_2(\boldsymbol{p})\ \perp\ \boldsymbol{p}, \tag{37}$$

thus if we use the choice that $\boldsymbol{p}$ should be in the $[x,y]$ plane and its z component should vanish, then the y component of $\boldsymbol{\Pi}_2(\boldsymbol{p})$, should depend on p_x only (see Fig. 5).

IV. THE FREEZE-OUT STAGE

The fluid dynamical model is in principle not adequate to describe the final, post-freeze-out (FO) particle distributions, the abundance of the particle species, and also their polarization. This is so because the post-freeze-out distributions must not be in local thermal equilibrium and must not have interactions among the final emitted particles. Furthermore, the emitted particles should not move back into the interacting zone, i.e., towards the pre-FO side of the FO hypersurface. How to handle the freeze-out is described in great detail in [30]. It indicates two ways to handle this process: (i) Consider the post-FO matter as if it has an equation of state (EoS). This is only possible if the post FO EoS is that of a noninteracting ideal gas and the FO hypersurface is timelike. (ii) The other approach is that the post-FO matter is described by a dynamical model with weak and rapidly decreasing interaction, like UrQMD or PACIAE, matched to the QGP fluid on the FO hypersurface. The change at crossing this hypersurface is in general significant, as the pre-FO matter is strongly interacting, supercooled QGP, while the post-FO matter is weakly interacting and has different (usually fewer) degrees of freedom in both situations. The FO across the hypersurface is stronger if the latent heat of the transition is larger.

The precise way to perform this transition is described in [30]. This method is demonstrated in several earlier fluid dynamical model calculations (also using the PICR method) for precision calculations of flow harmonics.

As mentioned in the introduction, at high energies (RHIC and LHC) the constituent quark number scaling and the large strangeness abundance clearly indicate a supercooling and rapid hadronization. Furthermore at these energies the transition is in the crossover domain of the EoS, thus the expected changes are smaller, and the major part of the FO hypersurface is timelike, which allows one to use ideal gas post-FO distributions, as we do it here using the method of [23]. These are the conditions which make the changes in mechanical parameters (e.g., $\boldsymbol{v}$) small at freeze-out while the temperature changes are larger [30].

Thus, just in the case of constituent quark number scaling, we assume that other mechanical processes like mechanical polarization will not significantly change at freeze-out at RHIC and LHC energies. This conclusion is restricted to local thermal and flow equilibrium, and should not apply to some of the microscopic processes, which dominate $p+p$ reactions.

Also, in the case of freeze-out through spacelike FO hypersurfaces, the mechanical parameters change significantly, the post-FO distribution is far from a thermal distribution (it is a cut-Jüttner or canceling-Jüttner distribution), and thus the conditions of [23] that we use, are not satisfied.

In this connection we may mention that in earlier related publications, previous experimental Λ polarization measurements, which were negative, were discussed. It was pointed out that polarization as measured was averaged for all Λ particle directions. Here, as well as in the previously detailed PICR fluid dynamical calculations, it was emphasized that polarization should be measured after finding event by event the reaction plane and the center of mass of the system. Significant polarization can only be expected for particles emitted in selected directions.

Preliminary experimental polarization studies in the RHIC Beam Energy Scan program along these lines are promising [31], and may lead soon to positive quantitative results. At this point in time the present relatively simpler FO treatment of the model calculations with constant time FO are sufficient, and can be refined when quantitative experimental data are available.

A. Conclusion

Finally, adding Eqs. (36) and (26) we get the analytical solution for Λ polarization in the Exact model:

$$\begin{aligned}\boldsymbol{\Pi}(p) = \frac{\hbar}{8mT}&\left[\frac{p_yc_9}{c_3\sqrt{c_4}}\frac{M_{-1,\frac{1}{2}}}{M_{-\frac{1}{2},0}}\boldsymbol{e}_x+\left(2\epsilon\omega-\frac{|p_x|c_9}{c_3\sqrt{c_4}}\right.\right.\\ &\left.\left.\times\frac{M_{-1,\frac{1}{2}}}{M_{-\frac{1}{2},0}}\right)\boldsymbol{e}_y+\left(\frac{|p_x|c_7c_1}{2c_2}-\frac{p_yc_8}{c_3\sqrt{c_4}}\frac{M_{-1,\frac{1}{2}}}{M_{-\frac{1}{2},0}}\right)\boldsymbol{e}_z\right].\end{aligned} \tag{38}$$

Notice that Eq. (38) is the analytical solution in the nonrelativistic limit. The "Whittaker Function," $M_{\mu,\nu}(z)$, is the confluent hypergeometric function. For the relativistic case, the integrations of the Λ-polarization vector cannot be performed analytically, because of the presence of $\gamma = 1/\sqrt{1-v_r^2-v_y^2-v_\phi^2}$, which will make the integrations more involved. Thus, a numerical solution for the Λ polarization would be needed.

The effect of vorticity is shown in Fig. 2. The nonrelativistic Exact model can handle reactions with modest energy and modest rotation, so the overall vorticity and the resulting polarization is not too large. Furthermore, the rotation and

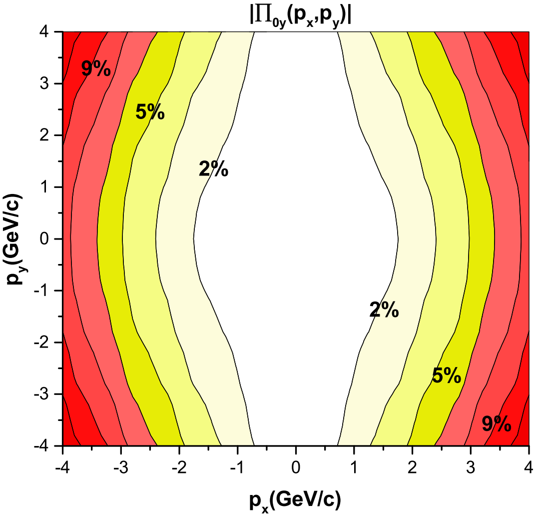

FIG. 3. (Color online) The absolute value of Λ polarization, $\mathbf{\Pi}_2(\boldsymbol{p})$, in the participant center-of-mass (c.m.) frame for the second term containing the $(\partial_t \boldsymbol{\beta})$ contribution, at time $t = 0.5$ fm/c after the equilibration of the rotation, in the Exact model. The polarization changes from zero at the c.m. momentum $(p_x = p_y = 0)$, up to 20% in the corners at $p_x = -4\text{GeV/c}$, in 2.5% steps per contour line. In the corners at $p_x = 4\text{GeV/c}$, the polarization is 12%. This second term is orthogonal to $\boldsymbol{p}$, and it is smaller, especially at c.m. momenta, where it is negligible. This term arises from the expansion, which is increasing rapidly in the Exact model with time and also increases with the radius. At large radius the larger expansion leads to larger momenta. The structure of the second component of polarization arises from the asymmetries of the different components of $\mathbf{\Pi}_2(\boldsymbol{p})$.

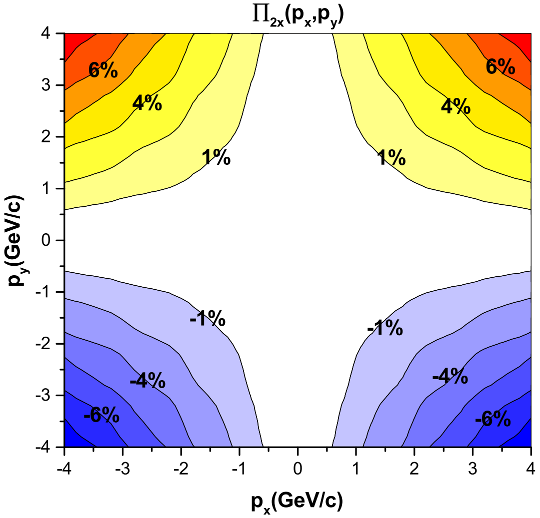

FIG. 4. (Color online) The x component of the Λ polarization $\mathbf{\Pi}_{2x}(\boldsymbol{p})$ in the participant center-of-mass (c.m.) frame for the second term containing the $(\partial_t \boldsymbol{\beta})$ contribution, at time $t = 0.5$ fm/c after the equilibration of the rotation, in the Exact model. The polarization vanishes at the c.m. momentum $(p_x = p_y = 0)$, and changes from zero up or down to ±8% in the corners, in 1% steps per contour line. This term arises from the expansion, which is increasing rapidly in the Exact model with time and also increases with the radius. At large radius the larger expansion leads to larger momenta.

vorticity decrease with time while the radial and axial expansion increases. This expansion leads to the second term of polarization $\mathbf{\Pi}_2$, which depends on $\partial_t \boldsymbol{\beta}$ (while the $\nabla \beta^0$ terms vanishes in the nonrelativistic approximation). Because of the simplicity of the Exact model, the vorticity arising from the shear flow of the peripheral initial state is constant in space and depends on the time only. However, because of the construction of thermal vorticity, both the angular momentum and the temperature in the denominator decrease with time, thus $\nabla \times \boldsymbol{\beta}$ is hardly decreasing with the time, and it has a significant value, -0.13, in natural units. At the same time in this model the time-dependent vorticity is smaller by almost an order of magnitude. The time-dependent vorticity components also decrease faster than the one originating from the initial shear flow.

Nevertheless, the second term in the polarization is of comparable magnitude to the term arising from local vorticity; see Fig. 3.

The presented plots are such that p_x points into the direction of the observed Λ particle, while the p_y is the axis direction. All results should be either symmetric or antisymmetric for a $\pm p_y$ change. On the other hand reversing the p_x axis must not change the data, as the x axis is chosen to be the direction of the argument of $\mathbf{\Pi}(\boldsymbol{p})$, which must be azimuthally symmetric in the $[x,y]$ plane.

The polarization arising from the dynamics of the radial and spherical expansion $\mathbf{\Pi}_2$ was not discussed before in the literature, as the dominance of the vorticity effect was anticipated and studied up to now. The $\mathbf{\Pi}_2$ plots in Figs. 3, 4, 5, and 7 show the components of the polarization arising from the dynamics of the spherical expansion. The most interesting y component arises from the x component of the momentum and the z component of the thermal velocity change $\dot{\beta}_z$ (Fig. 5).

Now if we study the axis directed components, this is given by $\Pi_y = \Pi_{1y} + \Pi_{2y}$. Both these terms have a negative maxima of the same magnitude (-8%), at the corners $p_x, p_y = \pm 4\text{GeV/c}$, thus these terms add up constructively and result in Λ-particle polarizations reaching -16% at high momenta. At small momenta the polarization is still the same sign but has a reduced value of the order of 1.5% arising from the vorticity (Fig. 6).

In this Exact model the x and z components of the polarization arise only from the second term $\mathbf{\Pi}_2(\boldsymbol{p})$. The x component is reaching ±8%, while the z component is smaller; it reaches about ±3%. These both are asymmetric for $\pm p_y$ change, and show an opposite symmetry. The x component is proportional to p_y and the dynamics of radial expansion. Thus it follows the signature of p_y (Fig. 4). The z component is proportional to p_y and the dynamics of radial expansion, thus it follows the signature of p_y (Fig. 7). The z component

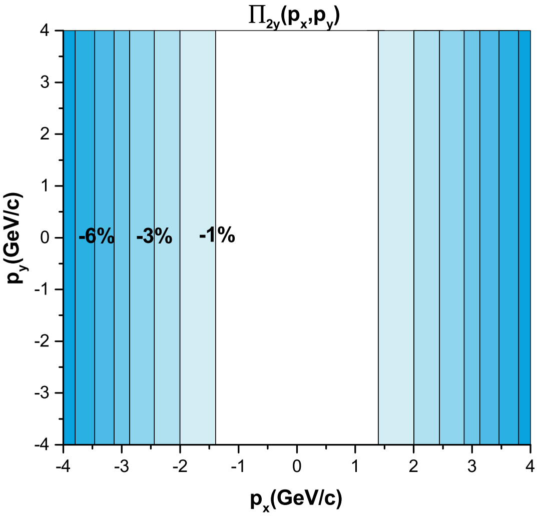

FIG. 5. (Color online) The y component of Λ polarization $\mathbf{\Pi}_2(\boldsymbol{p})$, in the participant center-of-mass (c.m.) frame for the first term containing the $(\partial_t \boldsymbol{\beta})$ contribution, at time $t = 0.5$ fm/c after the equilibration of the rotation, in the Exact model. The polarization changes from zero in the middle to -8% at $p_x = \pm 4$ GeV/c, in 1% steps per contour line. This y-component points into the axis direction just as the first term $\mathbf{\Pi}_1$, thus these two are additive. The y component of $\mathbf{\Pi}_2(\boldsymbol{p})$ does not depend on p_y, as shown in Eq. (36).

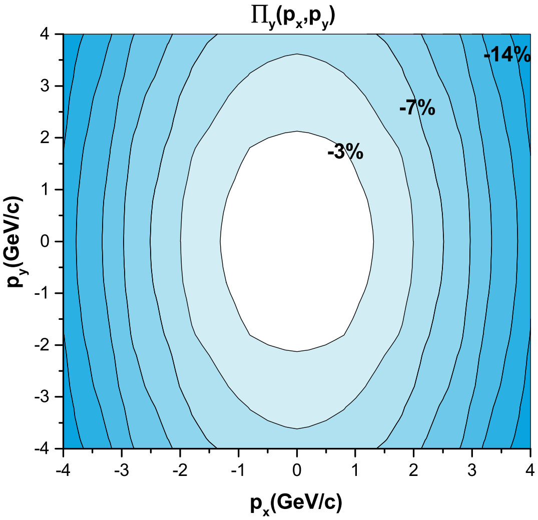

FIG. 6. (Color online) The y component of Λ polarization $\mathbf{\Pi}(\boldsymbol{p})$ in the participant center-of-mass (c.m.) frame for the second term containing the $(\partial_t \boldsymbol{\beta})$ contribution at time $t = 0.5$ fm/c after the equilibration of the rotation in the Exact model. The polarization is -1.5% at the c.m. momentum $(p_x = p_y = 0)$, it is -16% in the corners. The change is in steps of 2% per contour line.

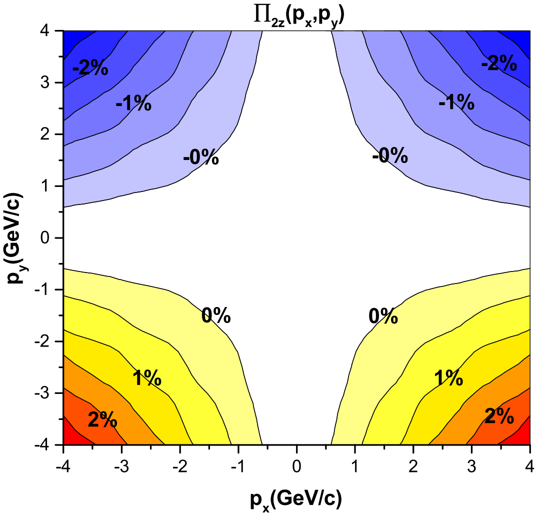

FIG. 7. (Color online) The z component of Λ polarization $\mathbf{\Pi}_2(\boldsymbol{p})$ in the participant center-of-mass (c.m.) frame for the second term containing the $(\partial_t \boldsymbol{\beta})$ contribution, at time $t = 0.5$ fm/c after the equilibration of the rotation, in the Exact model. The polarization vanishes at the c.m. momentum $(p_x = p_y = 0)$; it is $\pm 3\%$ in the corners. The change is in steps of 0.5% per contour line. The corners at $p_y = -4$ GeV/c are positive while at $p_y = 4$ GeV/c are negative.

is proportional to $p_x \dot{\beta}_y$ and inversely proportional to $p_y \dot{\beta}_x$ (Fig. 7). These two effects compensate each other so the maxima of the polarization are smaller and the symmetry is opposite to that of the x component. This term is sensitive to the balance between the axial expansion and the radial expansion in the model.

The Λ polarization is measured via the angular distribution of the decay protons in the Λ's rest frame, as shown in Eq. (6). The resulting distribution is shown in Fig. 8. This new study indicates that the dynamics of the expansion may lead to non-negligible contribution to the observable polarization. The structure of $\Pi_{0y}(\boldsymbol{p})$ is similar to the one obtained in Ref. [18], but here the contribution of the "second" $\partial_t \boldsymbol{\beta}$ term is also included, which makes the y-directed polarization stronger at high p_x values, 12%, while it was 9% in Ref. [18], both in the negative y direction. Furthermore, the second term changes the structure, of the momentum dependence of $\Pi_{0y}(\boldsymbol{p})$, and it becomes $\pm p_x$ asymmetric.

Recently the vorticity and polarization were also studied in two fluid dynamical models [32]. The initial states that were used from Bozek and Gubser neglected fully the initial shear flow in the central domain of the reaction, in contrast to other models where this is present [1,2,17,33,34]. This results in negligible thermal vorticity in the central domain of the collision (Figs. 3 and 13 of Ref. [32]), and consequently a negligible polarization from the vorticity from the "first term" discussed here. Thus, the observed vorticity arises from the "second term."

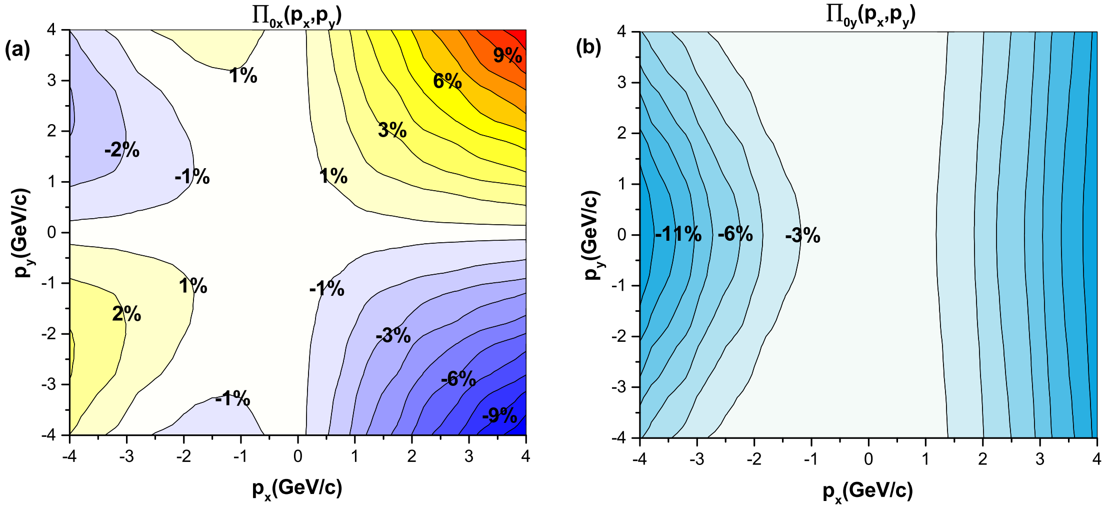

FIG. 8. (Color online) The (a) radial x and (b) axial y components of Λ polarization $\mathbf{\Pi}_0(\boldsymbol{p})$ in the Λ's rest frame. For $\Pi_{0x}(\boldsymbol{p})$ the contours represent changes of 1% from -9.5% in the upper left-hand corner to 9.5% in the upper right-hand corner, whereas the contours of $\Pi_{0y}(\boldsymbol{p})$ change in steps of 2% ranging from $\Pi_{0y} = 0$ (!) at the c.m. momentum ($p_x = p_y = 0$) to -12% for $p_x = \pm 4\text{GeV/c}$ at the edges. Both plots are asymmetric because of the Lorentz boost to the Λ rest frame.

On the other hand there is qualitative agreement between Fig. 12 of Ref. [32] and this work in the sense that only the y-directed (i.e., $[x,z]$ or $[x,\eta]$) component of the vorticity leads to an overall average net polarization. This arises in both models from the initial angular momentum and points into the $-y$ direction. In Ref. [32] this arises as a consequence of viscous evolution of the initial, vorticity-less flow, while in our Exact model it is present in the initial state.

Recent preliminary experimental results reported for the first time [31], significant Λ and $\bar{\Lambda}$ polarization for peripheral collisions at RHIC for beam energies $\sqrt{s_{NN}} = 7.7 - 39$ GeV aligned with the axis direction of the angular momentum of the participant system. Furthermore, the Λ and $\bar{\Lambda}$ polarizations were pointing in the same direction confirming our approach.

In this work we analyzed and compared the two terms of polarization, in the Exact model. Including both rotation and expansion, and vorticity arising from both of these effects enables us to study the consequences of the two terms separately. This study indicates that the assumptions regarding the initial state are influencing the predictions on the observed vorticity, while in all cases observable polarization is predicted.

ACKNOWLEDGMENTS

Enlightening discussions with Sharareh Mehrabi Pari, Francesco Becattini, Eirik Hatlen, Istvan Papp, Stuart Holland, and Sindre Velle are gratefully acknowledged. One of the authors, Y.L.X., is supported by the China Scholarship Council.

---

[1] V. K. Magas, L. P. Csernai, and D. D. Strottman, Phys. Rev. C **64**, 014901 (2001).

[2] V. K. Magas, L. P. Csernai, and D. D. Strottman, Nucl. Phys. A **712**, 167 (2002).

[3] B. McInnes and E. Teo, Nucl. Phys. B **878**, 186 (2014).

[4] B. McInnes, Nucl. Phys. B **887**, 246 (2014).

[5] K. Okamoto, C. Nonaka, and Y. Akamatsu, Poster presented at The XXV International Conference on Ultrarelativistic Nucleus-Nucleus Collisions, Sept. 27–Oct. 3, 2015, Kobe, Japan (published electronically).

[6] L.-G. Pang, H. Petersen, G.-Y. Qin, V. Roy, and X.-N. Wang, Invited talk presented at The XXV International Conference on Ultrelativistic Nucleus-Nucleus Collisions, Sept. 27–Oct. 3, 2015, Kobe, Japan (published electronically).

[7] L. P. Csernai, W. Greiner, H. Stöcker, I. Tanihata, S. Nagamiya, and J. Knoll, Phys. Rev. C **25**, 2482 (1982).

[8] L. P. Csernai, G. Fai, and J. Randrup, Phys. Lett. B **140**, 149 (1984).

[9] L. P. Csernai, V. K. Magas, H. Stöcker, and D. D. Strottman, Phys. Rev. C **84**, 024914 (2011).

[10] L. P. Csernai, D. D. Strottman, and Cs. Anderlik, Phys. Rev. C **85**, 054901 (2012).

[11] T. Csörgő and M. I. Nagy, Phys. Rev. C **89**, 044901 (2014).

[12] L. P. Csernai, D. J. Wang, and T. Csörgő, Phys. Rev. C **90**, 024901 (2014).

[13] L. P. Csernai and S. Velle, Int. J. Mod. Phys. E **23**, 1450043 (2014).

[14] L. P. Csernai, J. I. Kapusta, and L. D. McLerran, Phys. Rev. Lett. **97**, 152303 (2006).

[15] L. P. Csernai, V. K. Magas, and D. J. Wang, Phys. Rev. C **87**, 034906 (2013).

[16] D. J. Wang, Z. Néda, and L. P. Csernai, Phys. Rev. C **87**, 024908 (2013).

[17] G. Graef, M. Bleicher, and M. Lisa, Phys. Rev. C **89**, 014903 (2014).

[18] F. Becattini, L. P. Csernai, and D. J. Wang, Phys. Rev. C **88**, 034905 (2013).

[19] L. P. Csernai and J. H. Inderhaug, Int. J. Mod. Phys. E **24**, 1550013 (2015).

[20] T. A. DeGrand and H. I. Miettinen, Phys. Rev. D **24**, 2419 (1981).

[21] Z.-T. Liang and X.-N. Wang, Phys. Lett. B **629**, 20 (2005); Phys. Rev. Lett. **94**, 102301 (2005).

[22] A. Ayala, E. Cuautle, G. Herrera, and L. M. Montano, Phys. Rev. C **65**, 024902 (2002).

[23] F. Becatinni, V. Chandra, L. Del Zanna, and E. Grossi, Ann. Phys. **338**, 32 (2013).

[24] L. P. Csernai and J. I. Kapusta, Phys. Rev. D **46**, 1379 (1992); Phys. Rev. Lett. **69**, 737 (1992).

[25] T. Csörgó and L. P. Csernai, Phys. Lett. B **333**, 494 (1994).

[26] L. P. Csernai and I. N. Mishustin, Phys. Rev. Lett. **74**, 5005 (1995).

[27] I. S. Gradstein and I. M. Ryzhik, *Table of Integrals, Series, and Products* (Academic Press, Waltham, 2007).

[28] L. P. Csernai, S. Velle, and D. J. Wang, Phys. Rev. C **89**, 034916 (2014).

[29] Horst Stöcker, *Taschenbuch Der Physik* (Harri Deutsch, Frankfurt, 2000).

[30] Yun Cheng, L. P. Csernai, V. K. Magas, B. R. Schlei, and D. Strottman, Phys. Rev. C **81**, 064910 (2010).

[31] M. A. Lisa, Invited talk at the XI Workshop on Particle Correlations and Femtoscopy (WPCF2015), November 3–7, 2015, Warsaw, Poland.

[32] F. Becattini, G. Inghirami, V. Rolando, A. Beraudo, L. Del Zanna, A. De Pace, M. Nardi, G. Pagliara, and V. Chandra, Eur. Phys. J. C **75**, 406 (2015).

[33] G.-Y. Chen and R. J. Fries, Phys. Lett. B **723**, 417 (2013).

[34] J. Kapusta, R. J. Fries, G.-Y. Chen, and Y. Li, Invited talk presented at The XXV International Conference on Ultrarelativistic Nucleus-Nucleus Collisions, Sept. 27–Oct. 3, 2015, Kobe, Japan (published electronically).

Paper 2

Erratum: Λ polarization in peripheral heavy ion collisions

PHYSICAL REVIEW C **93**, 069901(E) (2016)

Erratum: Λ polarization in peripheral heavy ion collisions [Phys. Rev. C 88, 034905 (2013)]

F. Becattini, L. P. Csernai, D. J. Wang, and Y. L. Xie

(Received 2 December 2015; revised manuscript received 13 May 2016; published 6 June 2016)

DOI: 10.1103/PhysRevC.93.069901

In Sec. II, in the un-numbered equation after Eq. (4), we reported the angular distribution of the proton momentum $dN/d\Omega^*$ as a function of the polarization vector $\mathbf{\Pi}_0$. In our convention, which follows that of Ref. [10], this vector has a maximal magnitude of 1/2, i.e., the Λ spin, whereas the usual convention in particle physics has as maximal magnitude 1, i.e., 100% polarization. Therefore, the correct formula for the angular distribution with $\alpha = 0.647$ reads

$$\frac{1}{N}\frac{dN}{d\Omega^*} = \frac{1}{4\pi}(1 + 2\alpha\mathbf{\Pi}_0 \cdot \hat{\mathbf{p}}^*).$$

In Sec. II, below Eq. (3), we erroneously stated that because of parity symmetry, the integral term on the right-hand side of Eq. (3) involving the time derivative of $\boldsymbol{\beta}$ and the gradient of β^0 vanishes. In fact, because of the noninvariance of the β four-vector under reflection $(\beta^0,\boldsymbol{\beta}) \to (\beta^0, -\boldsymbol{\beta})$, the Fermi-Dirac distribution gets changed

$$n_F = \frac{1}{e^{\beta^0\varepsilon - \boldsymbol{\beta}\cdot\mathbf{p} + \mu/T} + 1} \to \frac{1}{e^{\beta^0\varepsilon + \boldsymbol{\beta}\cdot\mathbf{p} + \mu/T} + 1},$$

and the second term on the right-hand side of Eq. (3) does contribute to the polarization vector. This additional term vanishes in the nonrelativistic limit of the flow $\|\boldsymbol{\beta}\| \ll \beta^0$ and of the particle as well ($\|\mathbf{p}\| \ll \varepsilon$).

Under the conditions explored in the paper and according to our calculations, initially the relative contribution of the neglected term to Π_{0y} in Eq. (3) is small and positive. However, for later times, it increases, and at 4.75 fm/c—the time chosen for the stopping of the hydrodynamical regime—it overcomes the first term at high $|p_x|$ and small $|p_y|$. As a consequence, the overall pattern of the $\mathbf{p}_T$ dependence of $\Pi_{0y}(p_x,p_y)$ changes considerably with respect to our previous calculation with a maximal positive (i.e., opposite to the angular momentum, see Fig. 1 in the paper) polarization of 8% at high $|p_x|$ and small $|p_y|$ and a minimum at -6% (negative, i.e., along the angular momentum) at high $|p_y|$ and small $|p_x|$ momenta, whereas the momentum average of Π_{0y} remains negative, see the figure below.

Note that, in the corrected Fig. 3 below, we have plotted the polarization normalized to 1, that is, 2Π with Π as in Eqs. (1), (3), and (4).

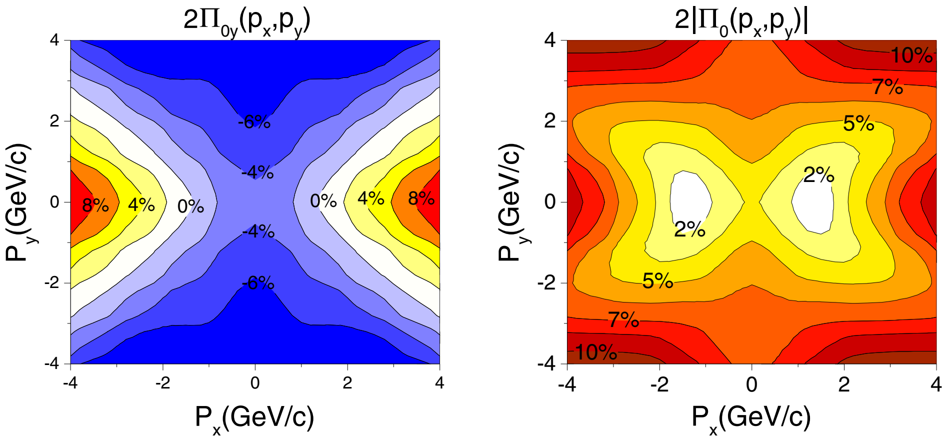

FIG. 3. Replacement for Fig. 3. The y component (left panel) and the modulus of the polarization (right panel) in the rest frame of the Λ as a function of momentum in the transverse plane (i.e., at $p_z = 0$).

Paper 3

Λ polarization in peripheral collisions at moderate relativistic energies

PHYSICAL REVIEW C **94**, 054907 (2016)

Λ polarization in peripheral collisions at moderately relativistic energies

Y. L. Xie,[1] M. Bleicher,[2,3] H. Stöcker,[2,3] D. J. Wang,[4] and L. P. Csernai[1]
[1]*Institute of Physics and Technology, University of Bergen, Allegaten 55, N-5007 Bergen, Norway*
[2]*Frankfurt Institute for Advanced Studies, Goethe University, D-60438 Frankfurt am Main, Germany*
[3]*Institut für Theoretische Physik, Goethe University, D-60438 Frankfurt am Main, Germany*
[4]*School of Science, Wuhan University of Technology, 430070, Wuhan, China*

(Received 20 June 2016; revised manuscript received 31 August 2016; published 21 November 2016)

The polarization of Λ hyperons from relativistic flow vorticity is studied in peripheral heavy ion reactions at FAIR and NICA energies, just above the threshold of the transition to the quark-gluon plasma. Previous calculations at higher energies with larger initial angular momentum, predicted significant Λ polarization based on the classical vorticity term in the polarization, while relativistic modifications decreased the polarization and changed its structure in the momentum space. At the lower energies studied here, we see the same effect namely that the relativistic modifications decrease the polarization arising from the initial shear flow vorticity.

DOI: 10.1103/PhysRevC.94.054907

I. INTRODUCTION

Relativistic heavy ion collisions allow one to explore the properties of hot and dense QCD matter in the laboratory. Among the most prominent observables are the different kinds of transverse flow, e.g., radial flow, directed flow, elliptical flow, and higher order flows. Hydrodynamics was shown to provide direct access to these flow patterns.

In recent fluid dynamical models of relativistic heavy ion reactions, both different fluctuating modes and global collective processes lead to flow observables. It is important to separate or split the two types of flow processes from each other [1,2]. This separation helps to precisely analyze both processes.

In peripheral heavy ion reactions, from the initial angular momentum, the reaction shows shear flow characteristics, leading to rotation [3] and even Kelvin-Helmholtz instabilities (KHI) [4] in the reaction plane, because of the low viscosity quark-gluon plasma. This possibility was indicated by high resolution computational fluid dynamics calculations using the PICR method. The development of these processes was studied in $3+1$-dimensional ($3+1$D) configurations that described the energy and momentum balance realistically [5]. The initial state model assumed transparency as well as stopping [6] because of strong attractive fields with accurate impact parameter and rapidity dependence in the transverse plane [7]. It assumed an initial interpenetration of Lorentz contracted slabs (in most present models considered as CGC), and strong attractive coherent Yang-Mills fields act between these slabs, with large string tension (according to the color rope model [8]).

In a previous work the development of vorticity was studied under the conditions where the viscosity is estimated to have a minimum, so the viscous dissipation is small [9,10], and the spherical expansion is also smaller because of the lower pressure. Thus in the initial local rotation, the vorticity drops slower.

In the PICR calculation [5], the dynamical initial state, a Yang-Mills field theoretical model [7] was used as in Ref. [11], and a longitudinal expansion lasting 4 fm/c from the initial impact was considered.

The classical weighted vorticity Ω_{zx} was calculated in the reaction [x-z] plane, the energy of the Au+Au collision was $\sqrt{s_{NN}} = 4.65 + 4.65$ GeV, $b = 0.5 b_{\max}$.

The used fluid dynamical calculation and this initial state model were tested in several model calculations in the last decade. These describe correctly the initial shear flow characteristics. The angular momentum distribution is based on the assumption that the initial angular momentum of the participants (based on straight propagation geometry) is streak by streak conserved, thus the model satisfies angular momentum conservation both locally and globally. Figure 1 shows the three-dimensional view of the simulated collisions shortly after the impact, and it could naturally generate a longitudinal velocity shear along the x direction, as shown in Fig. 2(a). This type of longitudinal velocity shear is a requirement for the subsequent rotation, turbulence, and even Kelvin Helmholtz instability(KHI), just as discussed in our previous paper [10], as well as in Refs. [12,13]. The vortical flow formed in the equilibrated hydroevolution, as shown in Figs. 2(b)–2(d), can give rise to the polarization from the equipartion principle or spin-orbit coupling.

The peak value of the vorticity at the energy $\sqrt{s_{NN}} = 4.65 + 4.65$ GeV, was a few times smaller than at the ultrarelativistic RHIC and LHC energies, but the negative values are less pronounced. The initial state used is the same as the one that was used at high energy: We assume transparency, QGP formation, and initial longitudinal expansion in the same Yang-Mills string rope model for 4 fm/c time. In addition, the frequently used "Bag Model" EoS was also applied in the hydrosimulation: $P = c_0^2 e^2 - \frac{4}{3}B$, where constant $c_0^2 = \frac{1}{3}$ and B is the Bag constant in QCD [7,14]. The energy density takes the form, $e = \alpha T^4 + \beta T^2 + \gamma + B$, where α, β, γ are constants arising from the degeneracy factors for (anti-)quarks and gluons. At a later time, the drop of the vorticity is not as large as in higher energy heavy ion collisions.

In Ref. [5] the classical and relativistic weighted vorticities Ω_{zx} were evaluated in the reaction plane, [x-z], so that the weighting does not change the average circulation of the layer, i.e., the sum of the average of the weights over all fluid cells is unity. The vorticity projected to the reaction plane for a

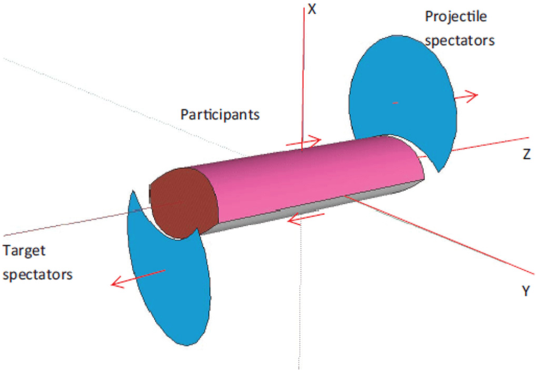

FIG. 1. The three-dimensional view of the collisions shortly after the impact. The projectile spectators are going along the z direction, and the target spectators are going along the z axis. The collision region is assumed to be a cylinder with an almond-shaped profile and tilted end surfaces, where the top side is moving to the right and the bottom is moving to the left. The participant cylinder can be divided into streaks, and each streak has its own velocity, as shown in Fig. 2(a). The velocity differences among the streaks result in rotation, turbulence, and even KHI.

collision for the FAIR-SIS300 energy of $\sqrt{s_{NN}} = 8.0$ GeV is evaluated at an initial moment of time and at a later time. The peak value of the vorticity is similar to the one obtained at the ultrarelativistic RHIC and LHC energies, but the negative values are less pronounced. The average vorticity was decreasing with time: Ω_{zx} is 0.1297/0.0736 for the times, t =0.17 and 3.56 fm/c, respectively. The same behavior was seen in Ref. [15].

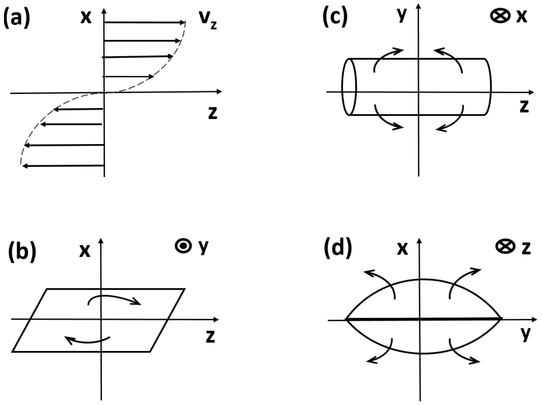

FIG. 2. The schematic hydroflow velocity after the collisions shown in Fig. 1. (a) The longitudinal velocity profile along the x direction, and it gives rise to the v_1 type of flow in the reaction plane, i.e., (b). (c) The anti-v_2 type of flow in the [y-z] plane, and (d) is the v_2 type of flow in the [x-y] plane.

In addition to the directed flow (v_1) [3,16], two methods were proposed so far to detect the effects of rotation: the differential HBT method [17] and the polarization of emitted fermions based on the equipartition of the rotation between the spin and orbital degrees of freedom [18,19].

The particle polarization effect has some advantages and disadvantages. The local polarization depends on the thermal vorticity [18,19]. Now at lower collision energy the temperature is lower and the thermal vorticity increases, which is advantageous. At ultrarelativistic energies this feature led to the conclusion that the predicted polarization is bigger for RHIC than for LHC because of the lower temperature of the system. Furthermore at ultrarelativistic energies, the relativistic corrections to polarization will become stronger compared to the original shear and the resulting classical vorticity [20].

The thermal vorticity occurs in the particle polarization, because the spin-orbit interaction aligns the spins and the orbital momentum, while the random thermal motion works against this alignment. Thus, we use the inverse temperature four-vector field [18,19],

$$\beta^\mu(x) = (1/T(x))u^\mu(x),$$

and define the *thermal vorticity* as

$$\varpi^{\mu\nu} = \tfrac{1}{2}(\partial^\nu \hat{\beta}^\mu - \partial^\mu \hat{\beta}^\nu), \tag{1}$$

where $\hat{\beta}^\mu \equiv \hbar\beta^\mu$. Thereby, ϖ becomes dimensionless.

The relativistic weighted thermal vorticity Ω_{zx}, calculated in the reaction [x-z] plane was presented in Ref. [5]. The energy of the Au+Au collision was $\sqrt{s_{NN}} = 4.65 + 4.65$ GeV, and the impact parameter $b = 0.5b_{\max}$. The obtained average thermal vorticity Ω_{zx} was 0.0847 (0.0739) for the times, $t = 0.17$ and 3.56 fm/c, respectively. It was observed that the thermal vorticity decreases slower than the standard vorticity because of the decreasing temperature.

In Ref. [5] the relativistic weighted thermal vorticity Ω_{zx} was calculated in the reaction [x-z] plane at t=0.34 fm/c and at t=3.72 fm/c for the energy of the collision $\sqrt{s_{NN}} = 4.0 + 4.0$ GeV, $b = 0.5b_{\max}$. Ω_{zx} was 0.0856 (0.0658) for the two selected times.

An analysis of the vorticity for peripheral Au+Au reactions at NICA and U+U reactions at FAIR energies of $\sqrt{s_{NN}} = 9.3(8.0)$ GeV, respectively, gave an initial peak vorticity that was about two times larger than the one obtained from random fluctuations in the transverse plane, of about 0.2 c/fm at much higher energies [21]. This is because of the initial angular momentum arising from the beam energy in noncentral collisions.

The RHIC Beam Energy Scan program measured significant Λ and $\bar{\Lambda}$ polarizations, with the largest values at the lowest energies [22].

At FAIR, the planned facilities, e.g., at PANDA [23], will make it possible to measure proton and antiproton polarization, also in the emission directions where significant polarization is expected.

II. POLARIZATION STUDIES

The flow vorticity was evaluated and reported in [5]. Based on these results we report the Λ polarization results for the same reactions. The initial state Yang-Mills flux-tube model [7] describes the development from the initial touching moment up to 2.5 fm/c. Then the PICR hydrocode is calculated for another 4.75 fm/c, so that the final freeze-out time is 7.25 fm/c.

The Λ and $\bar{\Lambda}$ polarization was calculated based on the work [19],

$$\mathbf{\Pi}(p) = \frac{\hbar\varepsilon}{8m}\,\frac{\int d\Sigma_\lambda p^\lambda n_F\,(\nabla\times\boldsymbol{\beta})}{\int d\Sigma_\lambda p^\lambda n_F} + \frac{\hbar\mathbf{p}}{8m}\times\frac{\int d\Sigma_\lambda p^\lambda n_F\,(\partial_t\boldsymbol{\beta}+\nabla\beta^0)}{\int d\Sigma_\lambda p^\lambda n_F}, \qquad (2)$$

where $n_F(x,p)$ is the Fermi-Jüttner distribution of the Λ, that is $1/(e^{\beta(x)\cdot p-\xi(x)}+1)$, being $\xi(x)=\mu(x)/T(x)$ with μ the relevant Λ chemical potential and p its four-momentum. $d\Sigma_\lambda$ is the freeze-out hypersurface element for $t=$const. freeze-out $d\Sigma_\lambda p^\lambda \rightarrow dV\varepsilon$, where $\varepsilon = p^0$ is the Λ's energy.

Here the *first term* is the classical vorticity term, while the *second term* is the relativistic modification. The above convention of $\mathbf{\Pi}(p)$ [19] is normalized to max. 50%, while in the experimental evaluation it is 100%, thus we present the values of $2\mathbf{\Pi}(p)$ [20], unlike in earlier calculations [18,24,25].

In Fig. 3 the dominant y component of the polarization vector $\mathbf{\Pi}(p)$, for the first and second terms are shown. The first term is pointing into the negative y direction with a maximum of −26%. The structure of the first term arises from the v_1 type of flow in Fig. 2(b), which is also unipolar and negative y directed. The second term has a different structure; it points in the opposite direction and has a maximum of +22%, i.e., ∼4% less than the absolute value of the first term.

In Fig. 4 the x component of the polarization vector $\mathbf{\Pi}(p)$, for the first and second terms are shown. The first term is about four times smaller than the y component, ±6%, and the positive and negative values are symmetric in a way that the integrated value of the polarization over the momentum space in the transverse plane is vanishing. This sign distribution is just the manifestation of anti-v_2 type of flow in the $[y$-$z]$ plane, seen in Fig. 2(c) with a dipole structure. The second term is about half of the y component, ±17%, and the positive and negative values are symmetric in a way that the integrated value of the polarization over the momentum space in the transverse plane is vanishing. Furthermore the first and second terms have opposite signs at the same momentum values in the transverse plane, which decreases further their effect.

In Fig. 5 the z component of the polarization vector $\mathbf{\Pi}(p)$, for the first and second terms are shown. The first term has a maximum of ±2%, and the positive and negative values are symmetric in a way that the integrated value of the polarization over the momentum space in the transverse plane is vanishing. This sign distribution is also the manifestation of the anti-v_2 type of flow in the $[x$-$y]$ plane, i.e., a dipole structure in Fig. 2(d). The second term has similar structure to the first one, with a maximum of ±2% also, but the first and second terms have similar structure in the momentum space.

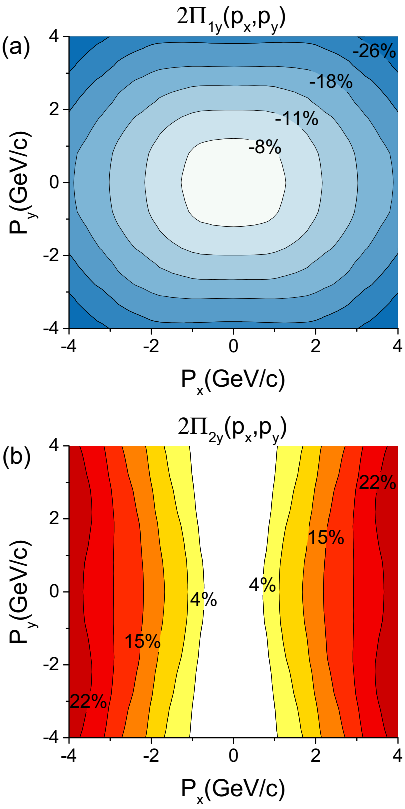

FIG. 3. The first (top) and second (bottom) term of the dominant y component of the Λ polarization for momentum vectors in the transverse, $[p_x,p_y]$, plane at $p_z=0$, for the FAIR U+U reaction at $\sqrt{s_{NN}}=8.0$ GeV.

In Fig. 6 the dominant y component of the polarization vector $\mathbf{\Pi}(p)$, for the sum of the first and second terms is shown. The top figure is the distribution of the polarization in the center-of-mass frame while the bottom figure is in the local rest frame of the Λ.

Figure 7 shows the modulus of the polarization vector $\mathbf{\Pi}(p)$. The maximum at high $|p_y|$ and low $|p_x|$ is the same as the absolute value of the Π_{0y} component. Here the other components have only minor contributions to the final observed polarization. At the corners, at high $|p_y|$ and high $|p_x|$, the contribution of the x and z components of $\mathbf{\Pi}(p)$ dominates, while the y component has a minimum.

Figure 8 shows the y component and the modulus of the polarization vector $\mathbf{\Pi}(p)$ for the NICA Au+Au reaction at $\sqrt{s_{NN}}=9.3$ GeV. The structure and magnitude of the polarization is similar to the reactions at FAIR. The negative maximum at high $|p_y|$ and low $|p_x|$ arises from the classical vorticity in the y component. The positive maximum at high

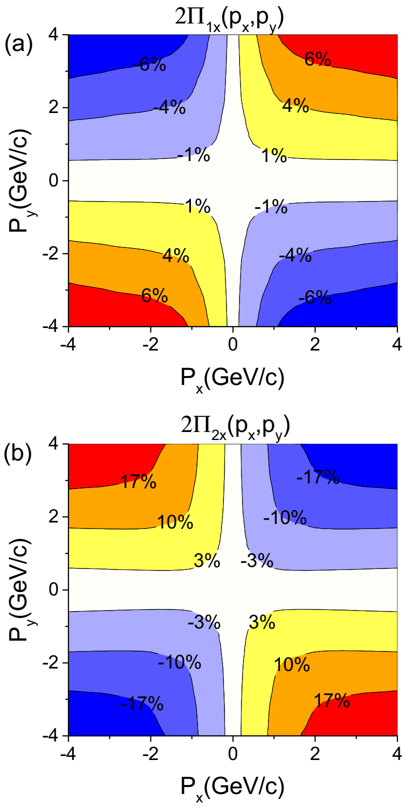

FIG. 4. The first (top) and second (bottom) term of the x component of the Λ polarization for momentum vectors in the transverse, $[p_x,p_y]$, plane at $p_z = 0$, for the FAIR U+U reaction at $\sqrt{s_{NN}} = 8.0$ GeV.

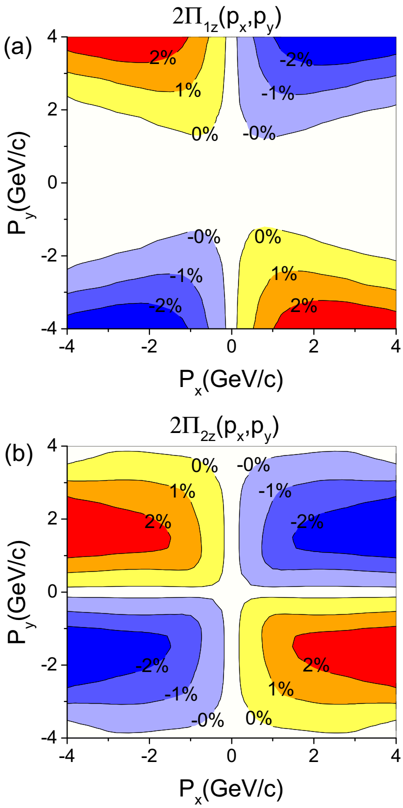

FIG. 5. The first (top) and second (bottom) term of the z component of the Λ polarization for momentum vectors in the transverse, $[p_x,p_y]$, plane at $p_z = 0$, for the FAIR U+U reaction at $\sqrt{s_{NN}} = 8.0$ GeV.

$|p_x|$ and low $|p_y|$ arises from the relativistic modifications of the second term. The momentum space average is dominated by the first term.

The polarization studies at ultrarelativistic, RHIC and LHC energies, turned out to be sensitive to both the classical vorticity of the flow (first term) and the relativistic modifications arising from rapid expansion expansion at later stages of the flow (second term) [18,20].

Initially the contribution of the classical vorticity is stronger than the relativistic modification term, i.e., the "second" term. This is in line with earlier observations [5,15]. The effect of this decrease is also visible in the polarization results. The Λ polarization was evaluated at earlier freeze-out time, $t = 2.5 + 1.7$ fm/c $= 4.2$ fm/c for the FAIR U+U reaction. See Fig. 9

The y component and the modulus of the polarization vector $\mathbf{\Pi}(p)$ have very similar structure and magnitude, although the y component points in the negative y direction as the angular momentum vector from the initial shear flow. This indicates that the other, x and z, components are of the order of 1% only at moderate momenta where the y component and the modulus are of the order of 5%–6%. At the "corners," at high $|p_y|$ and high $|p_x|$, the contribution of the x and z components of $\mathbf{\Pi}(p)$ are approaching that of the y component, so that the modulus is larger than the y component, by 4%–5%. Still the contribution of these second term components is clearly smaller than the classical vorticity component.

It is important to mention the role of the initial condition. The *second term*, the relativistic modification, develops during the expansion of the system and is not very sensitive to the initial state. This is shown by the fact that the structure of the x component of polarization, Π_{2x} in the dominant Fig. 4(b), is very similar to Fig. 14(b) of Ref. [25]. At the same time here the initial shear and classical vorticity are present in the initial state with strong stopping and dominance of the Yang-Mills field [6,7], while in Ref. [25] this is not present. As a consequence the final polarization estimates in the y direction are different in the two models.

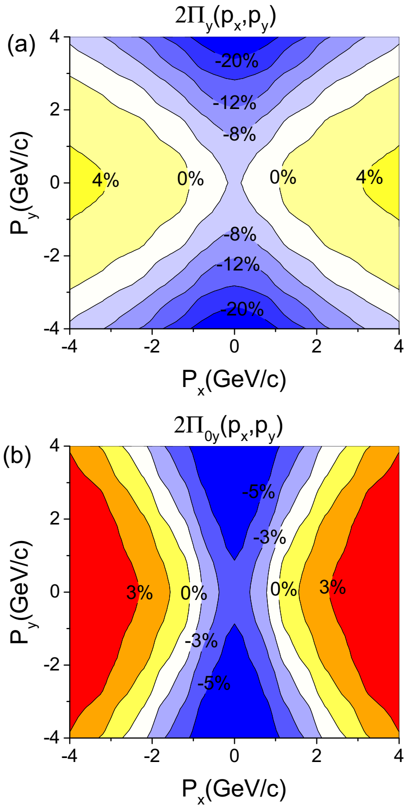

FIG. 6. The y component of the Λ polarization for momentum vectors in the transverse, $[p_x, p_y]$, plane at $p_z = 0$, for the FAIR U+U reaction at $\sqrt{s_{NN}} = 8.0$ GeV. The top figure is in the calculation frame, while the bottom figure is boosted to the frame of the Λ [18].

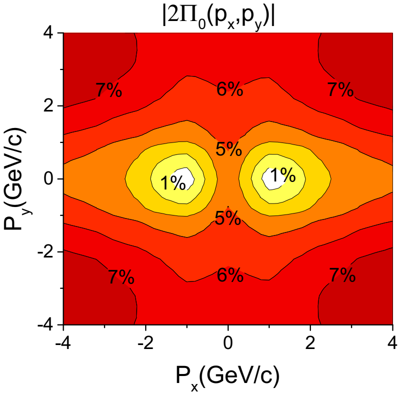

FIG. 7. The modulus of the Λ polarization for momentum vectors in the transverse, $[p_x, p_y]$, plane at $p_z = 0$, for the FAIR U+U reaction at $\sqrt{s_{NN}} = 8.0$ GeV. The figure is in the frame of the Λ.

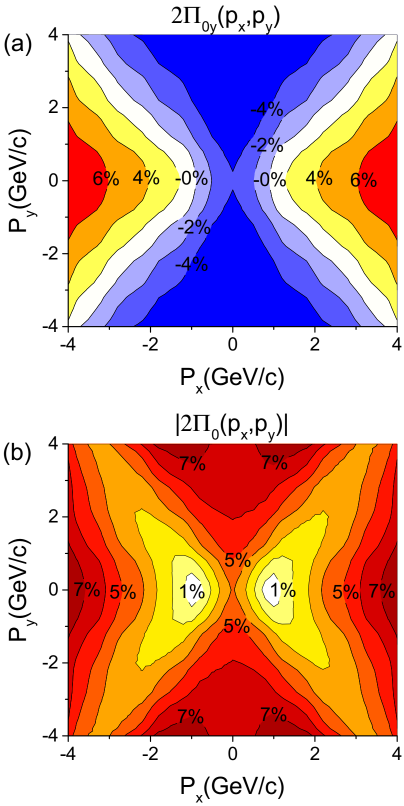

FIG. 8. The y component (top) and the modulus (bottom) of the Λ polarization for momentum vectors in the transverse, $[p_x, p_y]$, plane at $p_z = 0$, for the NICA Au+Au reaction at $\sqrt{s_{NN}} = 9.3$ GeV. The figure is in the frame of the Λ.

III. TOTAL Λ POLARIZATION INTEGRATED OVER MOMENTUM SPACE

Because the experimental results for Λ polarization are averaged polarizations over the Λ momentum, we evaluated the average of the y component of the polarization $\langle \Pi_{0y} \rangle_p$. We integrated the y component of the obtained polarization Π_{0y} over the momentum space as follows:

$$\langle \Pi_{0y} \rangle_p = \frac{\int dp\, dx\, \Pi_{0y}(p,x)\, n_F(x,p)}{\int dp\, dx\, n_F(x,p)} = \frac{\int dp\, \Pi_{0y}(p)\, n_F(p)}{\int dp\, n_F(p)}. \tag{3}$$

For Au+Au collisions at NICA energy (9.3 GeV/A), the avarged y component of polarization is 1.82%, at freeze-out time $2.5 + 4.75$ fm/c, while for the U+U collisions at FAIR energy (8 GeV/A) at the same time, the value is 1.85%, a bit larger. As some papers [18,26] had pointed out, the Λ polarization scales with $x_F = 2p/\sqrt{s}$, thus the Λ polarization

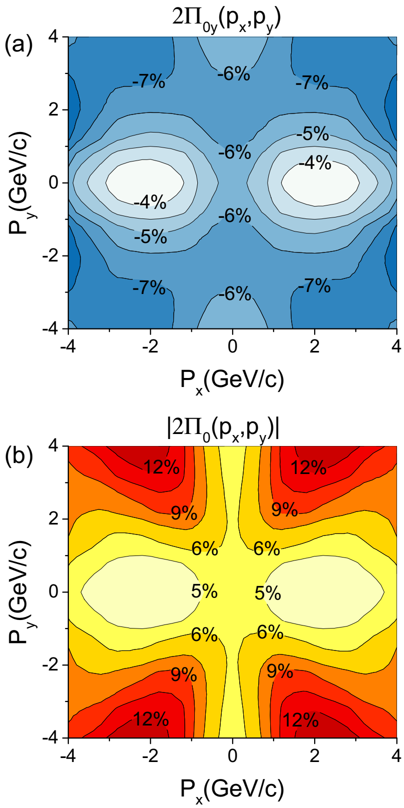

FIG. 9. The y component (top) and the modulus (bottom) of the Λ polarization for momentum vectors in the transverse, $[p_x, p_y]$, plane at $p_z = 0$, for the FAIR U+U reaction at $\sqrt{s_{NN}} = 8$ GeV at the earlier freeze-out time of $t = 4.2$ fm/c. The figure is in the frame of the Λ.

should increase with decreasing energy, which is also, more or less, being confirmed by our results. We also evaluated the average polarization for U+U collisions at 8 GeV/A energy at an earlier time 2.5+1.7 fm/c, and the obtained value is about 2.02%, showing that the average polarization is decreasing with freeze-out time.

It is important to mention that if vorticity and polarization are dominated by the expansion and not by the initial shear flow then the vorticity is symmetric (see Fig. 13 of Ref. [25]), and the polarization also as shown in Fig. 4(b), and similarly in Fig. 14(b) of Ref. [25]. Because of the symmetry of the polarization in the ± directions these polarizations average out to zero. This applies to the y directed polarization in the model initial state of Ref. [25] also. The result that the present model yields to a net average polarization, Π_{0y}, in the negative y direction, is because of the strong shear flow and vorticity in the initial state.

The vorticity induced by the initial orbital angular momentum will eventually give rise to nonvanishing local and global polarization, which is aligned with the initial angular momentum [12,13,27–31]. As Eq. (4.4) in Ref. [12] shows, the quark polarization rate is sensitive to the viscosity η/s. This equation also indicates that the modulus of quark polarization is inversely proportional with the center-of-mass energy. On the other hand, this equation is based on the one-dimensional Bjorken assumption, i.e., the transverse expansion was not considered, while in our model the spherical expansion is manifested in the second term, and obviously influences the final polarization significantly.

Previous experimental results, e.g., Au+Au collisions at 62.4 and 200 GeV in RHIC, have shown global polarization [32], with large error bars. We have to point out that these experiments had a centrality percentage of 0%–80% in RHIC, which dilutes the obtained polarization values after averaging. Also the azimuth averaged values are much smaller than values for given azimuthal ranges as shown in Fig. 8. Furthermore Fig. 2 in Ref. [28] and Fig. 3 in Ref. [33] have shown a centrality region of nontrivial initial angular momentum, which drops drastically above 50% and below 20% centrality percentage. Because the polarization originates from initial angular momentum, it is better to measure the polarization effect in the 20%–50% centrality percentage range. The centrality percentage value used in our model is 30%, which gives us the peak value of initial angular momentum.

For the correct determination of the momentum space dependence of Λ polarization, we have to know the reaction plane and the center of mass (c.m.) of the participant system in a peripheral heavy ion reaction. The event by event (EbE) determination of the longitudinal c.m. of participants could be measured by the forward backward asymmetry of the particles in the zero degree calorimeters (ZDCs). In colliders only single neutrons are measured in the ZDCs, so one has to extrapolate from these to the total spectator momenta. This method to detect the EbE c.m. was proposed in Refs. [1,34].

At collider experiments, e.g., the LHC-ALICE or RHIC-STAR, this determination was not performed up to now, with the argument [35] that nuclear multifragmentation may also lead to fluctuation of single neutron hits in ZDCs, and therefore c.m. frame would have been determined inaccurately. However, at FAIR's fixed target experiments, it is possible to detect all the fragments from multifragmentation of spectators, thus the c.m. frame can be determined accurately.

Because the experimental measurement of global Λ polarization is conducted around a different azimuthal angle, it is crucial to accurately define the EbE c.m. frame. In symmetric collider experiments, the c.m. frame de facto fluctuates around the actual c.m. frame. The fixed target FAIR setup can get rid of this uncertainty perfectly. The compressed byronic matter (CBM) experiments will be able to measure the polarization effects at SIS-100 and SIS-300 with millions times higher intensity and event rate, up to six order of magnitude than at the RHIC Beam Energy Scan program.

The higher multiplicity thus allows for the high resolution measurement of the momentum space dependence of the Λ

polarization, which can be decisive to determine the dominant polarization mechanism.

IV. SUMMARY

We have explored Λ polarization as an observable signal for the vorticity created in peripheral heavy ion collisions. The studies were performed within a $(3+1\text{D})$ hydrodynamic simulation for U+U collisions at FAIR energies ($\sim\sqrt{s_{NN}} = 8$ GeV). We predicted a sizable polarization signature in the emitted Λ hyperons that can directly signal the initial vorticity. The predictions can be explored at the NICA and FAIR facilities in the near future.

Note added in proof. The field is in rapid development, which is indicated by several recent publications [36–39].

ACKNOWLEDGMENTS

Enlightening discussions with Francesco Becattini are gratefully acknowledged. This work was partially supported by the Helmholtz International Center for FAIR within the Hessian LOEWE initiative.

[1] L. P. Csernai and H. Stöcker, J. Phys. G **41**, 124001 (2014).
[2] S. Floerchinger and U. A. Wiedemann, Phys. Rev. C **88**, 044906 (2013).
[3] L. P. Csernai, V. K. Magas, H. Stöcker, and D. D. Strottman, Phys. Rev. C **84**, 024914 (2011).
[4] L. P. Csernai, D. D. Strottman, and Cs. Anderlik, Phys. Rev. C **85**, 054901 (2012).
[5] L. P. Csernai, D. J. Wang, M. Bleicher, and H. Stöcker, Phys. Rev. C **90**, 021904(R) (2014).
[6] L. P. Csernai and J. I. Kapusta, Phys. Rev. D **31**, 2795 (1985).
[7] V. K. Magas, L. P. Csernai, and D. D. Strottman, Phys. Rev. C **64**, 014901 (2001); Nucl. Phys. A **712**, 167 (2002).
[8] T. S. Biró, H. B. Nielsen, and J. Knoll, Nucl. Phys. B **245**, 449 (1984).
[9] P. K. Kovtun, D. T. Son, and A. O. Starinets, Phys. Rev. Lett. **94**, 111601 (2005).
[10] L. P. Csernai, J. I. Kapusta, and L. D. McLerran, Phys. Rev. Lett. **97**, 152303 (2006).
[11] L. P. Csernai, V. K. Magas, and D. J. Wang, Phys. Rev. C **87**, 034906 (2013).
[12] X.-G. Huang, P. Huovinen, and X.-N. Wang, Phys. Rev. C **84**, 054910 (2011).
[13] Z.-T. Liang and X.-N. Wang, Phys. Lett. B **629**, 20 (2005).
[14] L. P. Csernai, *Introduction to Relativistic Heavy Ion Collisions* (Jonh Wiley & Sons, Chichester, 1994).
[15] Y. Jiang, Z.-W. Lin, and J.-F. Liao, Phys. Rev. C **94**, 044910 (2016).
[16] J. Steinheimer, J. Auvinen, H. Petersen, M. Bleicher, and H. Stöcker, Phys. Rev. C **89**, 054913 (2014).
[17] L. P. Csernai, S. Velle, and D. J. Wang, Phys. Rev. C **89**, 034916 (2014); L. P. Csernai and S. Velle, Int. J. Mod. Phys. E **23**, 1450043 (2014).
[18] F. Becattini, L. P. Csernai, and D. J. Wang, Phys. Rev. C **88**, 034905 (2013).
[19] F. Becattini, V. Chandra, L. Del Zanna, and E. Grossi, Ann. Phys. **338**, 32 (2013).
[20] F. Becattini, L. P. Csernai, D. J. Wang, and Y. L. Xie, Phys. Rev. C **93**, 069901(E) (2016).
[21] S. Floerchinger and U. A. Wiedemann, JHEP 11 (2011) 100; J. Phys. G: Nucl. Part. Phys. **38**, 124171 (2011).
[22] M. A. Lisa *et al.* (STAR Collaboration), Invited talk presented at the QCD Chirality Workshop 2016, Feb. 23–26, 2016, Los Angeles, USA.
[23] A. Dbeyssi, in *Proceedings of Science* (International School for Advanced Studies, Trieste, 2013), p. 059.
[24] Y. L. Xie, R. C. Glastad, and L. P. Csernai, Phys. Rev. C **92**, 064901 (2015).
[25] F. Becattini, G. Inghirami, V. Rolando, A. Beraudo, L. Del Zanna, A. De Pace, M. Nardi, G. Pagliara, and V. Chandra, Eur. Phys. J. C **75**, 406 (2015).
[26] A. M. Smith *et al.* (R608 Collaboration), Phys. Lett. B **185**, 209 (1987).
[27] J.-H. Gao, Z-T. Liang, S. Pu, Q. Wang, and X.-N. Wang, Phys. Rev. Lett. **109**, 232301 (2012).
[28] J.-H. Gao, S.-W. Chen, W.-T. Deng, Z.-T. Liang, Q. Wang, and X.-N. Wang, Phys. Rev. C **77**, 044902 (2008).
[29] Z.-T. Liang and X.-N. Wang, Phys. Rev. Lett. **94**, 102301 (2005).
[30] F. Becattini and F. Piccinini, Ann. Phys. **323**, 2452 (2008).
[31] L.-G. Pang, H. Petersen, Q. Wang, and X.-N. Wang, Phys. Rev. Lett. **117**, 192301 (2016).
[32] B. I. Abelev *et al.* (STAR Collaboration), Phys. Rev. C **76**, 024915 (2007).
[33] F. Becattini, F. Piccinini, and J. Rizzo, Phys. Rev. C **77**, 024906 (2008).
[34] L. P. Csernai, G. Eyyubova, and V. K. Magas, Phys. Rev. C **86**, 024912 (2012).
[35] J. Schukraft (private communication).
[36] I. Karpenko and F. Becattini, arXiv:1610.04717.
[37] F. Becattini, I. Karpenko, M. Lisa, I. Upsal, and S. Voloshin, arXiv:1610.02506.
[38] A. Sorin and O. Teryaev, arXiv:1606.08398.
[39] M. Baznat, K. Gudima, A. Sorin, and O. Teryaev, Phys. Rev. C **93**, 031902(R) (2016).

Paper 4

Λ polarization in high energy collisions

PHYSICAL REVIEW C **95**, 031901(R) (2017)

Global Λ polarization in high energy collisions

Yilong Xie,[1] Dujuan Wang,[2] and László P. Csernai[1]
[1]*Institute of Physics and Technology, University of Bergen, Allegaten 55, 5007 Bergen, Norway*
[2]*School of Science, Wuhan University of Technology, 430070, Wuhan, China*

(Received 1 November 2016; published 14 March 2017)

With a Yang-Mills flux-tube initial state and a high-resolution (3+1)D particle-in-cell relativistic (PICR) hydrodynamics simulation, we calculate the Λ polarization for different energies. The origination of polarization in high energy collisions is discussed, and we find linear impact parameter dependence of the global Λ polarization. Furthermore, the global Λ polarization in our model decreases very quickly in the low energy domain, and the decline curve fits well the recent results of Beam Energy Scan (BES) program launched by the STAR Collaboration at the Relativistic Heavy Ion Collider (RHIC). The time evolution of polarization is also discussed.

DOI: 10.1103/PhysRevC.95.031901

Introduction. The nontrivial polarization effect in high energy collisions, since it was first observed in Fermilab with both polarized and unpolarized incident beams [1,2], has been raising people's interest. The Λ hyperon is well suited to measure the polarization because through the decay $\Lambda^0 \rightarrow p + \pi^-$ with proton carrying the spin information, the Λ becomes its own spin analyzer. Afterwards, more experimental research was launched continuously, including nucleon collisions and heavy ion collisions [3–9]. Theoretical studies have also been under way synchronously with the experiments [10–19].

These experiments have observed that (1) the Λ polarization is perpendicular to the reaction plane and (2) increases with the Λ's transverse momentum (p_T) and its Feynman x, taken to be $x_F = p_L/\sqrt{s}$ [4,5,7]. However, no significant evidence was found to indicate the energy dependence of the hyperon polarization, which we will discuss in this Rapid Communication.

The Λ polarization in experiments was measured through the angular distribution of emitted protons in Λ's rest frame:

$$\frac{dN}{d\cos\theta} = (1 + \alpha P \cos\theta)/4\pi, \quad (1)$$

where θ is the angle between the proton momenta $\boldsymbol{p}_p$ and the Λ's spin $\boldsymbol{S}_\Lambda$, P is the polarization amplitude, and the decay parameter α is taken to be 0.647 ± 0.013 [1,8]. To perform the measurement and calculation, it is crucial to determine the reaction plane (RP) and center of mass (c.m.) of the participant system. Recently it was pointed out that in collider experiments the c.m. frame determination might not be accurate enough due to the nuclear fragmentation effects, while the early fixed target experiments can get rid of this issue [20].

From these experiments, theorists have suggested that the hyperon polarization originates from the initial substantial angular momentum, $\boldsymbol{L}$, in noncentral collisions, since the global polarization aligns with the orbital angular momentum. The initial angular momentum is dependent on impact parameter, or centrality percentage, taking a shape of quadratic function that peaks around 9% centrality percentage, as shown in Refs. [21,22]. In the RHIC's Au+Au collisions at 62.4 and 200 GeV, no centrality dependence of the global hyperon polarization was analyzed [23], due to the insignificant polarization. Recently, stronger polarization signal was observed in RHIC's Beam Energy Scan (BES) program in the energy region below 100 GeV [24]. Therefore, in this Rapid Communication we will explore this issue again.

During past decades, two different perspectives were developed for the transition mechanism from initial angular momentum to the final state hyperon polarization, i.e., the hydrodynamical perspective and partonic kinetic perspective. From the partonic micro-perspective, the initial angular momentum is transferred to the partons through the interaction of spin-orbit coupling in viscous QGP [11], and then the global polarized quarks are recombined into hadrons, in which the Thomas precession of the quark spin was applied [25].

In the hydro- and thermodynamical description, the initial angular momentum is manifested in a longitudinal velocity shear, which, with small shear viscosity, results into a rotating system with substantial vorticity and even Kelvin-Helmholtz instability [26]. Assuming local equilibrium at freeze-out and equipartition of the spin degree of freedom, Ref. [15] put forward a polarization 3-vector for spin-1/2 particles and antiparticles based on the generalization of Cooper-Frye formula for particles with spin.

It was recently pointed out that the detailed balance of Cooper-Frye formula on freeze-out (FO) hypersurface requires a nonvanishing polarization in fluid before FO [27]. However, the absence of pre-FO polarization should not significantly effect the polarization calculation based on Ref. [15]. One can calculate that, the spin of each baryon is $L = \hbar/2 \approx 98.5$ MeV fm/c. As the polarization is between 1 and 10% at different beam energies in the RHIC BES program, this gives $L \approx 1$–10 MeV fm/c for the angular momentum carried by one baryon. On the other hand the total angular momentum is around [28]: $L = 1.05 \times 10^4 \hbar = 205.8 \times 10^4$ MeV fm/c. This is distributed among a few hundred baryons in semiperipheral reactions at not too high energies, i.e., very few antibaryons, which gives an angular momentum per baryon: $L \approx 10^4$ MeV fm/c. This is 3 to 4 orders of magnitude bigger than the spin angular momentum carried by one baryon in the vortical flow. Therefore, even if 1–10% of spins are already polarized before FO, carrying only one per mil of the total angular momentum, they will neither effectively impact the fluid dynamical evolution, nor significantly change the detailed balance during FO process, thus keeping the validity of the polarization 3-vector in Ref. [15].

References [17,18] applied this polarization 3-vector to relativistic heavy ion collisions to explore the momentum space distribution of Λ polarization. However, the previously neglected second term of the polarization formula, which reflects the effect of system expansion, turned out to be not negligible. In this Rapid Communication, we will compute the complete Λ polarization, including both the first and second terms, for the Au+Au collisions in the same energy domain as the RHIC BES program.

Λ polarization in hydrodynamic model. The initial state we used here could naturally generate a longitudinal velocity shear [29,30], which leads to the hyperon polarization after the hydrodynamical evolution, simulated by a high-resolution computational fluid dynamic (CFD) calculation using the relativistic particle-in-cell (PICR) method. This initial state assumed a Yang-Mills field string tension between Lorentz contracted streaks after impact, and conserved the angular momentum both locally and globally. Both in the initial state and subsequent CFD simulation, the frequently used bag model equation of state (EoS) was applied: $P = c_0^2 e^2 - \frac{4}{3}B$, with constant $c_0^2 = \frac{1}{3}$ and a fixed bag constant B [29–31]. The energy density takes the form $e = \alpha T^4 + \beta T^2 + \gamma + B$, where α, β, γ are constants arising from the degeneracy factors for (anti)quarks and gluons. At freeze-out (FO) stage, the major part of FO hypersurface is assumed to be timelike, which entails small changes between the pre-FO and post-FO state, and thus the ideal gas phase space distribution can be applied [18,32].

The spatial part of polarization 3-vector for (anti) hyperon with mass m reads as [17–19]

$$\mathbf{\Pi}(p) = \frac{\hbar\varepsilon}{8m}\,\frac{\int d\Sigma_\lambda p^\lambda\, n_F\,(\nabla\times\boldsymbol{\beta})}{\int d\Sigma_\lambda p^\lambda\, n_F} + \frac{\hbar\mathbf{p}}{8m}\times\frac{\int d\Sigma_\lambda p^\lambda\, n_F\,(\partial_t\boldsymbol{\beta}+\nabla\beta^0)}{\int d\Sigma_\lambda p^\lambda\, n_F}\,, \qquad (2)$$

where $\beta^\mu(x) = (\beta^0, \boldsymbol{\beta}) = [1/T(x)]u^\mu(x)$ is the inverse temperature four-vector field, and $n_F(x,p)$ is the Fermi-Jüttner distribution of the Λ, that is $1/(e^{\beta(x)\cdot p-\xi(x)}+1)$, being $\xi(x) = \mu(x)/T(x)$ with μ being the Λ's chemical potential and p its four-momentum. $d\Sigma_\lambda$ is the freeze-out hypersurface element, for $t = $ const. freeze-out, $d\Sigma_\lambda p^\lambda \rightarrow dV\varepsilon$, where $\varepsilon = p^0$ is the Λ's energy.

Here the *first term* reflects the classical vorticity effect ($\nabla\times\beta$), and the *second term* arises from the expansion effect ($\partial_t\boldsymbol{\beta}$) and relativistic modification ($\nabla\beta^0$). Noticing that the convention of $\Pi(p)$ is normalized to 50%, i.e., Eq. (1), the value should be multiplied by 2 to keep in line with the polarization anisotropy in experimental studies, where the upper limit is 100%. This is unlike the previous studies [13,17–19]. Besides, Eq. (2) is calculated in the center-of-mass (c.m.) frame, and one can Lorentz boost it into Λ's rest frame by the following formula:

$$\mathbf{\Pi}_0(\boldsymbol{p}) = \mathbf{\Pi}(p) - \frac{\boldsymbol{p}}{p^0(p^0+m)}\mathbf{\Pi}(p)\cdot\boldsymbol{p}. \qquad (3)$$

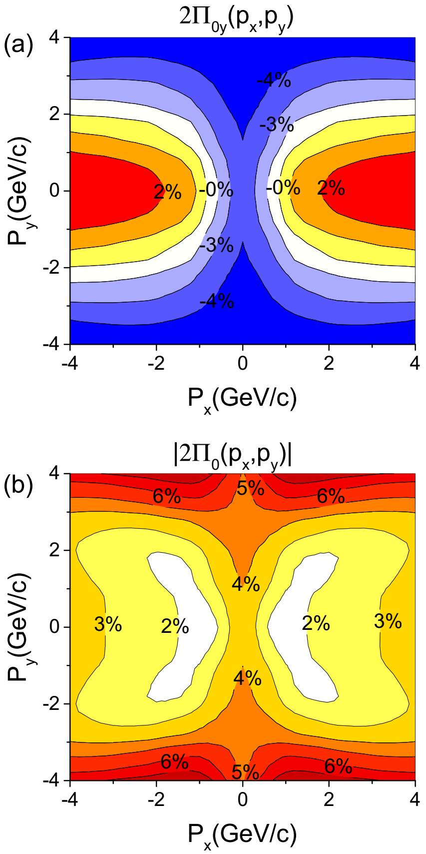

FIG. 1. The y component (top) and the modulus (bottom) of the Λ polarization for momentum vectors in the transverse, $[p_x, p_y]$, plane at $p_z = 0$, for the Au+Au reaction at $\sqrt{s_{NN}} = 11.5$ GeV. The figure is in the frame of the Λ. The impact parameter $b = 0.7b_m = 0.7\times 2R$, where R is the radius of Au and $b_m = 2R$ is the maximum value of b. The freeze-out time is $6.25 = (2.5 + 4.75)$ fm/c, including 2.5 fm/c for initial state and 4.75 fm/c for hydroevolution.

The three components of the polarization 3-vectors, $2\mathbf{\Pi}(p_x, p_y)$ [or $2\mathbf{\Pi_0}(p_x, p_y)$], have different significance. As we pointed out in our earlier paper [19], the x and y components of polarization, $2\Pi_x$ and $2\Pi_x$, in transverse momentum space $[p_x, p_y]$ are rather trivial and form a symmetric dipole structure, which results in vanishing global polarization along the x and y direction in the participant c.m. frame. Meanwhile, as expected, the $-y$ directed polarization, aligned with the initial angular momentum, dominates the modulus of polarization 3-vector, $2|\mathbf{\Pi_0}(\boldsymbol{p_x}, \boldsymbol{p_y})|$. Figure 1 shows the dominant y component and the modulus of Λ polarization, in Au-Au collisions at 11.5 GeV. One can see that the top and bottom figures have similar structures and magnitudes, which indicates a trivial influence of the x and y components on the global polarization.

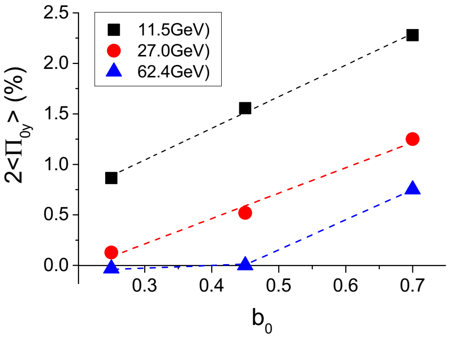

FIG. 2. The linear dependence of global polarization, $2\langle\Pi_{0y}\rangle_p$, as a function of impact parameter ratio b_0 at 11.5, 27.0, and 62.4 GeV.

Since the $-y$ directed global Λ polarization in experimental results is averaged polarization over the Λ's momentum space, we evaluated the average of the y component of the polarization $\langle\Pi_{0y}\rangle_p$. We integrated the y component of the obtained polarization, Π_{0y}, over the momentum space as follows:

$$\langle\Pi_{0y}\rangle_p = \frac{\int dp\,dx\,\Pi_{0y}(p,x)\,n_F(x,p)}{\int dp\,dx\,n_F(x,p)} = \frac{\int dp\,\Pi_{0y}(p)\,n_F(p)}{\int dp\,n_F(p)} \tag{4}$$

to calculate the global polarization. The word *global* means averaging over phase space $[\boldsymbol{x},\boldsymbol{p}]$. Besides, we replace the $\langle\Pi_{0y}\rangle_p$ with $-\langle\Pi_{0y}\rangle_p$, since in experiments the angular momentum's direction, i.e., negative y direction, is the conventional direction for global polarization.

Results and discussion. According to the alignment of polarization and the system's angular momentum, theorists suggested attributing the polarization to the initial orbital angular momentum arising in noncentral collisions. References [21,22] have analytically deduced and schematically displayed the initial angular momentum in the reaction region as a function of impact parameter b, taking the form of quadratic function, which roughly peaks at $b = 0.25b_m$ or $0.3b_m$. If the angular momentum is translated into polarization without any other significant perturbative mechanism, one should also observe the polarization's dependence on impact parameter. In other words, the initial angular momentum of the participant system is initiated by the inequality of local nuclear density in the transverse plane, and this inequality is dependent on the impact parameter. Thus the initial impact parameter dependence of the late-state polarization should in principle be observed.

Figure 2 shows the global polarization of Au+Au collisions as a function of ratio of impact parameter b to Au's nuclear radius R, i.e., $b_0 = b/2R$. One could see that the polarization at different energies indeed approximately takes a linear increase with the increase of impact parameter, except for 62.4 GeV, due to the vanishing polarization signals at relatively central collisions. This linear dependence clearly indicates that the polarization in our model arises from the initial angular momentum. However, the polarization's linear dependence on b is somewhat different from the angular momentum's quadratic dependence on b. This is because the angular momentum L is an extensive quantity dependent on the system's mass, while the polarization Π is an intensive quantity.

An earlier Λ global polarization measurement by the STAR Collaboration in Au+Au collisions at 62.4 and 200 GeV had observed an insignificant indication of centrality dependence, due to the occurrence of negative polarization, as well as large error bars [9,33]. The result of opposite directed global polarization at different centralities would be weird, if we assume that polarization comes from the angular momentum. Besides, no experimental Λ polarization measurements before the present ones had observed the opposite-pointing direction of global Λ polarization [1–6]. This might be because of the inappropriate choice of momentum space. However, from Figs. 5 and 7 in Refs. [9,33] one could still see that the polarization signal becomes stronger at larger centrality, while at small centrality percentage (below 40%) the signal is weak and vanishing. Similar behavior occurs in our simulation results for 62.4 GeV; specifically the polarization value also vanishes when the centrality percentage goes below 20% and increases as the centrality increases.

The recently reported global Λ polarization observation in STAR's BES I program has shown a positive signal for both Λ and $\bar{\Lambda}$, and thus it is promising to eliminate the disturbing opposite polarization direction that occurred in previous experiments [1–6], and this confirms our predictions. Besides, the RHIC's Event Plane Detector (EPD), on upgrading for future BES II with higher EP resolution, will provide a better chance to determine the issue of centrality dependence of Λ polarization [34]. With experimental c.m. identification one could also verify the momentum dependence of the polarization as shown in Fig. 1.

The Λ polarization increases with its Feynman $x_F = p_L/\sqrt{s}$, as well as transverse momentum p_T, had been observed in experiments and can be partly attributed to the

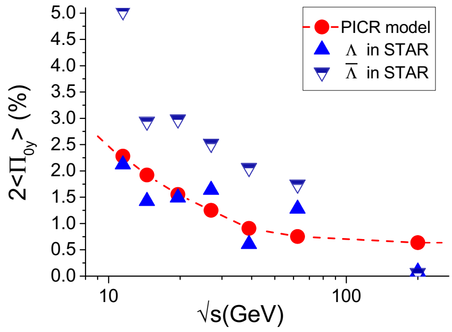

FIG. 3. The global polarization, $2\langle\Pi_{0y}\rangle_p$, in our PICR hydromodel (red circle) and STAR BES experiments (green triangle), at energies $\sqrt{s}$ of 11.5, 14.5, 19.6, 27.0, 39.0, 62.4, and 200 GeV. The experimental data were extracted from Ref. [24], with solid triangle for Λ and hollow triangle for $\bar{\Lambda}$, dropping the error bars.

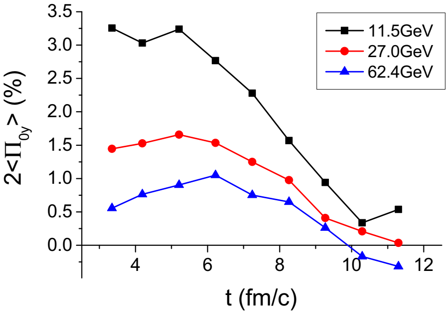

FIG. 4. The time evolution of global polarization, $2\langle\Pi_{0y}\rangle_p$, for energy $\sqrt{s}$ = 11.5, 27, and 62.4 GeV.

$s\bar{s}$ pair production mechanism. It was also predicated that the polarization should also depend on the collision energy $\sqrt{s}$, although early experiments did not find evident signals to confirm this [4,5,7]. Recently with an exploration to low energy domain between 7.7 and 27.0 GeV, the RHIC BES I program had successfully observed the energy dependence of Λ polarization with a higher EP resolution and better background extraction.

Using the PICR hydrodynamical model, we calculated the global Λ polarization at the following energies: 11.5, 14.5, 19.6, 27, 39, 62.4, and 200 GeV, and plotted them with red round symbols in Fig. 3. The impact parameter is $b_0 = 0.7$, i.e., the centrality is $c = 49\%$. For comparison the data of Λ and $\bar{\Lambda}$ polarization from STAR (RHIC) were inserted into Fig. 3 with blue triangle symbols. One could see that our model fits fairly well the experimental data. Although the experimental $\bar{\Lambda}$ polarization is larger than the Λ polarization, it will not change the averaged polarization very much, because the production ratio of $\bar{\Lambda}$ to Λ is very small in high energy collisions [35].

Figure 3 clearly shows that Λ polarization is dependent on collision energy; it drops very quickly with increasing energy from 11.4 to 62.4 GeV and tends to saturate after 62.4 GeV. From a thermodynamical perspective, the polarization decreases with energy, and this can be attributed to the higher temperature in higher energy collisions. The drastic thermal motion of particles will decrease the quark polarization rate, which according to Ref. [11] is inversely proportional to the collision energy. On the other hand, simulating results by a multi-phase transport (AMPT) model has shown that the averaged classical vorticity decreases with the collision energy [36,37], which, of course, leads to the decline of global Λ polarization.

It is also interesting to take a glance on the time evolution of Λ polarization, shown in Fig. 4. In this figure, the Λ polarization increases slowly at an early stage and then falls down very quickly. The negative polarization values that occur at 62.4 GeV after 10 fm/c demonstrate the loss of validity of the hydrodynamical model at late stages of system expansion, due to the large surface to volume ratio. Besides, at early stages, no Λs are produced, so the climbing segment of the curves before 4 fm/c is not observable.

Summary and conclusions. With a Yang-Mills field initial state and a high resolution (3+1)D Particle-in-Cell Relativistic (PICR) hydrodynamics simulation, we calculate the Λ polarization for different low energies and different impact parameters. The polarization in high energy collisions originates from initial angular momentum or the inequality of local density between projectile and target, and both of them are sensitive to the impact parameter. Thus, we plotted the global polarization as a function of impact parameter b and a linear dependence on b was observed. We hope that after upgrading the Event Plane Detector, the STAR will provide higher resolution EP determination and centrality, to determine precisely the centrality dependence of global Λ polarization.

Furthermore, the global Λ polarization in our model decreases very quickly in the low energy domain, and the decline curve fits very well with the recent results of Beam Energy Scan (BES) program launched by STAR (RHIC). This is a very exciting new result, which indicates the significance of thermal vorticity and system expansion.

Finally, the time evolution of Λ polarization shows the limitation of hydrodynamical model at later stage of system expansion.

Acknowledgments. Enlightening discussions with Mike Lisa and Francesco Becattini are gratefully acknowledged. One of the authors, Y. L. Xie, is supported by the China Scholarship Council (China).

---

[1] G. Bunce, R. Handler, R. March, P. Martin, L. Pondrom, and M. Sheaff, Phys. Rev. Lett. **36**, 1113 (1976).
[2] A. Lesnik, D. M. Schwartzf, I. Ambats, E. Hayes, W. T. Meyer, C. E. W. Ward, T. M. Knasel, E. G. Swallow, R. Winston, II, and T. A. Romanowski, Phys. Rev. Lett. **35**, 770 (1975).
[3] M. Anikina *et al.*, Z. Phys. C **25**, 1 (1984).
[4] A. M. Smith *et al.* (R608 Collaboration), Phys. Lett. B **185**, 209 (1987).
[5] E. J. Ramberg *et al.*, Phys. Lett. B **338**, 403 (1994).
[6] A. Morelos *et al.* (E761 Collaboration), Phys. Rev. Lett. **71**, 2172 (1993).
[7] I. Abt *et al.* (HERA-B Collaboration), Phys. Lett. B **638**, 415 (2006).
[8] I. Selyuzhenkov *et al.* (STAR Collaboration), J. Phys. G: Nucl. Part. Phys. **32**, S557 (2006).
[9] B. I. Abelev *et al.*, Phys. Rev. C **76**, 024915 (2007).
[10] Z.-T. Liang and X.-N. Wang, Phys. Rev. Lett. **94**, 102301 (2005).
[11] X.-G. Huang, P. Huovinen, and X.-N. Wang, Phys. Rev. C **84**, 054910 (2011).
[12] B. Betz, M. Gyulassy, and G. Torrieri, Phys. Rev. C **76**, 044901 (2007).
[13] F. Becattini, G. Inghirami, V. Rolando, A. Beraudo, L. D. Zanna, A. De Pace, M. Nardi, G. Pagliara, and V. Chandra, Eur. Phys. J. C **75**, 406 (2015).
[14] A. D. Panagiotou, Phys. Rev. C **33**, 1999 (1986).
[15] F. Becattini, V. Chandra, L. Del Zanna, and E. Grossi, Ann. Phys. **338**, 32 (2013).

[16] C. C. Barros and Y. Hama, Int. J. Mod. Phys. E **17**, 371 (2008).
[17] F. Becattini, L. P. Csernai, and D. J. Wang, Phys. Rev. C **88**, 034905 (2013).
[18] Y.-L. Xie, R. C. Glastad, and L. P. Csernai, Phys. Rev. C **92**, 064901 (2015).
[19] Y. L. Xie, M. Bleicher, H. Stöcker, D. J. Wang, and L. P. Csernai, Phys. Rev. C **94**, 054907 (2016).
[20] L. P. Csernai, G. Eyyubova, and V. K. Magas, Phys. Rev. C **86**, 024912 (2012).
[21] F. Becattini, F. Piccinini, and J. Rizzo, Phys. Rev. C **77**, 024906 (2008).
[22] J.-H. Gao, S.-W. Chen, W.-T. Deng, Z.-T. Liang, Q. Wang, and X.-N. Wang, Phys. Rev. C **77**, 044902 (2008).
[23] I. Karpenko and F. Becattini, arXiv:1610.04717.
[24] M. A. Lisa *et al.* (STAR Collaboration), QCD Chirality Workshop 2016, Feb. 23–26, 2016, Los Angeles, USA (unpublished).
[25] T. A. DeGrand and H. I. Miettinen, Phys. Rev. D **24**, 2419 (1981).
[26] L. P. Csernai, D. D. Strottman, and Cs. Anderlik, Phys. Rev. C **85**, 054901 (2012).
[27] D. Montenegro, L. Tinti, and G. Torrieri, arXiv:1701.08263 (unpublished).
[28] L. P. Csernai, D. J. Wang, and T. Csorgo, Phys. Rev. C **90**, 024901 (2014).
[29] V. K. Magas, L. P. Csernai, and D. D. Strottman, Phys. Rev. C **64**, 014901 (2001).
[30] V. K. Magas, L. P. Csernai, and D. D. Strottman, Nucl. Phys. A **712**, 167 (2002).
[31] L. P. Csernai, *Introduction to Relativistic Heavy Ion Collisions* (Jonh Wiley & Sons Ltd., Chichester, UK, 1994).
[32] Y. Cheng, L. P. Csernai, V. K. Magas, B. R. Schlei, and D. D. Strottman, Phys. Rev. C **81**, 064910 (2010).
[33] R.-H. Fang, L.-G. Pang, Q. Wang, and X.-N. Wang, Phys. Rev. C **94**, 024904 (2016).
[34] J.-L. Zhang *et al.* (STAR Collaboration), Strangeness in Quark Matter 2016, June 27–July 1, 2016, Berkeley, USA (unpublished).
[35] T. Anticic *et al.* (NA49 Collaboration), Phys. Lett. B **93**, 022302-1 (2004).
[36] Y. Jiang, Z.-W. Lin, and J.-F. Liao, Phys. Rev. C **94**, 044910 (2016).
[37] W.-T. Deng and X.-G. Huang, Phys. Rev. C **93**, 064907 (2016).

Paper 5

PHYSICAL BASIS OF SUSTAINABLE DEVELOPMENT

Paper 6

Λ polarization in an exact rotating and expanding fluid dynamical model for peripheral heavy ion reactions

EPJ Web of Conferences **117**, 03016 (2016) DOI: 10.1051/epjconf/201611703016
NN2015

Λ polarization in an exact fluid dynamical model for heavy-ion collisions

Yilong Xie*

Department of Physics and Technology,
University of Bergen, Allegaten 55, 5007 Bergen, Norway

Abstract

Λ polarization is calculated in an exact analytical, rotating model based on parameters from a high resolution (3+1)D Particle-in-Cell Relativistic hydrodynamics calculation. The polarization is attributed to effects from thermal vorticity and for the first time the effects of the radial and axial acceleration are also studied separately.

At finite impact parameters, the initial state (IS) has non-vanishing angular momentum. Early studies neglected effects arising from the non-vanishing angular momentum, but interest increased recently. With the development of hydrodynamic modeling, rotation and its consequences were studied as well.

Thermal vorticity arises from the inverse temperature field in heavy ion collisions, and due to the non-vanishing angular momentum and shear in the initial stages. We look at polarization in effects arising from thermal vorticity in an exact rotating model [1], corresponding to an appropriate time-period of the collision based on a (3+1)D fluid dynamical model

Conventionally, $[x, z]$-plane is the reaction plane, with y being the axis of rotation. Then the initial angular momentum points into the negative y-direction, with an absolute value of approximately $1.45 \cdot 10^4\hbar$.

---

*Email: yilong.xie@uib.no

Following [2], the polarization arises from the thermal velocity field, $\beta^\mu(x) = u^\mu(x)/T(x)$, due to equipartition between vorticity and spin as

$$\Pi_\mu(p) = \hbar\epsilon_{\mu\sigma\rho\tau}\frac{p^\tau}{8m}\frac{\int d\Sigma_\lambda p^\lambda n_F(x,p)(1-n_F(x,p))\partial^\rho\beta^\sigma}{\int d\Sigma_\lambda p^\lambda n_F(x,p)} \ . \tag{1}$$

where $\epsilon_{\mu\rho\sigma\tau}$ is the completely antisymmetric Levi-Civita symbol, n_F the Fermi-Jüttner distribution for spin-1/2 particles, $(1-n_F)$ is the Pauli blocking factor and p is the four-momentum of the Λ.

The Λ polarization is determined by measuring the angular distribution of the decay protons in the Λ's rest frame. By Lorentz boosting the polarization vector, $\boldsymbol{\Pi}(\boldsymbol{p})$, in the participant frame, one can obtain the polarization vector $\boldsymbol{\Pi}_0(\boldsymbol{p})$ in Λ's rest frame:

$$\boldsymbol{\Pi}_0(\boldsymbol{p}) = \boldsymbol{\Pi}(p) - \frac{\boldsymbol{p}}{p^0(p^0+m)}\boldsymbol{\Pi}(p)\cdot\boldsymbol{p} \ , \tag{2}$$

where $(p^0, \boldsymbol{p})$ is the Λ four-momentum and m its mass.

As the Λ is transversely polarized, $\Pi^\mu p_\mu = 0$, one can confine himself to the spatial part of Π^μ. The simplified spatial part of polarization vector is:

$$\begin{aligned}\boldsymbol{\Pi}(p) &= \boldsymbol{\Pi_1}(p) + \boldsymbol{\Pi_2}(p) \\ &= \frac{\hbar\epsilon}{8m}\frac{\int dV n_F(x,p)\,(\nabla\times\boldsymbol{\beta})}{\int dV n_F(x,p)} \\ &\quad + \frac{\hbar\boldsymbol{p}}{8m}\times\frac{\int dV n_F(x,p)\,(\partial_t\boldsymbol{\beta}+\nabla\beta^0)}{\int dV n_F(x,p)} \ . \end{aligned} \tag{3}$$

Using the vorticity evaluated in [3], for the non-relativistic Exact model, we deduced the analytical solution for the Λ polarization:

$$\begin{aligned}\boldsymbol{\Pi}(p) = \frac{\hbar}{8mT}\Bigg[\frac{p_y c_9}{c_3\sqrt{c_4}}\frac{M_{-1,\frac{1}{2}}}{M_{-\frac{1}{2},0}}\boldsymbol{e}_x &+ \left(2\epsilon\omega - \frac{|p_x|c_9}{c_3\sqrt{c_4}}\times\frac{M_{-1,\frac{1}{2}}}{M_{-\frac{1}{2},0}}\right)\boldsymbol{e}_y \\ &+ \left(\frac{|p_x|c_7c_1}{2c_2} - \frac{p_y c_8}{c_3\sqrt{c_4}}\frac{M_{-1,\frac{1}{2}}}{M_{-\frac{1}{2},0}}\right)\boldsymbol{e}_z\Bigg] \ , \end{aligned} \tag{4}$$

where c_i $(i = 1-9)$ are parameters in terms of scaling variables and $M_{\mu,\nu}(z)$, is the Whittaker function, the confluent hypergeometric function [1].

As seen in eq. (4), the polarization consists of two terms, $\boldsymbol{\Pi_1}(p)$ and $\boldsymbol{\Pi_2}(p)$, which arise from local vorticity $(\nabla\times\boldsymbol{\beta})$ and expansion $(\partial_t\boldsymbol{\beta})$. One can see from Fig. 1, that the second term in the polarization is of comparable

EPJ Web of Conferences **117**, 03016 (2016) DOI: 10.1051/epjconf/201611703016
NN2015

magnitude to the term arising from local vorticity. In a previous calculation [4], the p dependence of n_F, was considered negligible in the integral, and the time derivative and gradient terms were also assumed to be smaller. The present calculation shows that in general these terms are not negligible.

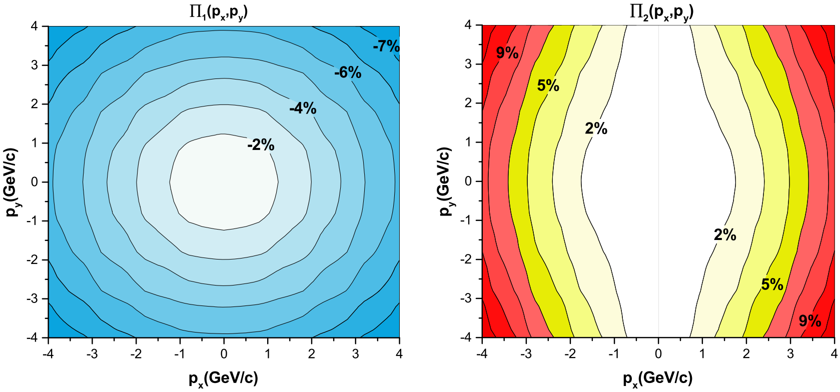

Figure 1: (color online) The two terms of Λ polarization $\boldsymbol{\Pi}_1(\boldsymbol{p})$ (left panel), $\boldsymbol{\Pi}_2(\boldsymbol{p})$ (right panel) in the participant frame at time $t = 0.5$ fm/c after the equilibration of the rotation, in the Exact model. Based on Ref. [1].

The Λ polarization is measured via the angular distribution of the decay protons in the Λ's rest frame, as shown in Eq. (2). The resulting distribution is shown in Fig. 2. The structure of $\Pi_{0y}(\boldsymbol{p})$ is similar to the one obtained in [4], but it reaches 12% at high p_x values, greater than 9% in Ref. [4], due to the contribution of the "second", $\partial_t \boldsymbol{\beta}$ term. These new studies indicate that the dynamics of the expansion may also lead to non-negligible contribution to the observable polarization.

Recently the vorticity and polarization were also studied in another fluid dynamical model [5], where the initial shear flow is neglected. This results in negligible thermal vorticity (Figs. 3 and 13 of Ref. [5]), and consequently a negligible polarization from the vorticity, i.e. from the "first term" discussed here. On the other hand, there is qualitative agreement between Fig. 12 of Ref. [5] and this work in the sense that only the y-directed (i.e. $[x, z]$ or $[x, \eta]$) component of the vorticity leads to an overall average net polarization. This arises in both models from the initial angular momentum and points into the $-y$-direction. In Ref. [5] this arises as a consequence of viscous evolution of the initial, vorticity-less flow, while in our Exact model it is present in the initial state.

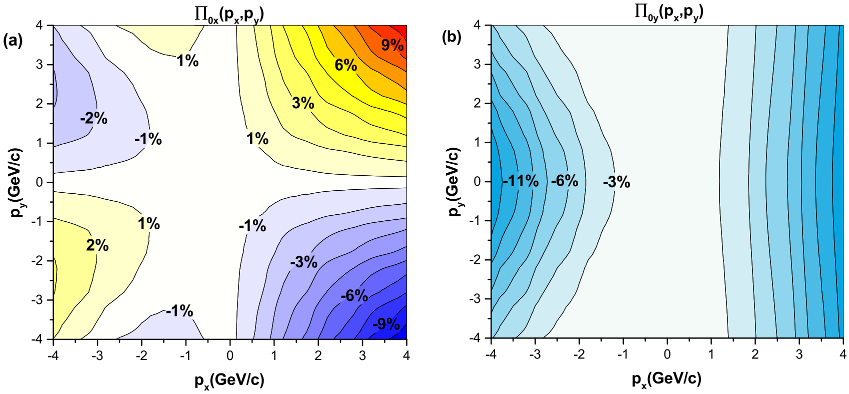

Figure 2: (color online) The radial, x, and axial, y, components of Λ-polarization, $\boldsymbol{\Pi}_0(\boldsymbol{p})$, in the Λ's rest frame. Both plots are asymmetric due to the Lorentz boost to the Λ rest frame. From [1].

In this work we analyzed and compared the two terms, and the Exact model. Including both rotation, expansion, and vorticity arising from both effects. This study indicates that the assumptions regarding the initial state are influencing the predictions on the observed vorticity.

Acknowledgements

Enlightening discussions with Francesco Becattini are gratefully acknowledged. This author is supported by the China Scholarship Council.

References

[1] Yilong Xie, Robert C. Glastad, Laszlo P. Csernai, arXiv: 1505.07221v2.

[2] F. Becattini, V. Chandra, L. Del Zanna, E. Grossi, Annals of Physics **338**, 32 (2013).

[3] L.P. Csernai, J.H. Inderhaug, Int. J. Mod. Phys. E **24**, 1550013 (2015).

[4] F. Becattini, L.P. Csernai, and D.J. Wang, Phys. Rev. C **88**, 034905 (2013).

[5] F. Becattini, G. Inghirami, V. Rolando, A. Beraudo, L. Del Zanna, A. De Pace, M. Nardi, G. Pagliara, and V. Chandra, arXiv: 1501.04468v2.